Master's thesis

NTNU
Norwegian University of Science and Technology
Faculty of Natural Sciences
Department of Materials Science and Engineering

Ulrik Aalborg Eriksen

Sintering and transport properties of Al-LLZO ceramic electrolytes for use in solid-state Li-ion batteries

Master's thesis in Materials Science and Engineering
Supervisor: Kjell Wiik
Co-supervisor: Mari-Ann Einarsrud, Evgeniya Khomyakova and Leif Olav Jøsang

June 2021

NTNU
Norwegian University of Science and Technology

Ulrik Aalborg Eriksen

Sintering and transport properties of Al-LLZO ceramic electrolytes for use in solid-state Li-ion batteries

Master's thesis in Materials Science and Engineering
Supervisor: Kjell Wiik
Co-supervisor: Mari-Ann Einarsrud, Evgeniya Khomyakova and Leif Olav Jøsang
June 2021

Norwegian University of Science and Technology
Faculty of Natural Sciences
Department of Materials Science and Engineering

NTNU
Norwegian University of Science and Technology

Preface

This master's thesis was written as part of the TMT4905 course at the Department of Materials Science and Engineering at the Norwegian University of Science and Technology.

First and foremost, I would like to thank my main supervisor Kjell Wiik for excellent guidance and support throughout the work on this thesis. I also want to thank my co-supervisors at Cerpotech and NTNU for for both practical assistance and useful input. Thank you to all the people in the FACET battery group for sharing their knowledge, and the laboratory engineers at IMA for always lending a helping hand.

Lastly, I want to thank my fellow materials science students for 5 amazing years in Trondheim. Thanks for making every day enjoyable, and I will never forget the times we shared at 113 and elsewhere.

- Ulrik Aalborg Eriksen

> I've been waiting for you,
> Obi-Wan. We meet again, at last.
> The circle is now complete. When I
> left you, I was but the learner; now
> I am the *master*.
>
> A New Hope

Abstract

Solid-state electrolytes are investigated as a potential substitute to the common liquid organic electrolytes employed in current Li-ion battery technology. The implementation of solid-state electrolytes will improve battery safety and enable the use of high capacity Li metal anodes. $Li_7La_3Zr_2O_{12}$ (LLZO) is a promising material which exhibits high ionic conductivity upon doping and is stable in contact with Li metal.

This work focused on LLZO doped with aluminium $Li_{6.25}Al_{0.25}La_3Zr_2O_{12}$ (Al-LLZO), produced by spray pyrolysis at Cerpotech. Three different stoichiometry powders were sprayed, with 8, 24, and 30 mol% Li excess added to make up for Li-loss during synthesis. Sintering experiments were conducted in ambient air at 1000 °C and 1150 °C, and sintered samples were evaluated based on their phase composition, density, microstructure, and ionic conductivity. The most successful sintering program heated the pellets to 1150 °C for 2h and resulted in pure cubic LLZO phase and above 90% relative density. However, sintering at 1150 °C also caused abnormal grain growth, which reduces the mechanical strength of the solid electrolyte. The ionic conductivity of Al-LLZO with 24 mol% Li excess was generally superior, and with the optimal sintering program a high ionic conductivity of $\sim 3.0 \cdot 10^{-4}\ Scm^{-1}$ was achieved.

Sammendrag

Faststoffelektrolytter blir forsket på som en mulig substitutt til de flytende organiske elektrolyttene som brukes i dagens Li-ion batterier. Bruk av faststoffelektrolytter vil øke batterisikkerheten, og muliggjøre bruk av Li-metall anoder med høy kapasitet. $Li_7La_3Zr_2O_{12}$ (LLZO) er et lovende materiale, som kan dopes for å oppnå høy ionisk ledningsevne, og som ikke reagerer med Li-metall.

Dette arbeidet fokuserte på LLZO dopet med aluminium, $Li_{6.25}Al_{0.25}La_3Zr_2O_{12}$ (Al-LLZO), produsert med spraypyrolyse på Cerpotech. Tre pulver med forskjellig støkiometri ble sprayet, der enten 8, 24 eller 30 mol% Li-overskudd ble benyttet for å gjøre opp for tap av Li i løpet av syntesen. Sintring ble gjennomført i åpen ovn på 1000 °C og 1150 °C. Etter sintring ble prøvene karakterisert og evaluert basert på fasesammensetning, tetthet, mikrostruktur og ionisk ledningsevne. Det sintringsprogrammet som gav best resultater holdt prøvene på sintringstemperatur 1150 °C i 2 timer, og resultatet var en ren kubisk LLZO fase med relativ tetthet over 90%. Sintring på 1150°C medførte også en enorm kornvekst, som går ut over de mekaniske egenskapene. Den ioniske ledningsevnen til Al-LLZO tilsatt 24 mol% Li-overskudd var generelt overlegen, og ved bruk av det best tilpassede sintringsprogrammet ble ionisk ledningsevne på $\sim 3.0 \cdot 10^{-4}\ Scm^{-1}$ oppnådd.

Table of Contents

List of Abbreviations

AGG	Abnormal grain growth
Al-LLZO	$Li_{6.25}Al_{0.25}La_3Zr_2O_{12}$
BP-ratio	Bed powder ratio
CIP	Cold isostatic pressing
EDS	Energy-dispersive X-ray spectroscopy
EIS	Electrochemical impedance spectroscopy
EPMA	Electron probe micro analyser
HT	High temperature
LIB	Lithium ion battery
LLZO	$Li_7La_3Zr_2O_{12}$
LT	Low temperature
RD	Relative density
RT	Room temperature
SEM	Scanning electron microscope
SP	Sintering program
SPS	Spark plasma sintering
VLC	Volatile lithium compound
WDS	Wavelength-dispersive X-ray spectroscopy
XRD	X-ray diffraction

List of Figures

List of Tables

1 Introduction

1.1 Background & motivation

Lithium ion batteries (LIBs) are essential in enabling a range of current technologies and will become increasingly important in the years to come. Battery technology will play a crucial part in the upcoming energy transition, and this has caused a huge interest in developing better LIBs. The popularity of the LIB technology can mostly be attributed to the high cell voltage and energy density provided by Li. Despite the many advantages of LIBs, current technology has shortcomings and limitations which could be overcome by switching to a solid electrolyte: namely battery safety and incompatibility with Li metal anodes.

Solid-state electrolytes functions much like the liquid organic electrolytes found in most current batteries; the solid-state electrolyte acts as both a separator for the electrodes and an ionic conductor, as sketched in Fig. 1.1. The solid-state electrolyte has a high mobility of Li ions, which allows for migration of Li ions during operation. The electronic conductivity on the other hand should be poor [1], to avoid short-circuiting of the cell and dendrite formation.

$Li_{6.25}Al_{0.25}La_3Zr_2O_{12}$ (Al-LLZO) is a promising solid-state electrolyte material. It is a ceramic material with a garnet-like crystal structure. It is a $Li_7La_3Zr_2O_{12}$ (LLZO) material doped with Al to stabilise the cubic polymorph and improve the ionic conductivity. The high Li conductivity, low reactivity with Li metal, and wide electrochemical stability window makes Al-LLZO a promising candidate for the solid-state batteries of the future [2].

Al-LLZO is an inorganic solid electrolyte, which could drastically improve battery safety by substituting the flammable organic electrolyte used in current LIBs. Organic electrolytes decompose exothermically if overheated, and if the temperature exceeds the critical temperature the cell will enter thermal runaway, meaning the reaction will become self-sustaining and unstoppable [3]. By instead employing thermally stable inorganic materials, there is no fuel to enable such a reaction, which increases the battery safety.

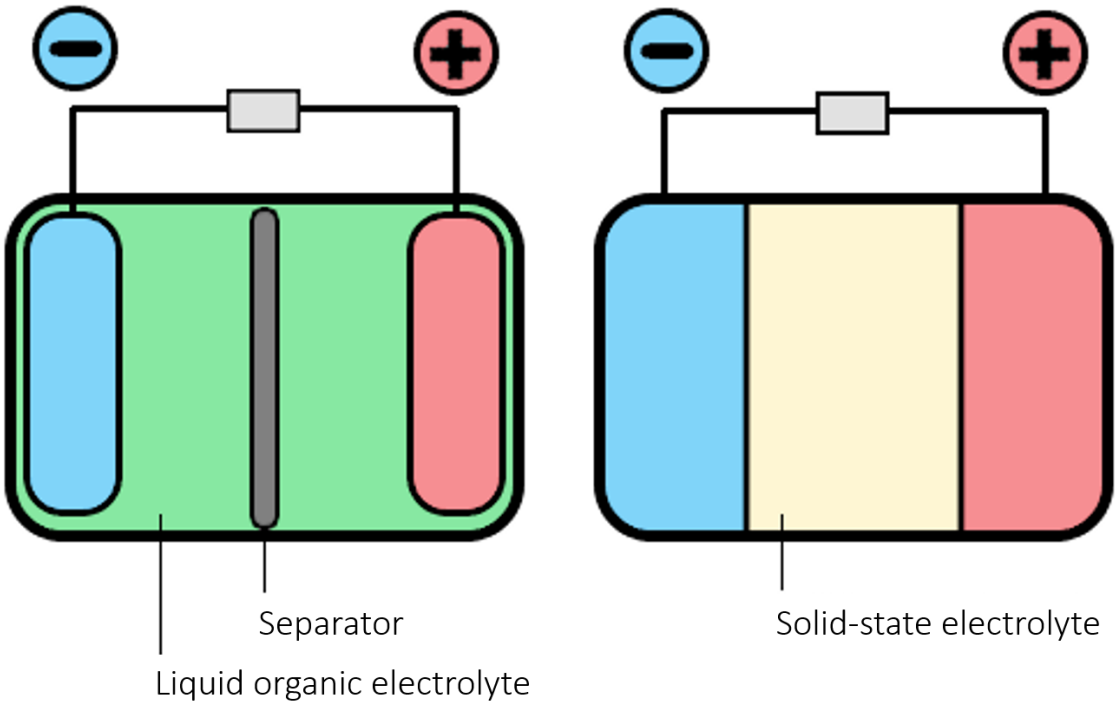

Figure 1.1. Schematic drawing of a liquid organic electrolyte Li-ion battery (left) and a solid-state Li-ion battery (right).

Al-LLZO has a high stability to Li metal, which allows Li metal to be used as anode material. Current LIBs use graphite anodes almost exclusively, and switching to Li metal anodes will increase the anode energy density [4]. Pure Li metal has the highest specific capacity of any anode, 10 times higher than the common graphite anodes [5]. Whereas Li metal anodes are difficult to combine with liquid organic electrolytes due to breakdown of the solid electrolyte interphase followed by dendrite growth, high mechanical strength is commonly reported to suppress dendrite growth in solid-state electrolytes [4, 6–8].

While Al-LLZO has desirable properties for solid-state electrolyte purposes, synthesising high quality material is challenging. Li in particular adds complexity to the LLZO system. High Li volatility at elevated temperatures makes controlling the stoichiometry complicated, and the Li content has a high influence on the phase composition and thereby the resulting ionic conductivity. Li is commonly add ed in excess during synthesis to combat the challenge of volatility. The system is also subject to abnormal grain growth (AGG) during sintering, which limits the use of high sintering temperatures to achieve densification.

Al-LLZO is usually synthesised by either a solid-state process or a co-precipitation technique. In this work, Al-LLZO is synthesised by spray pyrolysis, which is a affordable and continuous wet chemical synthesis [9]. A suitable process for Al-LLZO made by this spray pyrolysis technique must be established in order to produce high quality Al-LLZO.

1.2 Aim & scope

This work investigates the sintering behaviour and properties of Al-LLZO produced by spray pyrolysis. The effect of varying Li excess will be studied, with the goal of determining the appropriate amount. The aim is to produce a dense, single-phase cubic Al-LLZO material with good ionic conductivity, suitable for use as an electrolyte. Sintering experiments will be carried out in ambient atmosphere, and the sintering mechanism and resulting microstructure will be characterised by dilatometry and scanning electron microscopy (SEM). Quantitative element analysis will be performed by energy-dispersive spectroscopy (EDS) and wavelength-dispersive spectroscopy (WDS). The sintered pellet density will be measured using the Archimedes' principle, and the phase composition will be determined by X-ray diffraction (XRD). The resulting ionic conductivity will be measured by electrochemical impedance spectroscopy (EIS).

2 Literature Review

This section covers the necessary theory needed to interpret the results from this work. The content of this section is partly based on the theory section in the specialisation project by Eriksen [10]. In this section, the LLZO material is covered in detail: including its structure, the thermodynamics of the system, the Li^+ transport properties of the electrolyte, and the sintering behaviour.

2.1 LLZO

LLZO is a garnet-like structured oxide which have gained a lot of attention lately for its potential as electrolyte in solid-state batteries. Generally, garnet structures are on the from $A_3B_2C_3O_{12}$, where A are 8-coordinated, B are octahedral, and C are tetrahedral lattice sites. In the LLZO structure, the A, B, and C lattice sites are occupied by La^{3+}, Zr^{4+}, and Li^+ respectively. Compared to regular garnets, LLZO has 4 extra Li in the formula unit, these are placed at interstitial sites. Regular garnets usually crystallise in the cubic crystal system. However, LLZO also appears tetragonal due to the additional 4 Li^+ per formula unit which distort the LLZO lattice [11].

There are two possible crystal symmetries for the LLZO system: a cubic structure ($Ia\bar{3}d$, No. 230) and a tetragonal structure ($I4_1/acd$, No. 142). The cubic crystal structure has a disordered Li arrangement, with varying Li site occupancy less than unit. The tetragonal structure has accommodated for the interstitial Li^+ by distorting the lattice. This structure is highly ordered, with all sites having unit site occupancies [12]. The crystal structure has a huge impact on the transport properties of LLZO, causing the cubic crystal structure to exhibit ionic conductivity at least two orders of magnitude greater than the tetragonal structure [13]. Hence, controlling the symmetry of LLZO is crucial for producing a high quality electrolyte.

The Li sublattice of the cubic and tetragonal crystal structures are shown in Fig. 2.1. There are two different Li lattice sites in the cubic structure: Li(1) and Li(2) sites (Wyckoff positions 24d and 96h respectively). Both of these positions have

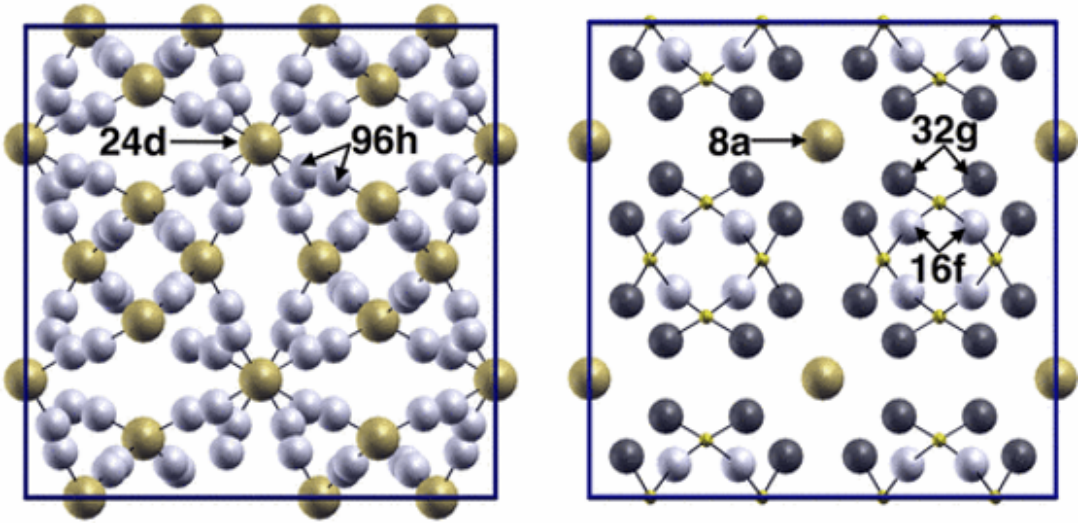

Figure 2.1. The Li sublattice in the cubic (left) and tetragonal (right) LLZO unit cell. All the lattice sites are included, but only a fraction of the cubic sites are actually occupied by Li^+ ions. Li(1) ions are gold, Li(2) ions are white and Li(3) ions are dark grey. Adopted from [13].

lower than unit occupancies [11]. In particular, the occupancy of cubic Li(2) sites is heavily restricted due to coulombic repulsive forces which prevent the occupation of both members of a 96h site pair (see figure). The tetragonal structure has Li(1), Li(2), and Li(3) sites (Wyckoff positions 8a, 16f and 32g respectively), and all these sites have unit occupancies [13]. The Li(1) positions are tetrahedrally coordinated, while both Li(2) and Li(3) are octahedrally coordinated to oxygen in the structure [14]. The complete crystal structure of LLZO is included in Appendix F, but because the unit cell is rather large and difficult to grasp, there are in many instances more practical to examine the Li sublattice. Also, one of the main differences between the two structures is the Li arrangement.

2.2 Thermodynamics of LLZO

LLZO appears in three different phases: one tetragonal and two cubic ones. The two cubic phases are usually denoted as high temperature (HT)-cubic and low temperature (LT)-cubic. Whereas the HT-cubic phase appears intrinsically in LLZO, the LT-cubic is only obtained through reactions with CO_2 or H_2O [12, 15–17]. Unless

explicitly stated otherwise, every instance of the cubic structure in this thesis refers to the HT-cubic phase.

Controlling the phase of the material is crucial, as the difference in ionic conductivity is huge. The HT-cubic phase has 2-3 orders of magnitude better ionic conductivity than the other two phases [18]. Typical literature values for HT-cubic LLZO are $> 10^{-4}\ Scm^{-1}$, while the other two phases only show ionic conductivity of about $10^{-6}\ Scm^{-1}$.

2.2.1 Undoped LLZO

Tetragonal LLZO is the most stable LLZO phase at ambient conditions, which is uncommon in garnets. One reason the system favours a tetragonal symmetry is due to the Li-Li electrostatic repulsion. In an effort to reduce this Coulomb repulsion, the Li sites are ordered. However, this ordering of Li^+ distorts the crystal structure unfavourably, which causes a tetragonal transformation in order to preserve optimal bond angles. The ordering of Li^+ and the cubic-tetragonal phase transition are inherently linked, neither process would be spontaneous without the other [13].

The tetragonal phase has low bulk ionic conductivity, hence several studies have investigated how to trigger the tetragonal-cubic phase transition. The phase stability is governed by the free energy of the system. In eq. 2.1, $\Delta G_{t\rightarrow c}$ is the free energy, $\Delta H_{t\rightarrow c}$ is the enthalpy, and $\Delta S_{t\rightarrow c}$ is the entropy of the tetragonal-cubic phase transition. T is the absolute temperature.

$$\Delta G_{t\rightarrow c} = \Delta H_{t\rightarrow c} - T\Delta S_{t\rightarrow c} \tag{2.1}$$

The transition will be spontaneous once the corresponding free energy is negative. The Li^+ configuration of cubic LLZO is highly disordered, which causes the cubic phase to have lower entropy than the tetragonal phase. Hence, the reaction entropy of the tetragonal-cubic transition is positive. Knowing this, it is evident that this phase transition must be spontaneous at *some* temperature, as the entropy term in eq. 2.1 becomes increasingly negative at higher temperatures [13]. The temperature

where the free energy of transition is 0 is known as the transition temperature or critical temperature (T_c) and is given by eq. 2.2.

$$T_c = \frac{\Delta H_{t\to c}}{\Delta S_{t\to c}} \tag{2.2}$$

Several studies have investigated the transition temperature of the tetragonal-cubic phase transition in undoped LLZO, a summary of their findings is provided in Table 2.1. The reported values for T_c are in the range $610 - 650$ °C. The transition is reversible and the reaction rate is high, as a consequence the cubic phase is *not* quenchable to room temperature (RT) [11, 12, 19]. Hence, undoped LLZO is not well suited as electrolyte material; only the tetragonal phase is stable at ambient conditions, and this phase has rather poor bulk ionic conductivity.

Table 2.1: Tetragonal-cubic transition temperature.

Transition temperature [°C]	Experiment	Ref
650	XRD	[12]
$610 - 630$	XRD	[15]
$\sim$630	Neutron diffraction	[19]

It is worth noting that there are some conflicting information and several reports of undoped LLZO exhibiting the cubic crystal symmetry in literature, including the initial discovery of the LLZO material by Murugan et al. [20]. This is probably a consequence of the high sensitivity of the LLZO system to contamination. In cases were samples have been exposed to the atmosphere, this might be due to formation of the LT-cubic phase. Another frequent issue is accidental Al contamination from alumina crucibles, which can stabilise the cubic phase [11, 15, 21–23]. Additionally, controlling the amount of Li is not simple, due to the high volatility of Li. High loss of Li might leave the LLZO Li-deficient, which can act to stabilise the cubic phase as shown by Paoella et al. [16]. Hence, the atmosphere and Li content must be carefully controlled, and inert crucibles must be employed in order to produce pure undoped LLZO.

2.2.2 Al-doped LLZO

Aluminium is one of the most studied doping elements in LLZO, which was early observed to stabilise cubic phase LLZO due to accidental contamination from alumina crucibles. In addition to stabilising the cubic LLZO phase through formation of Li vacancies, Al has other positive effects as it essentially works as a sintering aid. Formation of a Li-Al-O amorphous phase increase the rate of Li diffusion between the LLZO grains [24], and the sintering temperature is lowered by the presence of Al [25].

Doping of LLZO with supervalent cations have become the main approach to stabilise the cubic crystal structure at ambient conditions. In addition to Al, other cations like gallium, niobium, and tantalum are also frequently referenced in literature [26]. While the different doping elements have different preferred substitution sites in the LLZO lattice, they all serve the same basic purpose: to introduce Li vacancies into the LLZO structure.

The formation of Li vacancies stabilises the cubic crystal structure. This is because with less Li^+ in the crystal structure, the energy gained from ordering the Li^+ decreases [13]. The average Li-Li interatomic distance increases with the Li vacancy concentration, causing the repulsive forces to decrease. The system is therefore less incentivised to order the Li sites, and the tetragonal distortion does not occur. The aforementioned doping with supervalent cations is a convenient way of introducing these vacancies. Upon doping with a supervalent cation, the system must adapt in order to preserve electroneutrality [11, 27]. Al is trivalent, and prefers to substitute at Li sites. Hence, the addition of one Al atom must produce two Li vacancies in order to remain charge neutral, according to eq. 2.3 (Kröger-Vink notation).

$$[\mathrm{Al}_{\mathrm{Li}}^{\bullet\bullet}] = 2\,[\mathrm{v}'_{\mathrm{Li}}] \tag{2.3}$$

In agreement with the substitution reaction in eq. 2.3, Al-LLZO has nominal stoichiometry $Li_{7-3x}Al_xLa_3Zr_2O_{12}$. The phase diagram in Fig. 2.2 is provided by Matsuda et al. [18], and it shows the effect of Al content on the phase composition in the

LLZO system. From this, it is observed that the transition temperature decreases linearly with increasing Al content up to 0.2 Al per formula unit LLZO. At 0.25 Al per formula unit, the cubic phase is the thermodynamically stable polymorph at all temperatures, which corresponds to 0.5 Li vacancies per formula unit. Interestingly, as the transition temperature decreases with increasing Al content, so does the rate of the phase transition. Due to this slower transition rate, the cubic phase was experimentally proven to be quenchable from above the transition temperature to RT with an addition of 0.2 Al, or 0.4 Li vacancies, per formula unit LLZO [18]. Bernstein et al. [13] reported that the critical vacancy concentration necessary to stabilise the cubic phase is more than 0.4 Li vacancies per formula unit LLZO, which has proven to fit reasonably well for Al, as well as for other doping elements.

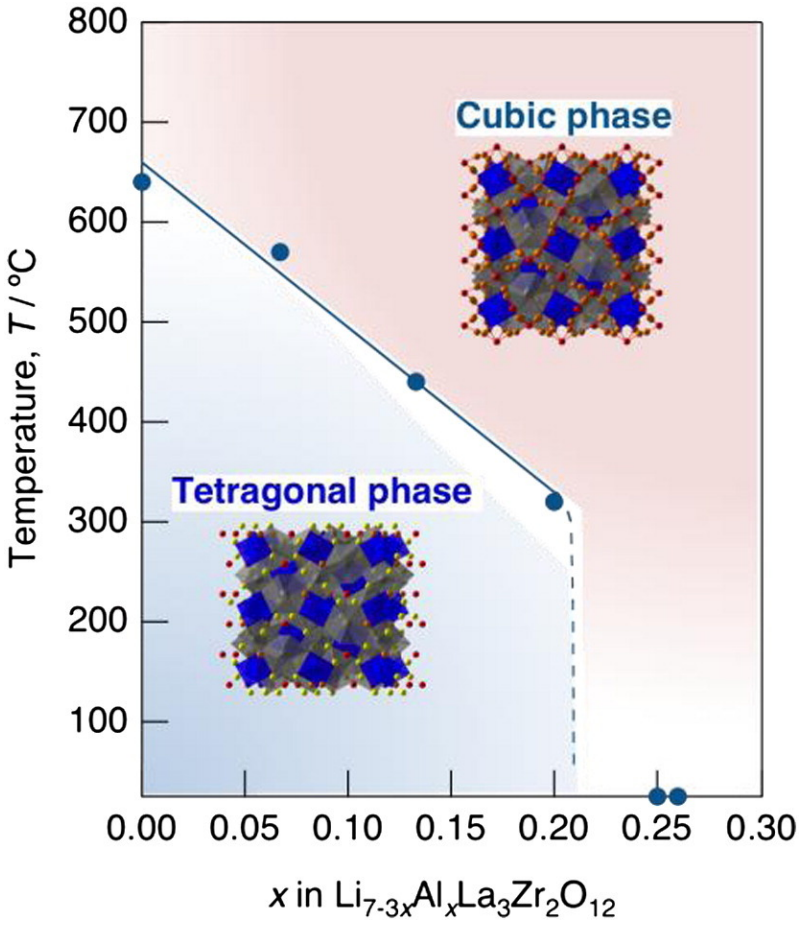

Figure 2.2. Phase diagram of Al-LLZO, by Matsuda et al. [18].

2.2.3 Impurity phases

There are some notable impurity phases which are frequently observed in the LLZO system. These phases have a negative effect on the ionic conductivity, and are therefore undesirable in the final product. However, knowledge about their formation is key in producing high quality single-phase cubic LLZO.

Tetragonal phase LLZO appears even in doped LLZO if the Li content is too high, which is common due to the addition of Li excess. In adequately doped LLZO, tetragonal phase LLZO will revert back to the cubic LLZO phase as the Li content decreases due to Li-loss at high temperatures [10]. Tetragonal LLZO can be distinguished from cubic LLZO by XRD; a family of planes in the isotropic cubic structure will only produce a single Bragg peak, while a family of planes in the tetragonal structure will produce two separate Bragg peaks [12].

LT-cubic LLZO is the low ionic conductivity cubic LLZO phase obtainable at low temperatures. This phase might form due to reactions with H_2O or CO_2 in the atmosphere. The LT- and HT-cubic phases are distinguishable by (i) the slightly larger lattice parameter of the LT-cubic phase [18], (ii) the reversion of the LT-cubic phase back to the tetragonal phase at temperatures above the decomposition temperature (H_2O is extracted at lower temperatures than CO_2) [12, 15], and (iii) the significantly lower bulk ionic conductivity of the LT-cubic phase.

Formation of LT-cubic phase is minimised by limiting the exposure of LLZO to the atmosphere, especially at elevated temperatures where the reaction rate is at its highest. The rate of incorporation of both H_2O and CO_2 into the LLZO structure is high at around $100 - 200\,^{\circ}C$ [12, 15]. At lower temperatures the reaction rate is lower, and at higher temperatures the equilibrium is shifted more towards desorption of H_2O and CO_2.

$La_2Zr_2O_7$ (pyrochlore) is commonly found in LLZO systems and is formed due to Li deficiency. Li is a volatile element, and Li-loss at high temperatures might leave LLZO samples with insufficient Li content after heat treatment; pyrochlore is then formed according to eq. 2.4.

$$2\,Li_7La_3Zr_2O_{12} \longrightarrow 2\,La_2Zr_2O_7 + 7\,Li_2O + La_2O_3 \tag{2.4}$$

Formation of pyrochlore can be avoided by either adding Li excess to the synthesis prior to sintering, or by reducing Li-loss during heat treatment.

Li_2ZrO_3 secondary phase can form if the Li content is too high. Li is commonly added in excess to avoid residual pyrochlore, Li_2ZrO_3 can therefore form in this Li-rich environment. If the Li excess is higher than the Li-loss, it can result in residual Li_2ZrO_3 after heat treatment [19].

There also exist other stable phases in the Li_2O-ZrO_2 system (namely $Li_6Zr_2O_7$ and Li_8ZrO_6), as shown in the phase diagram in Fig. 2.3. While there are few or no mentions of these other Li_2O-ZrO_2 phases in LLZO in the literature, they could potentially form in Li-rich environments.

Li_2CO_3 is commonly encountered during LLZO synthesis. In many syntheses Li_2CO_3 is added as the Li source, but it is a relatively stable phase which might form in the presence of carbon, even if other Li sources are utilised [10]. The high stability of Li_2CO_3 might make Li inaccessible and therefore impede the formation of LLZO if the temperature is too low. The decomposition rate of Li_2CO_3 is improved greatly by heating to temperatures above its melting point (723 °C) [19, 29]. Upon decomposition of Li_2CO_3, the Li will react with any residual pyrochlore to form LLZO according to eq. 2.5.

$$2\,La_2Zr_2O_7 + 7\,Li_2CO_3 + La_2O_3 \longrightarrow 2\,Li_7La_3Zr_2O_{12} + 7\,CO_2 \tag{2.5}$$

Li-Al-O phases are found in LLZO systems with Al as doping element. These are amorphous phases which increases the intergranular diffusion rate of Li, thereby promoting sintering [24]. The phase diagram of the lithia-alumina system is shown

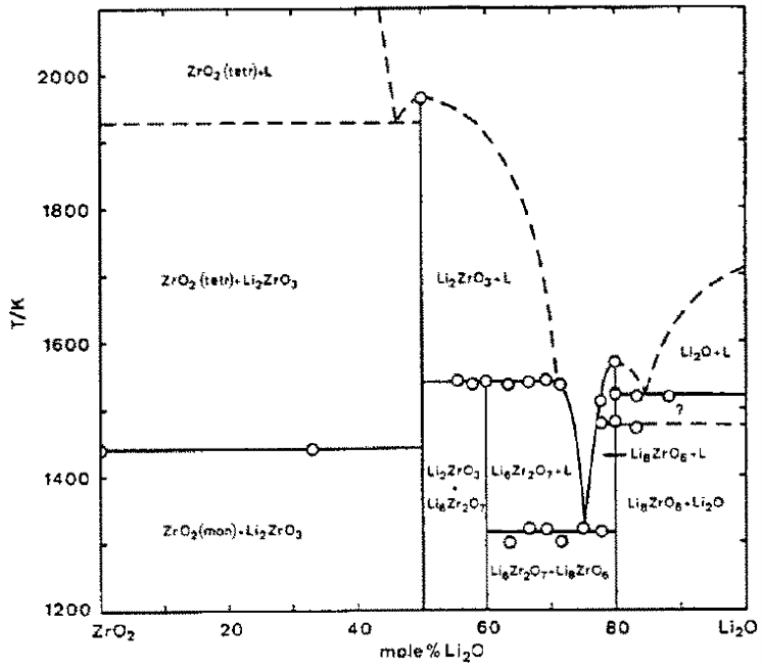

Figure 2.3. Phase diagram for the lithia-zirconia system, by Wyres and Cordfunke [28]. The eutectic phase consisting of $Li_6Zr_2O_7$ and Li_8ZrO_6 has a melting temperature of $1025 - 1049\,^{\circ}C$.

in Fig. 2.4, and the system has an eutectic phase with a melting point of 1064 °C. The melting point of this eutectic phase is lower than many common sintering temperatures for LLZO, and can therefore greatly increase sintering activity through the mechanism of viscous flow.

$LaAlO_3$ is another secondary phase which might form in Al-doped LLZO systems. It is formed if the addition of Al is higher than the solubility limit of Al in LLZO [18]. Lowering the Al content should reduce the amount of $LaAlO_3$ formed.

2.2.4 Volatile lithium compounds

Li-loss at high temperatures is evident from multiple experimental studies, however the mechanism of this loss is not well documented. Processes which might cause Li-loss in the garnet phase include (i) evaporation of volatile lithium compounds (VLCs), (ii) reactions with the crucible material, and (iii) loss of Li from the garnet phase to secondary phases [16, 31].

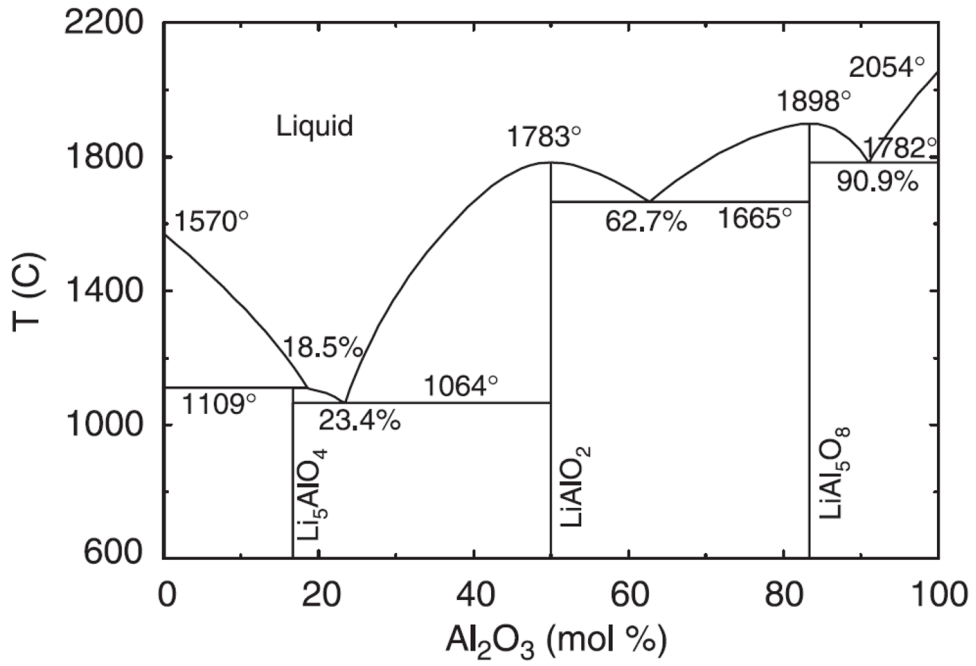

Figure 2.4. Phase diagram for the lithia-alumina system, by Kulkarni et al. [30]. The eutectic phase consisting of Li_5AlO_4 and $LiAlO_2$ has a melting temperature of 1064 °C.

VLCs in the LLZO system have been studied by Huang et al [31]. An alumina sheet was used to capture VLCs which originated from a LLZO specimen. The formation of both $LiAl_5O_8$ and $LiAlO_2$ on the alumina sheet proved the existence of VLCs. For sintering in air, the VLCs consist predominantly of $Li_2O_{(g)}$ [31].

Crucible material has a huge effect on the Li-loss. Materials like the common alumina crucibles are highly reactive with Li, and direct contact with alumina will cause huge Li-loss at high temperatures [32]. Bed powder is often used to avoid direct contact between LLZO pellets and alumina crucibles, and to assist in saturating the air with VLCs during sintering. Sintering can be performed without bed powder, but only in inert crucibles made from e.g. platinum or magnesia. Even with the use of bed powder, alumina crucibles can increase Li-loss compared to inert crucibles due to reactions between alumina and VLCs which reduce the VLC vapour pressure [33].

2.3 Li^+ transport

The high Li^+ conductivity is the primary advantage of the LLZO compared to other solid-state electrolytes. High Li^+ conductivity is a feature of garnet-like ceramic compounds with more than three Li atoms per formula unit. More than three Li atoms per formula unit forces some Li atoms into interstitial positions. This increases the lattice parameter and lowers the chemical interaction between Li^+ and other cations, which generally results in high Li^+ conductivity [11, 20].

Cubic phase LLZO exhibits orders of magnitude better Li^+ conductivity than the tetragonal phase. While descriptions of the cubic LLZO structure is somewhat incomplete due to varying site occupancies of Li and Al lattice sites, it is still possible to identify multiple causes for the better Li^+ conductivity of the cubic structure. Three properties of the cubic structure which benefit the Li^+ transport properties include (i) isotropic Li^+ migration pathways, (ii) lower migration barrier due to smaller distance between adjacent Li sites, and (iii) lower occupancy of Li sites [11].

The ionic conductivity of the cubic phase also depends on the dopant. To maximise the ionic conductivity of the cubic phase, Chen et al. [34] found that doping with small concentrations of high valence cations is the most effective. However, the doping level must be sufficient to not destabilise the cubic LLZO phase. In addition to the amount of vacancies, the distribution of vacancies in the crystal structure also determines the ionic conductivity. Li vacancies located close to the dopant element can essentially be deactivated if electrorepulsive forces make occupation of the sites unfavourable to Li^+ [34]. Deactivated vacancies will not contribute to Li^+ transport, and the conduction pathways must avoid these sites.

Usually, the term ionic conductivity refers to the total ionic conductivity (σ_{tot}) of the samples. This includes the contributions from the bulk and the grain boundaries (additive as resistivities $\rho_{total} = \rho_{bulk} + \rho_{gb}$) [35]. In addition to maximising the bulk ionic conductivity by stabilising the cubic LLZO phase, high relative density (RD) and tight grain boundaries are needed to maximise the grain boundary ionic conductivity [36, 37]. Porosity is negatively affecting the ionic conductivity. Li^+ ions are transported through the crystal structure, and pores act as physical barriers to

this transport.

It is worth noting that when the electrolyte is mounted in an electrochemical cell, interphase resistance between the electrolyte and electrodes plays a crucial role in determining the total internal resistance of the cell. However, the electrolyte-electrode interphase is a whole separate issue, which is beyond the scope of this thesis.

2.3.1 Li^+ conductivity in Al-LLZO

Al-doped LLZO exhibits increased ionic conductivity compared to undoped LLZO due to the stabilisation of the cubic phase. Still, other dopant strategies have proven just as, if not more, successful. An important feature of Al doping is the fact that Al substitutes at the tetrahedral Li(1) sites [38]. This has repercussions for the Li conduction pathways and activation energy, and the fact that Al has to block conduction pathways in order to produce vacancies in the structure is of importance [34]. Many studies have explored using other dopant elements like niobium and tantalum, which preferentially substitute outside the Li sublattice, at Zr sites. By doping outside the Li sublattice, faster Li^+ conduction pathways can be obtained [38], which is expected to enable even higher ionic conductivity.

Although higher ionic conductivity is always better, it is generally accepted that values of $10^{-4} \sim 10^{-3}\, S\, cm^{-1}$ at RT are good enough that bulk ionic conductivity is no longer the bottleneck in solid-state batteries [26]. Table 2.2 contains a summary of ionic conductivity values previously obtained in Al-LLZO. From this table it is obvious that Al-LLZO with ionic conductivity $> 10^{-4}\ S\ cm^{-1}$ is obtainable, even with ambient air sintering. However, in order to achieve high RD $\geq 98\%$, advanced sintering methods like hot-pressing and spark plasma sintering (SPS) should be applied.

Table 2.2: Ionic conductivity values measured in Al-LLZO and reported in literature. σ_{tot}=Total ionic conductivity, RD = Relative density.

Sintering conditions	RD	σ_{tot} ($\times 10^{-4}\, S\, cm^{-1}$)	Ref.
Ambient air sintering, 1200 °C @ 12h	79%	1.1 (33 °C)	[35]
Ambient air sintering, 1230 °C @ 6h	89.8%	1.8 (RT)	[39]
Ambient air sintering, 1200 °C @ 6h	86%	2.0 (RT)	[40]
Ambient air sintering, 900 °C @ 12h	N/A	2.1 (25 °C)	[41]
Ambient air sintering, 1300 °C @ 1h	N/A	2.1 (25 °C)	[18]
Ambient air sintering, 1100 °C @ 15h	92.5%	3.08 (20 °C)	[42]
Hot pressing, 62 MPa, 1050 °C @ 4h	98%	3.4 (20 °C)	[43]
Hot pressing, 40 MPa, 1000 °C @ 1h	98%	4.0 (RT)	[27]
Ambient air sintering, 1200 °C @ 24h[a]	96%	4.5 (25 °C)	[33]
SPS, 10 MPa, 1150 °C @ 3 min	99.8%	5.7 (RT)	[44]

[a] Experienced abnormal grain growth

2.3.2 Electrochemical impedance spectroscopy

The ionic conductivity of ceramics are commonly determined by EIS. The principle of EIS is that by applying small sinusoidal AC voltage impulses with varying frequency on a system, there will be a phase-shifted current response. The amplitude and phase shift of this current response is determined by the sample impedance [45].

Impedance is defined as the ratio between the voltage input signal and current response signal, much like resistance. However, resistance is only useful for describing ideal resistors which (i) obey Ohm's law for all current and voltage values, (ii) have frequency-independent resistance, and (iii) produce a current response in phase with the applied voltage. While subjected to an AC voltage, the solid-state electrolyte does not behave like an ideal resistor. Therefore, the electrical properties must be described by the impedance.

The AC impedance, Z, is frequency-dependent and is represented as a complex number, according to eq. 2.6.

$$Z(\omega) = \frac{E}{I} = \frac{E_0 \exp(i\omega t)}{I_0 \exp[i(\omega t - \phi)]} = Z_0 \exp(i\phi) = Z_0[\cos(\phi) + i\sin(\phi)] \tag{2.6}$$

Where E is the voltage signal, I is the current response, E_0 is the voltage amplitude, I_0 is the current amplitude, ω is the radial frequency, t is the time, and ϕ is the phase shift. The real part of the impedance is the resistance, which represent the magnitude, and the imaginary part is the reactance, which represent the phase shift.

2.4 LLZO sintering

In general, the goal of LLZO sintering is to obtain a material which (i) consists purely of the high ionic conductivity cubic LLZO phase, (ii) has RD close to 100% to minimise the grain boundary resistance, and (iii) consists of small and tightly bound grains which yield good mechanical strength. Producing a material which simultaneously exhibits all these properties is challenging, in large part due to Li.

The volatility of Li is the primary obstacle to the formation of pure single-phase cubic LLZO. The amount of Li excess must be tailored to the synthesis in order to avoid formation of the impurity phases detailed in Section 2.2.3.

Obtaining high RD is important in order to reduce the grain boundary resistance and improve σ_{tot}. Another benefit of low porosity and pore connectivity is the improved resistance to dendrite growth, which is crucial for the cycling performance of batteries [46]. Much effort has been put into increasing the RD of LLZO. These strategies include: (i) improved microstructure control by employing sintering programs with multiple holding temperatures [37, 47], (ii) rapid sintering at high temperatures [36], (iii) freeze drying of nano-sized raw powder in order to avoid agglomeration and limit the powder size [48], (iv) varying the amount of bed powder to control the vapour pressure of VLCs and thereby the Li-loss [31], (v) addition of various sintering additives [49, 50], and (vi) using advanced sintering techniques like hot-pressing and SPS to limit the sintering temperature [27, 43, 44].

The ideal microstructure of LLZO is widely considered to consist of small grains which are tightly bound to each other. This structure provides both good ionic conductivity and mechanical strength. However, AGG is a rather common occurrence in LLZO. AGG is a phenomenon where some grains devour neighbouring grains in order to grow enormous. AGG can be avoided by lowering the sintering temperature and holding time, but this should not be done at the expense of densification. Most of the previously covered strategies to increase the RD simultaneously aim to limit the AGG. Ideally, the temperature should allow densification processes like grain boundary diffusion to occur, while suppressing grain boundary migration. This is the principle of two-step sintering methods which have been used successfully to combat AGG [47]; by quickly heating to an elevated temperature and thereafter lowering the holding temperature, higher densification is possible without enabling AGG. It has also been demonstrated that both higher VLC vapour pressure and higher Al doping content cause increased AGG in LLZO [31, 42]. Lastly, sintering inhibitors have been successfully employed in tantalum and niobium doped LLZO systems to reduce AGG [37, 49, 50], by limiting the migration of grain boundaries.

3 Experimental

3.1 Chemicals & apparatuses

A list of the chemicals utilised in this thesis is provided in Table 3.1; Table 3.2 contains the apparatuses applied in this thesis.

Table 3.1: Utilised chemicals.

Chemical	Formula	State	Manufacturer	Purity
Lithium nitrate	$LiNO_3$	s	RodaChem	99.0 %
Aluminium nitrate	$Al(NO_3)_3 \cdot 9\,H_2O$	s	VWR Chemicals	98.5 %
Lanthanum nitrate	$La(NO_3)_3 \cdot 6\,H_2O$	s	Auer-Remy	$\geq$ 99.9 %
Zirconyl nitrate	$ZrO(NO_3)_2$	aq	Lehmann&Voss	99.9 %
Ammonia solution	25 % NH_4OH	aq	VWR Chemicals	-
Ethanol	96 % C_2H_5OH	l	VWR Chemicals	$\geq$ 99.8 %
Isopropanol	$(CH_2)_2CHOH$	l	VWR Chemicals	$\geq$ 99.7 %
Synthetic air	80 %N_2, 20 %O_2	g	Linde Group	5.0

Table 3.2: Utilised apparatuses.

Apparatus	Manufacturer & model	Purpose
Furnace	Nabertherm P330	Calcination & sintering
Dilatometer	Netzsch DIL 402 C	Study sintering behaviour
Rotavapor	Buchi R-210	Solvent evaporation
CIP	Autoclave Engineers CIP	Increase green body density
Diffractometer	Bruker D8 A25 DaVinci	Phase identification (XRD)
SEM	Zeiss Supra 55VP / Ultra 55	Microstructure & element analysis (EDS)
EPMA	JEOL JXA-8500F	Element analysis (WDS)
Sputter Coater	Edwards S150B	Au electrode deposition
Potentiostat	Biologic VMP-300	Ionic conductivity (EIS)

3.2 Procedure

An overview of the complete experimental procedure is shown in Fig. 3.1.

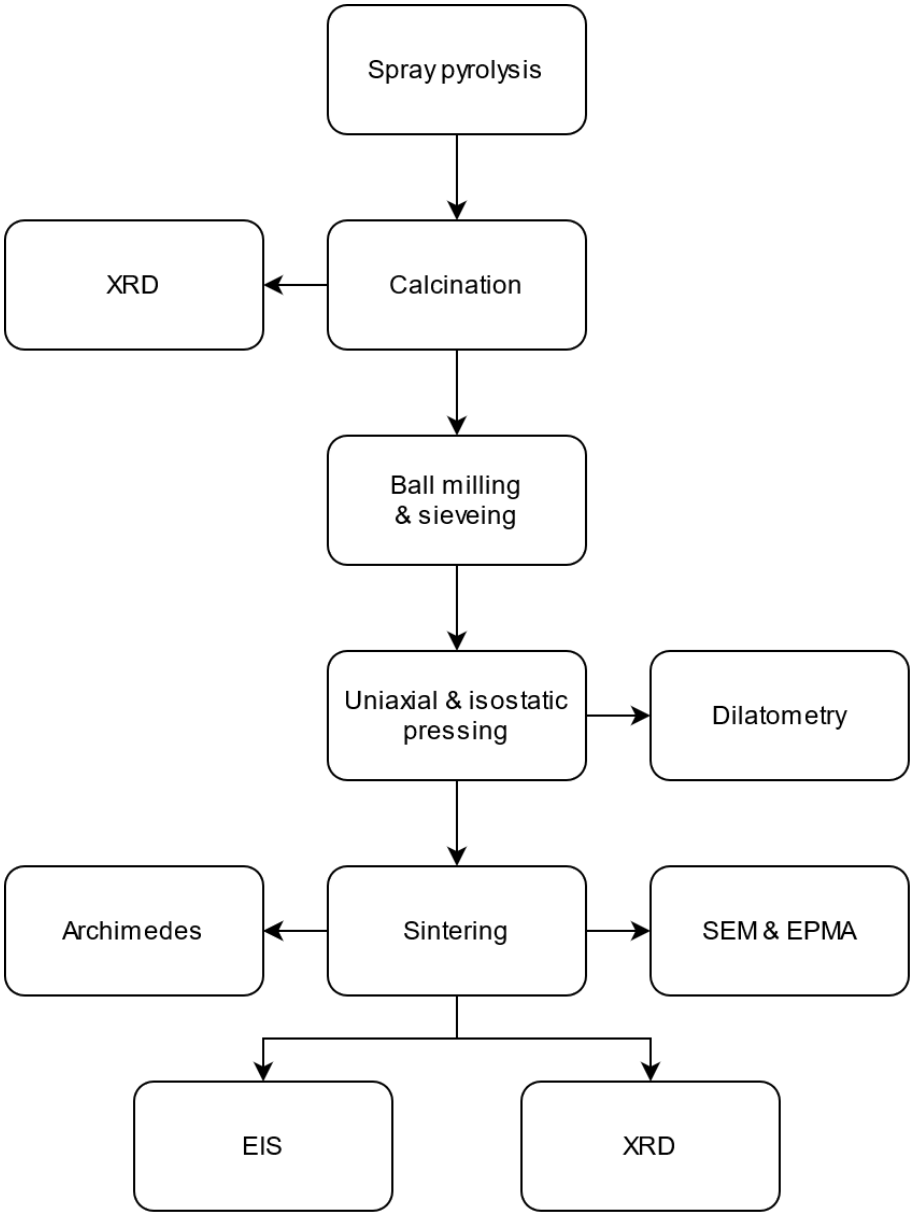

Figure 3.1. Flow chart of the experimental procedure.

3.2.1 Spray pyrolysis

Powder precursors were synthesised at Cerpotech AS, Trondheim. Solutions were prepared with nitrate-based precursors in molar ratios according to the target compositions summarised in Table 3.3. Powders of different Li excess will henceforth

be referred to by the nomenclature introduced in this table. Solutions containing zirconium and lathanum cations were prepared separately with deionised water as solute. Organic complexing agents were added, and ammonia was used for pH adjustments. The lanthanum and zirconium precursors were mixed vigorously, until the solutions were stabilised and turned transparent. The aluminium and lithium solution were added, and spray pyrolysis was conducted at 900 $°C$. A schematic of the spray pyrolysis technique is included in Fig. 3.2. The as-sprayed product of the spray pyrolysis process will be referred to as the powder precursor.

Table 3.3: Target stoichiometries of powders synthesised in this work.

Nomenclature	Li excess $[mol\%]$	Target stoichiometry
8-LLZO	8.0	$Li_{6.75}Al_{0.25}La_3Zr_2O_{12}$
24-LLZO	24.2	$Li_{7.7625}Al_{0.25}La_3Zr_2O_{12}$
30-LLZO	29.6	$Li_{8.1}Al_{0.25}La_3Zr_2O_{12}$

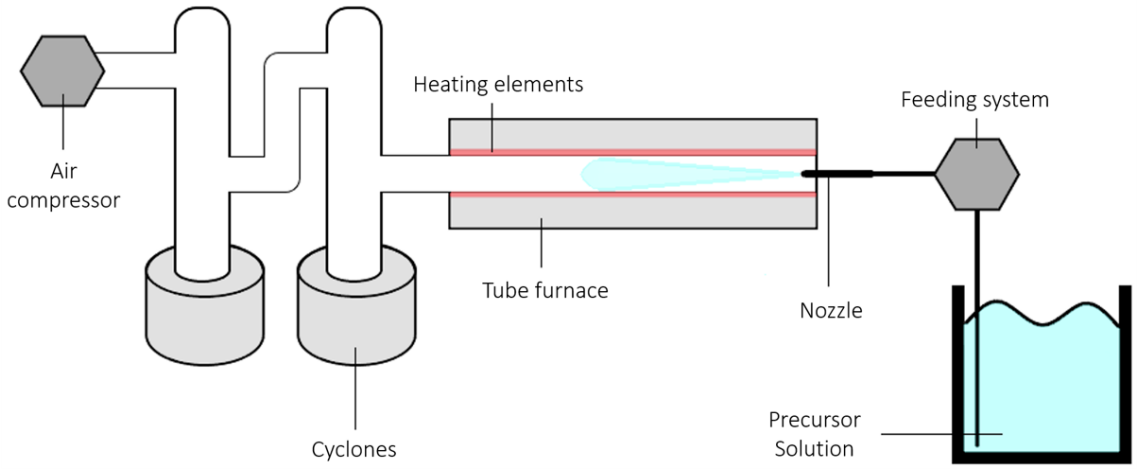

Figure 3.2. Schematic showing the spray pyrolysis setup.

3.2.2 Calcination

The powder precursor was calcined to remove organic residue from the spray pyrolysis process. Alumina crucibles were filled with powder precursor and were calcined

at 750 °C for 6h. Lids were placed on the crucibles to avoid refractory contamination, but there was a small gap to let out the gas formed due to decomposition reactions during calcination. The calcination was performed in ambient air. The heating and cooling rates were both set to $200\,°C\,h^{-1}$. The actual cooling rate varied with furnace temperature due to the lack of active cooling. The furnace was opened at $T \in [100\,°C,\ 200\,°C]$ to reach RT faster. The powder mass was measured before and after calcination.

The calcined powders were ball milled to break up agglomerates and to reduce the particle size. Varying amounts of calcined powder were mixed with 200 mL yttria-stabilised zirconia balls (with $d = 5\,mm$) and 100 mL isopropanol solvent in 500 mL flasks with a diameter of 7 cm. The rotation speed was approximately 120 rpm (measured by stopwatch), which equates to 75 % of the critical milling speed. After 24h of milling, the isopropanol was evaporated using a rotavapor. The soft agglomerates formed during drying were ground with a pestle in an agate mortar, and they were sieved through a 50 μm sieve to obtain a fine powder with a narrow particle size distribution.

3.2.3 Dilatometry

Calcined powder was pressed by double-action uniaxial pressing to produce pellet green bodies. The pressing tools were lubricated by a solution of stearic acid in ethanol, to make sure the pellet is easily removable after pressing. The pellet mass was approximately 250 mg and the diameter was 5 mm after uniaxial pressing. The powder was pressed using a force of 4 kN, which equates to a pressure of 204 MPa. Thereafter, the pellets were isostatically pressed by cold isostatic pressing (CIP) to obtain denser green bodies prior to sintering. A hydrostatic pressure of 2 $kbar$ was applied, with a holding time of 1 min.

Dilatometry experiments were conducted to study the sintering behaviour of LLZO. Platinum foil was used to avoid reactions with the alumina components in the tube furnace, the setup is sketched in Fig. 3.3. The heating and cooling rates were both set to $120\,°C\,h^{-1}$. The pellets were heated to 1250 °C, followed by a 1h isothermal

step. The atmosphere was synthetic air, and the gas flow rate was 30 $ml\,min^{-1}$.

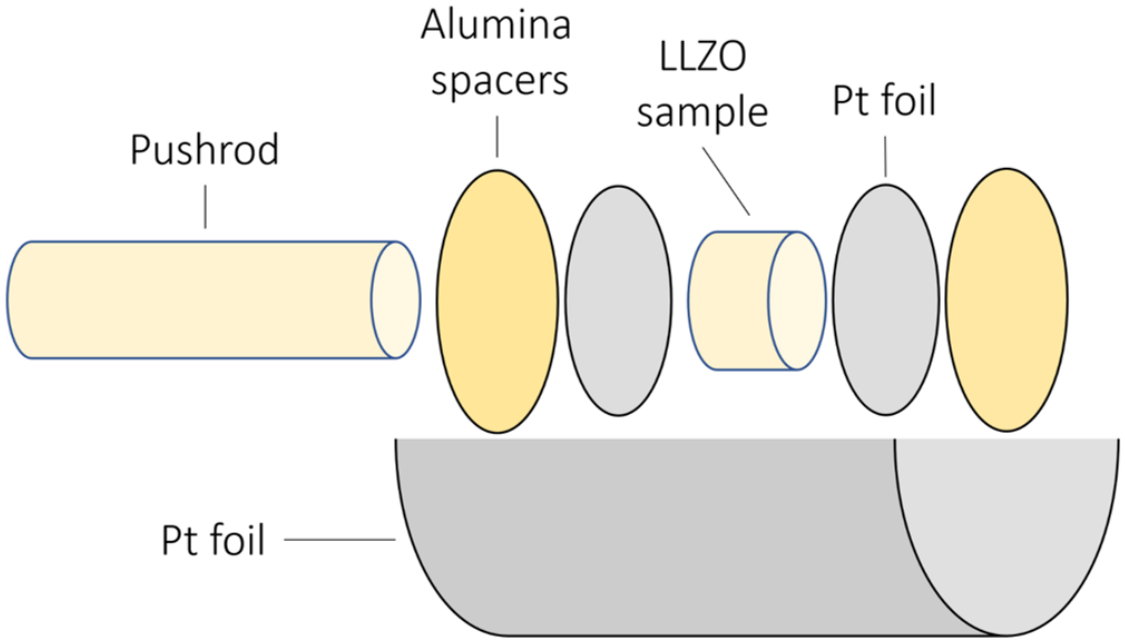

Figure 3.3. Schematic of the dilatometry setup.

3.2.4 Sintering

Calcined powders were pressed to pellets by double-action uniaxial pressing, the pressing tools were lubricated similarly to the dilatometry samples. The pellet mass was approximately 350 mg and the diameter was 10 mm. The powder was pressed using a force of 15 kN, which equates to a pressure of 191 MPa. Subsequently, the pellets were pressed with CIP similarly to the dilatometry samples.

The pellets were sintered to increase the density and to obtain a material suitable for electrolyte usage. Sintering experiments were conducted in ambient atmosphere at temperatures of 1000 °C and 1150 °C. Lids were placed on the crucibles to limit the loss of Li. Sintering was performed in alumina crucibles, hence bed powder was used to physically separate the pellets from the crucible and to avoid any undesired reactions. The mass of bed powder per mass of pellet is the bed powder ratio (BP-ratio). Fig. 3.4 shows the experimental setup for sintering with different BP-ratios. For BP-ratio = 2 the pellet is buried in bed powder, and for BP-ratio = 1/3 the pellet is not. In the case of no bed powder (BP-ratio = 0), the pellet

was physically separated from the crucible by balancing on a previously sintered LLZO fragment. Different sintering programs (SPs) were investigated, all sintering programs are detailed in Table 3.4. All samples were cooled to 500 °C in the furnace, and were then cooled to RT in a desiccator to avoid any reactions with humidity in the air. The mass, diameter, and thickness of the pellets were measured before and after sintering.

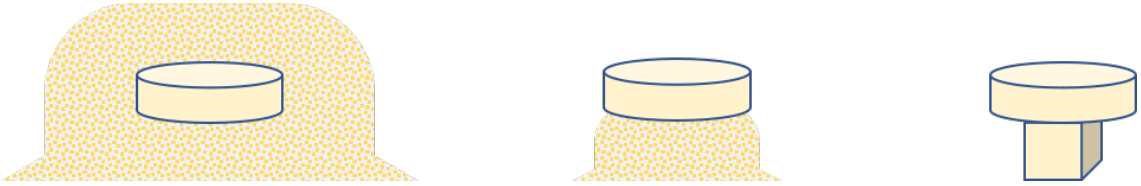

Figure 3.4. Schematic of the sintering setup for samples with BP-ratios of 2, 1/3 and 0 (left to right).

The density of the sintered pellets was determined by Archimedes' principle, according to the ISO 5017:1998 international standard [51]. The pellets were put in a vacuum chamber to remove air from the pores, before being submerged in isopropanol. The dry mass, the submerged mass, the wet mass, and the solvent temperature were measured for each sample (included in Appendix A).

3.2.5 X-ray diffraction

The phase composition was characterised using XRD. Diffraction patterns were collected at ambient conditions, using copper $K\alpha$ radiation with a wavelength $\lambda = 1.5406\ \mathring{A}$. The reflection geometry was Bragg-Brentano, and variable slits were used to increase counts at higher angles. The patterns were collected in the range $2\theta \in [15°,\ 75°]$.

Two different sample preparations were used for XRD. Bulk analysis of sintered pellets was performed by crushing the pellet in a steel pellet crusher. The resulting powder was suspended in ethanol and put on a Si-flat sample holder using a pipette. A thin film formed on the Si surface after the ethanol evaporated. Surface analysis of sintered pellets was also performed. This was done by placing the pristine pellet in a deep sample holder on top of plasticine for levelling purposes.

Table 3.4: Sintering programs utilised in this work. HR=Heating rate, T_H=Holding temperature, t_H=Holding time, CR=Cooling rate, BP-ratio=Bed powder ratio.

Sintering program	HR $[^\circ C\,h^{-1}]$	T_H $[^\circ C]$	t_H $[h]$	CR $[^\circ C\,h^{-1}]$	BP-ratio
SP-A	200	1000	1/2	200	2
	200	1000	1	200	2
	200	1000	2	200	2
	200	1000	6	200	2
SP-B	200	1150	1/2	200	2
	200	1150	1	200	2
	200	1150	2	200	2
	200	1150	6	200	2
SP-C	200	1150	1/2	400	1/3
	200	1150	2	400	1/3
	200	1150	6	400	1/3
SP-D	200	1150	1/2	400	0

The XRD patterns were indexed using the DIFFRAC.EVA V4.2 (Bruker AXS) software, and the reference patterns used for phase identification were provided by the 2020 ICDD PDF-4+ database [52]. Table 3.5 contains the number of all the PDF-4+ cards used to index patterns in this thesis. These are the same reference patterns which are included in figures in Section 4, though small diffraction peaks are not included in these figures to increase the readability. All diffraction patterns presented in this thesis are background subtracted and normalised based on the highest intensity peak.

Table 3.5: The PDF-4+ cards of reference patterns utilised in this work.

Phase	Formula unit	PDF-4+ card number
Al-LLZO	$Li_{6.28}Al_{0.24}La_3Zr_2O_{12}$	01-084-7686
c-LLZO	$Li_7La_3Zr_2O_{12}$	00-063-0174
t-LLZO	$Li_7La_3Zr_2O_{12}$	00-064-0140
Pyrochlore	$La_2Zr_2O_{12}$	01-070-5602
Li_2CO_3	Li_2CO_3	00-022-1141
$LaAlO_3$	$LaAlO_3$	01-078-2856
Li_2O	Li_2O	01-073-0593
ZrO_2	ZrO_2	00-037-1484
Li_2ZrO_3	Li_2ZrO_3	00-033-0843

Quantitative phase analysis was performed by Rietveld refinement of XRD patterns using the TOPAS V5.0 (Bruker AXS) software. Crystallite size, lattice parameters, and isotropic atomic displacement parameters were refined, while atomic positions and site occupancies were not.

3.2.6 Scanning electron microscopy & element analysis

The microstructure of sintered pellets was studied by SEM. Both secondary and backscattered electrons were used for imaging. Pristine pellet surfaces, pristine fracture surfaces, and polished fracture surfaces have all been investigated.

The chemical composition was studied by EDS and WDS. An accelerating voltage of $10\,kV$ was used for both analyses, which is sufficient to produce $K\alpha$ or $L\alpha$ characteristic X-rays from all the relevant elements, while still limiting the emission volume. EDS was performed in the SEM and WDS was performed by Morten Peder Raanes at NTNU using an electron probe micro analyser (EPMA).

Neither EDS nor WDS are able to detect Li. However, for the WDS measurements

the matrix (ZAF) correction was performed by considering the presence of Li, which should improve the accuracy of quantitative measurements. The measured counts are compared to defined standards, hence the missing counts can be quantified. Li is added as the difference, which means that all the missing counts are ascribed to Li.

3.2.7 Electrochemical impedance spectroscopy

EIS was conducted to determine the ionic conductivity of samples. Sintered pellets were polished by hand using sandpaper (European grit #320-#2400). The top and bottom of the pellet were sputter coated with Au, which acts as Li^+ blocking electrodes. A sketch of this setup with approximate dimensions is shown in Fig. 3.5.

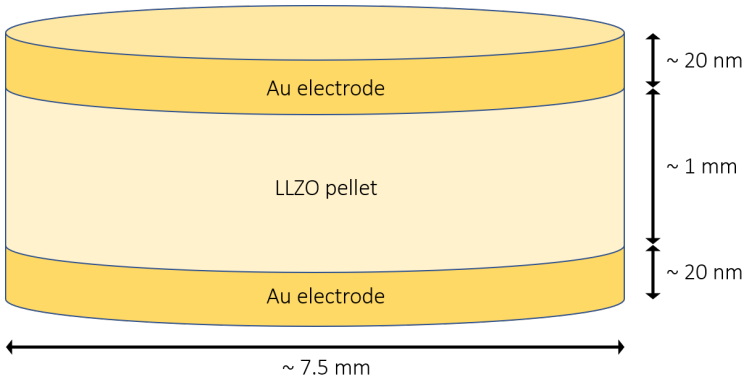

Figure 3.5. The experimental setup for EIS. Typical sample dimensions are indicated (not to scale).

The ionic conductivity of the samples was measured by EIS with a two-electrode setup. The frequency range was 7 $MHz - 100\ Hz$, the sinusoidal voltage amplitude was 20 mV, and the temperature was 20°C. The resistance of the samples was found by fitting the impedance data with one of the equivalent circuits shown in Fig. 3.6. The EC-Lab V11.31 (BioLogic) software was used to fit the experimental data to the respective equivalent circuit. The difference between the two circuits is whether the response from the bulk and grain boundaries are modeled together or individually. The circuit in Fig. 3.6a model the total response (bulk + grain boundary) as one resistance (R) and constant phase element (Q) in parallel, while the circuit in Fig.

3.6b treat the two contributions separately. The last (RQ) parallel represents the Au electrodes in both circuits.

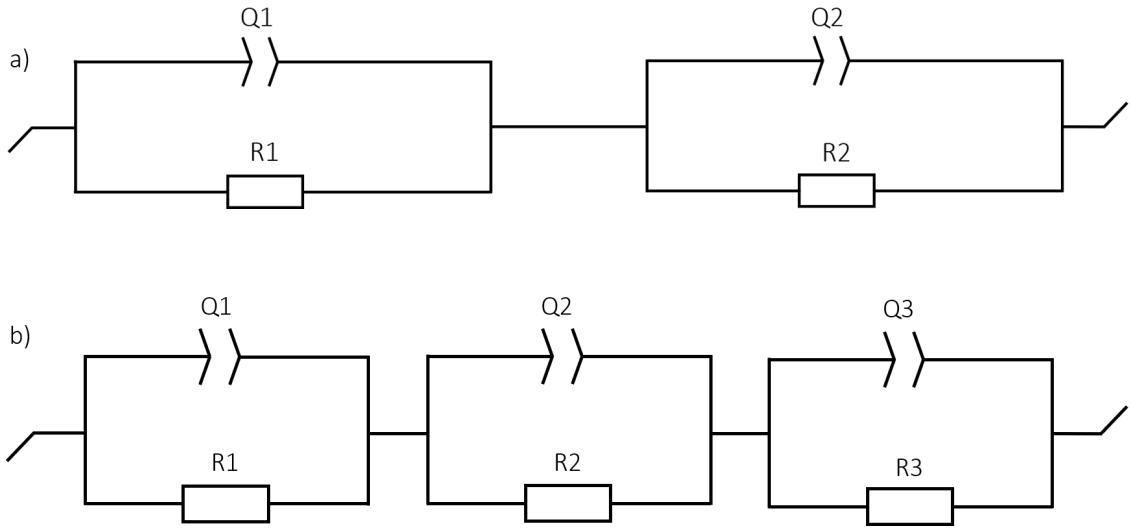

Figure 3.6. The equivalent circuits used to fit impedance results in Nyquist diagrams for (a) samples with inseparable contributions from bulk and grain boundaries and for (b) samples with discernible grain boundary contributions. R is a resistor and Q is a constant phase element.

4 Results

In this section, the most significant results on sintering and transport properties of Al-LLZO will be presented. This includes: documentation of the densification taking place during sintering, SEM micrographs which depict the microstructures, X-ray diffractograms and quantitative element analysis which detail the phase composition, and EIS measurements which yield the ionic conductivity of the sintered samples.

4.1 Calcination

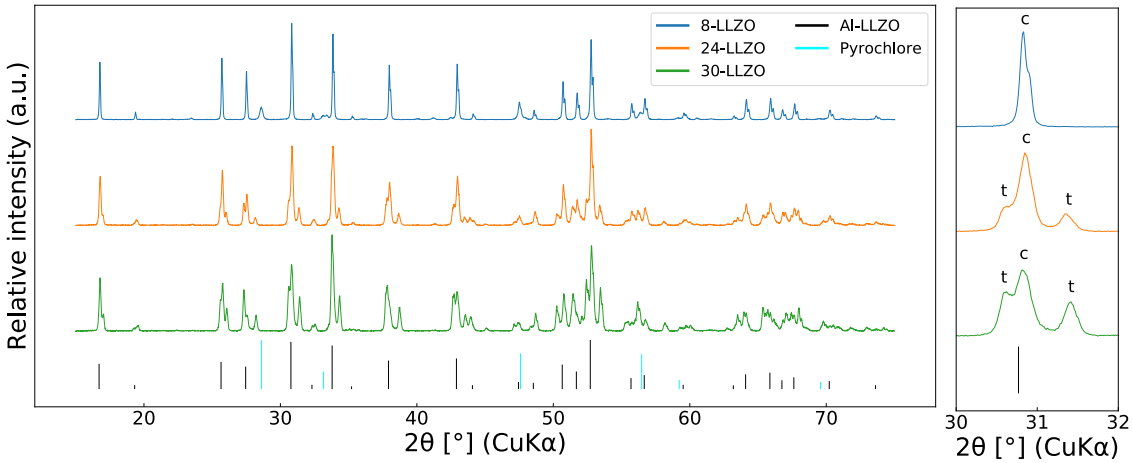

Figure 4.1. Diffraction pattern of powder calcined at 750 °C for 6h. All peaks belong to cubic LLZO, tetragonal LLZO (marked with c and t respectively in the inset on the right), or pyrochlore. As previously measured by Eriksen [10].

Fig. 4.1 shows the X-ray diffraction patterns of calcined powders with three different stoichiometries. These diffraction patterns were previously measured in a specialisation project by Eriksen [10]. They show that after calcination at 750 °C for 6h, a mixture of tetragonal and cubic LLZO forms in 24-LLZO and 30-LLZO. In the inset on the right, the cubic and tetragonal peaks are indicated. The cubic reflection is always in the middle at the same angle as the reference pattern, with two adjacent tetragonal peaks at slightly higher and lower angles. The relative amount of tetragonal phase LLZO is higher in 30-LLZO than 24-LLZO, judging from the relative peak intensities. 8-LLZO however, consists of cubic phase LLZO and a secondary

pyrochlore phase. By Rietveld refinement, pyrochlore was determined to constitute 11 wt% (with a $R_{wp} = 20.3$). As for all diffraction patterns shown in this section, only the reference pattern of cubic Al-doped LLZO is included in the figure in order to increase the readability, the presence of tetragonal phase LLZO is evidenced by the peak splitting.

4.2 Sintered pellet density

The dilatometry results in Fig. 4.2 show the change in the length of cylindrical LLZO pellets as a function of temperature, followed by a 1h isothermal step at 1250 °C. The densification behaviour of 24-LLZO and 30-LLZO is similar, and deviates significantly from 8-LLZO. Whereas 8-LLZO experiences two separated densification steps, both 24-LLZO and 30-LLZO have three discernible densification steps. Densification of 8-LLZO requires higher temperature than the other two stoichiometries. Densification of 24-LLZO and 30-LLZO stagnate before reaching the holding temperature, whereas the slope of the 8-LLZO curve is still rather steep at 1250 °C. At around 1050 °C, rapid densification takes place in 24-LLZO and 30-LLZO samples.

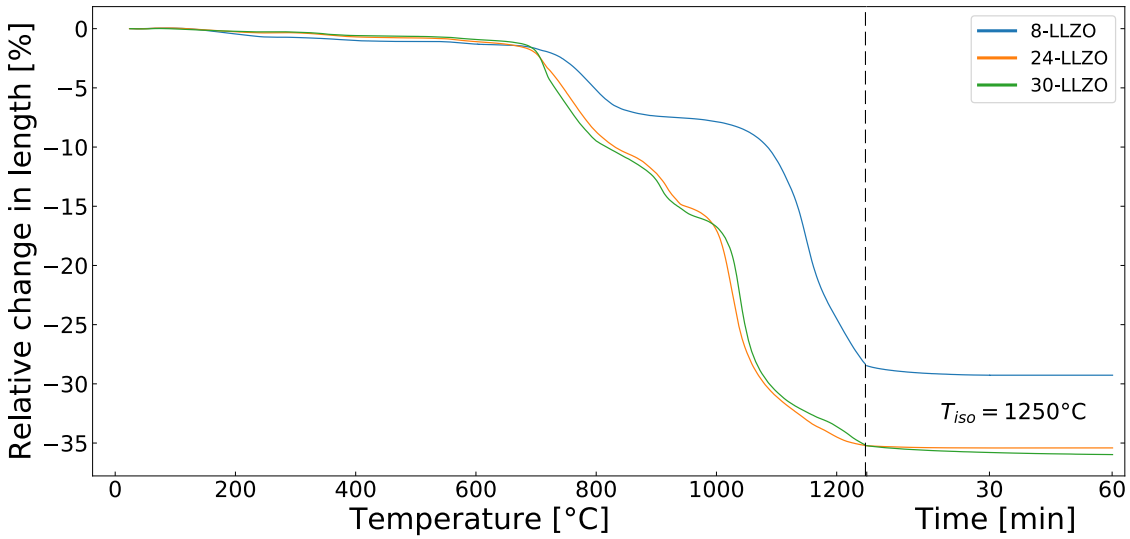

Figure 4.2. The change in length of cylindrical pellets was measured with dilatometry during sintering in synthetic air. After reaching the holding temperature of 1250 °C, the samples were held at this temperature for 1h, hence the split abscissa.

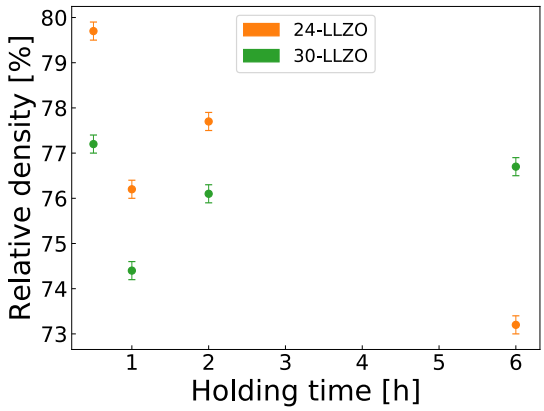

(a) SP-A ($T_H = 1000\,^{\circ}\mathrm{C}$, BP-ratio $= 2$)

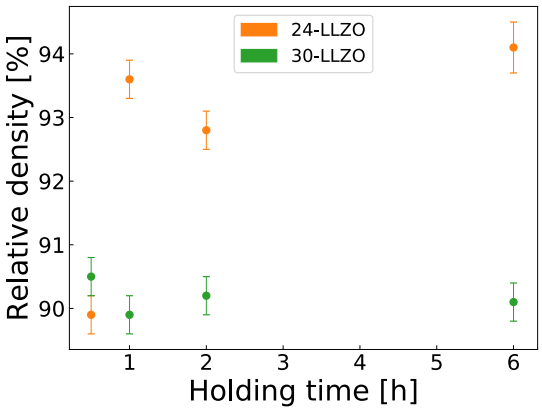

(b) SP-B ($T_H = 1150\,^{\circ}\mathrm{C}$, BP-ratio $= 2$)

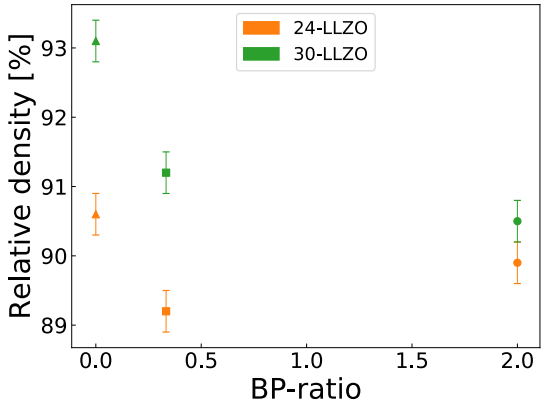

(c) $T_H = 1150\,^{\circ}\mathrm{C}$, $t_H = 1/2h$

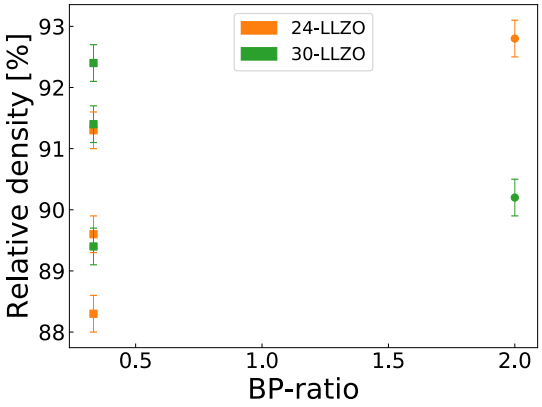

(d) $T_H = 1150\,^{\circ}\mathrm{C}$, $t_H = 2h$

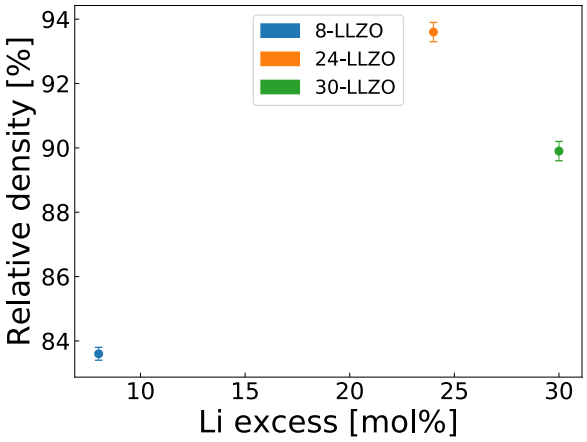

(e) SP-B ($T_H = 1150\,^{\circ}\mathrm{C}$, BP-ratio $= 2$) @ 1h

Figure 4.3. The RD of sintered pellets (a-b) as a function of sintering holding time, (c-d) as a function of BP-ratio, and (e) as a function of Li excess. The BP-ratio is denoted by the marker shape, where ● $= 2$, ■ $= 1/3$ and ▲ $= 0$. The densities were measured by Archimedes' method.

Figs. 4.3a and 4.3b show the RD of samples sintered with SP-A and SP-B. The only difference between these two SPs are the holding temperature of 1000 °C and 1150 °C respectively. The density is much higher for samples sintered with SP-B than for samples sintered with SP-A. In general, no significant increase in density is observed with increasing holding time for $t_H \in [1/2\text{h},\ 6\text{h}]$, with the one exception of 24-LLZO sintered with SP-B which has improved density after $t_H = 1/2$h. BP-ratio does not have a large impact on density either, as shown in Figs. 4.3c and 4.3d. Measurements of multiple samples sintered at 1150 °C with BP-ratio = 1/3 (Fig. 4.3d) reveal substantial difference in the resulting RD between similarly sintered samples. Fig. 4.3e shows that the RD of 8-LLZO is lower than for similarly sintered samples with higher Li excess.

4.3 1000 °C sintered pellets

Fig. 4.4 shows the surface morphology of pellets sintered at 1000 °C. Holding time at 1000 °C has little impact on the surface morphology (see Appendix C), hence the micrographs presented here are representative of all the SP-A sintered samples. Two qualitatively different microstructures were observed, one without a solidified liquid phase (Fig. 4.4a) and one with a solidified liquid phase surrounding the grains (Fig. 4.4b).

The pristine fracture surface of 30-LLZO pellets sintered with SP-A @ 1/2h and SP-A @ 6h are shown in Fig. 4.5. These micrographs show that the grain size is comparable between the two samples, and that there has been no significant grain growth due to the increased holding time. It is also clear that there is a higher tendency of transgranular fracture in the SP-A @ 6h sample than the SP-A @ 1/2h. However, the porosity is still high regardless of the holding time. Similar microstructures were observed in 24-LLZO (see Appendix C).

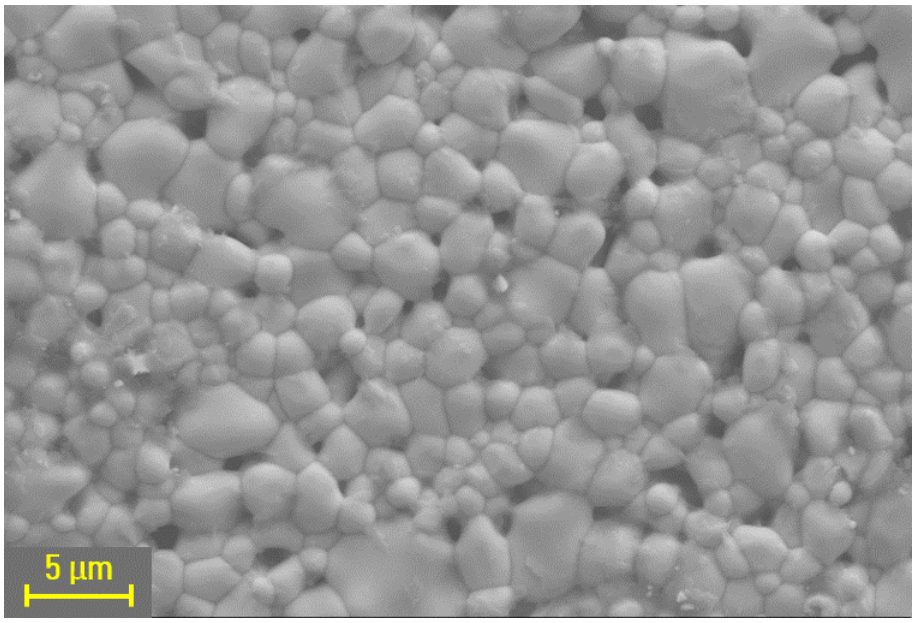

(a) 24-LLZO, SP-A @ 6h

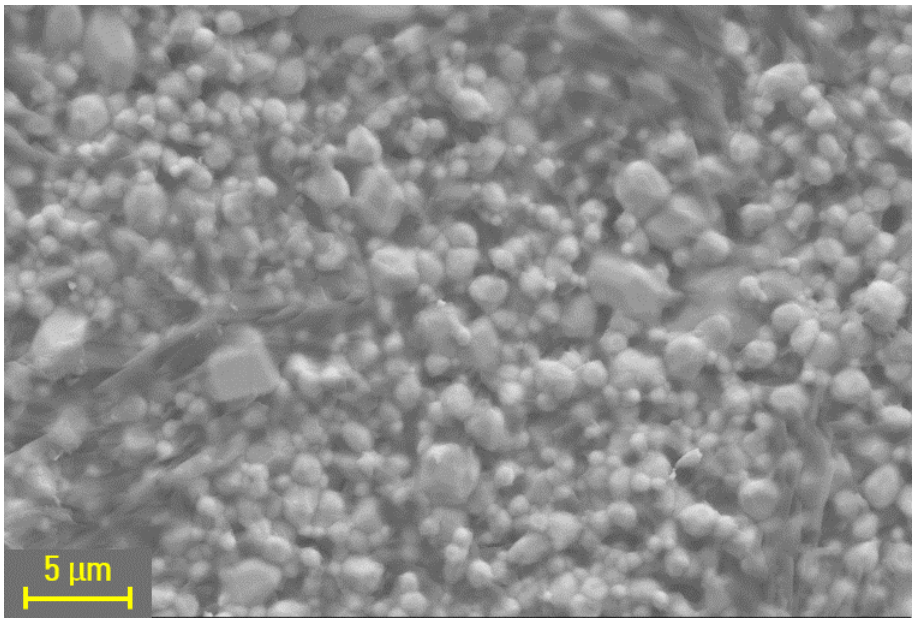

(b) 24-LLZO, SP-A @ 6h

Figure 4.4. Secondary electron micrographs of the microstructure of pristine pellet surfaces after sintering with SP-A ($T_H = 1000\,°\mathrm{C}$, BP-ratio = 2). Two qualitatively different microstructures were observed coexisting on the pellet surfaces: (a) one without a solidified liquid phase, and (b) one with a solidified liquid phase surrounding the grains.

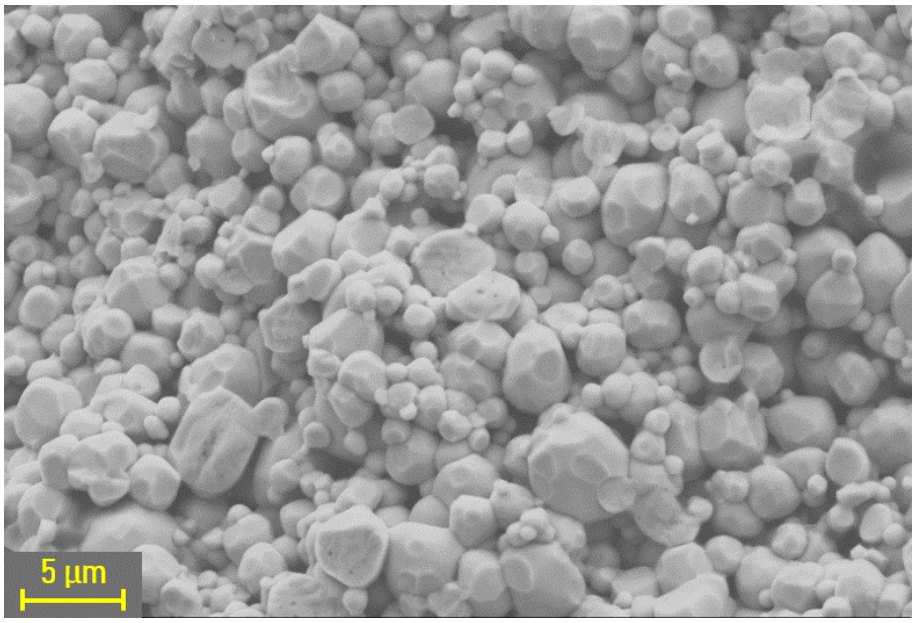

(a) 30-LLZO, SP-A @ 1/2h

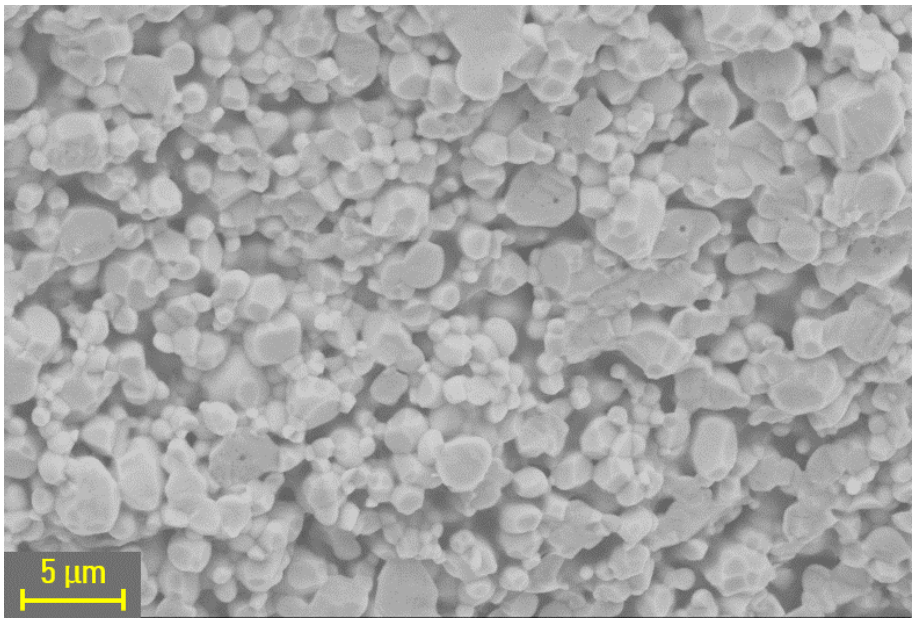

(b) 30-LLZO, SP-A @ 6h

Figure 4.5. Secondary electron micrographs of pristine fracture surfaces of pellets sintered with SP-A ($T_H = 1000\,°C$, BP-ratio = 2).

The XRD patterns of pellets sintered with SP-A @ 6h are shown in Fig. 4.6. These show that both 24-LLZO and 30-LLZO consist of a mixture of tetragonal and cubic LLZO phases after 6h of sintering. The phase composition after sintering with shorter holding times is also a mixture of cubic and tetragonal LLZO (shown in Appendix B).

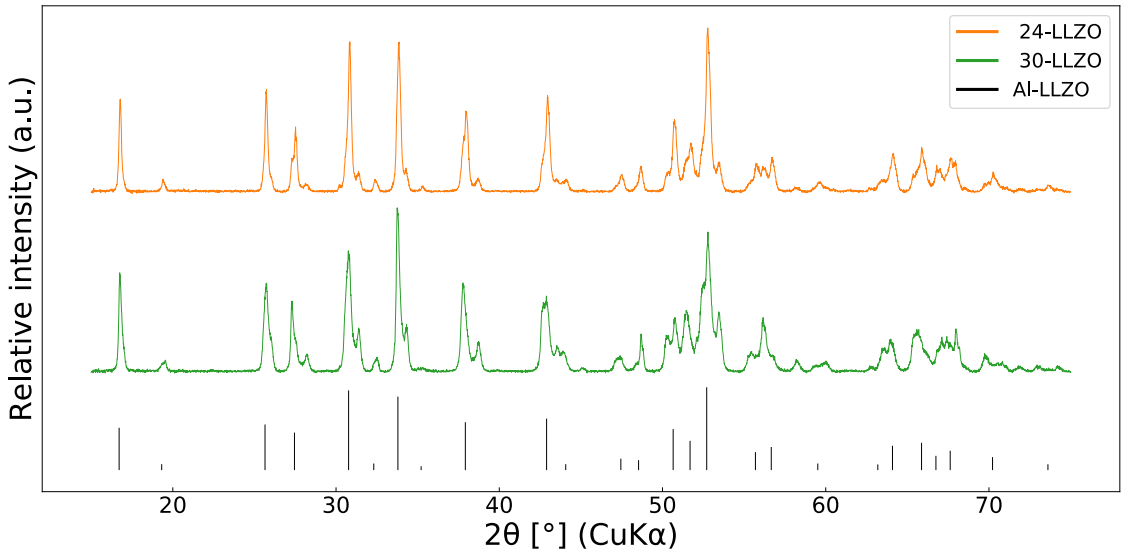

Figure 4.6. Bulk representative diffraction patterns of samples sintered with SP-A (T_H = 1000 °C, BP-ratio = 2) @ 6h. All peaks are indexed to tetragonal or cubic LLZO.

4.4 Microstructure of 1150 °C sintered pellets

The surface morphology of two pellets sintered with SP-B @ 1h is shown in Fig. 4.7. It is obvious that 24-LLZO experience AGG at 1150 °C, while 8-LLZO does not. The average grain size of 8-LLZO is a couple of microns, while 24-LLZO has grains which have grown several hundred microns wide. The grain size showcased in Fig. 4.7b is representative for all 24-LLZO and 30-LLZO samples sintered at 1150 °C (see Appendix C).

Fig. 4.8 shows the microstructure of 30-LLZO sintered with various holding times with SP-B. After 1/2h, there are large grains at the surface, and small grains in the centre of the pellet. As holding time increases, the fraction of the cross section with small grains decreases. The grain size in the centre of the pellet does not change significantly for $t_H \in [1/2\text{h},\ 2\text{h}]$. From the high magnification micrographs, it is apparent that the small grains in the centre area experience almost exclusively intergranular fracture. After 6h at 1150 °C, there are no small grains left in the centre; instead there is a large void remaining in the centre of the pellet. Similar sintering behaviour is observed in 24-LLZO and is shown in Appendix C.

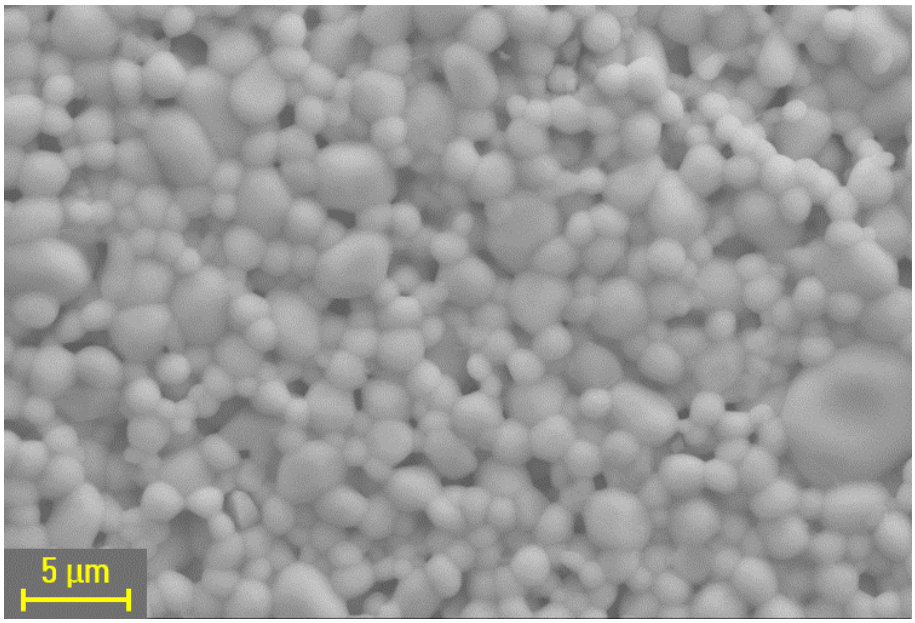

(a) 8-LLZO

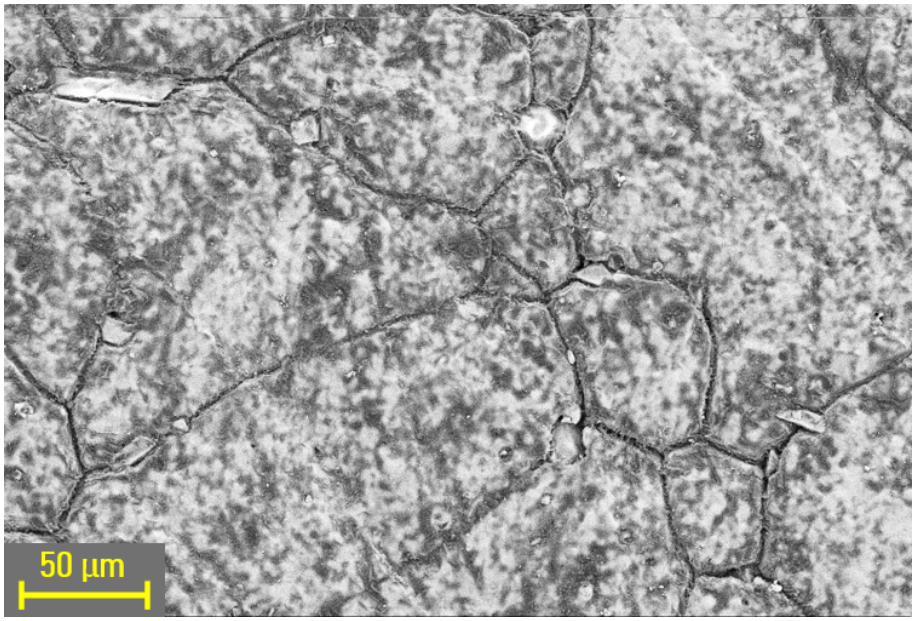

(b) 24-LLZO

Figure 4.7. Surface micrographs of (a) 8-LLZO and (b) 24-LLZO sintered with SP-B (T_H = 1150 °C, BP-ratio = 2) @ 1h which show the difference in grain size. Note the difference in magnification.

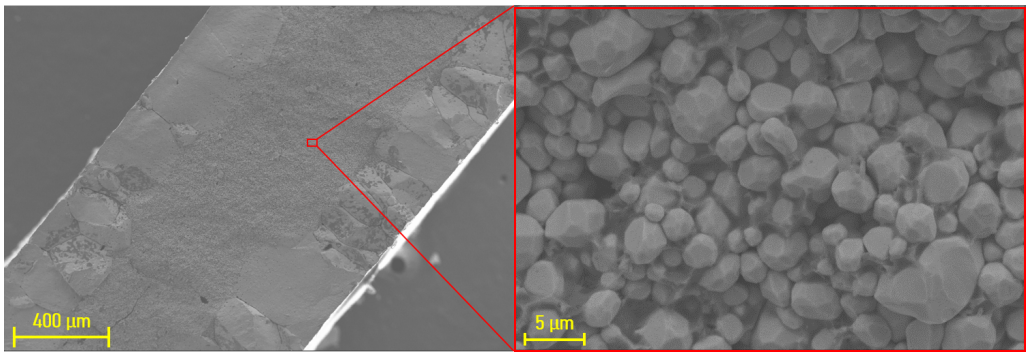

(a) SP-B @ 1/2h, low mag **(b)** SP-B @ 1/2h, high mag

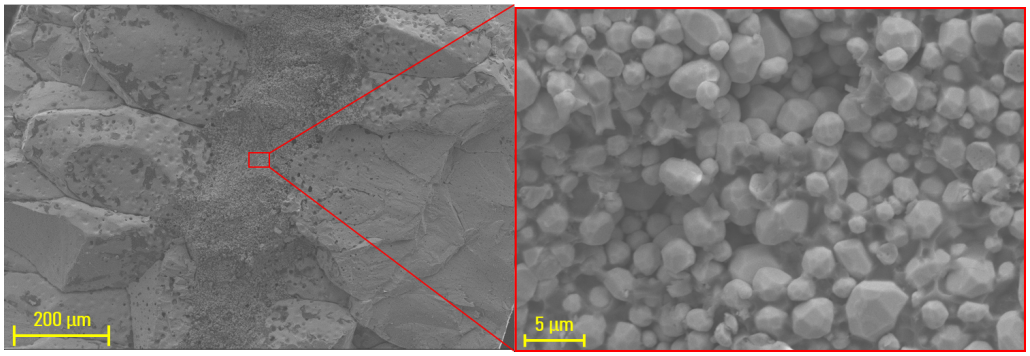

(c) SP-B @ 1h, low mag **(d)** SP-B @ 1h, high mag

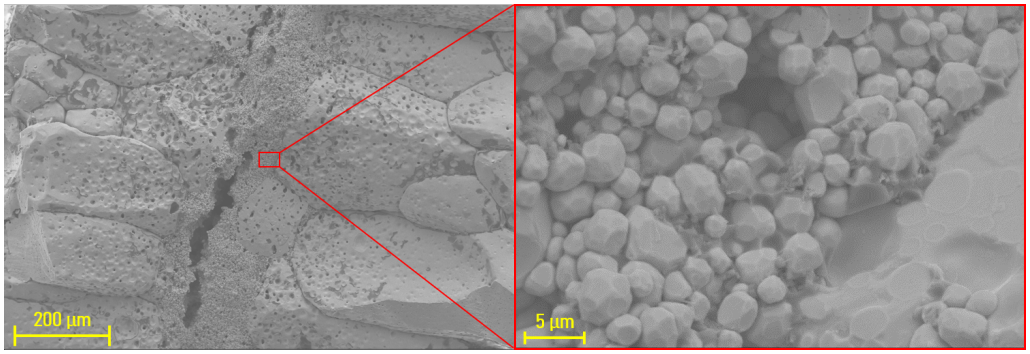

(e) SP-B @ 2h, low mag **(f)** SP-B @ 2h, high mag

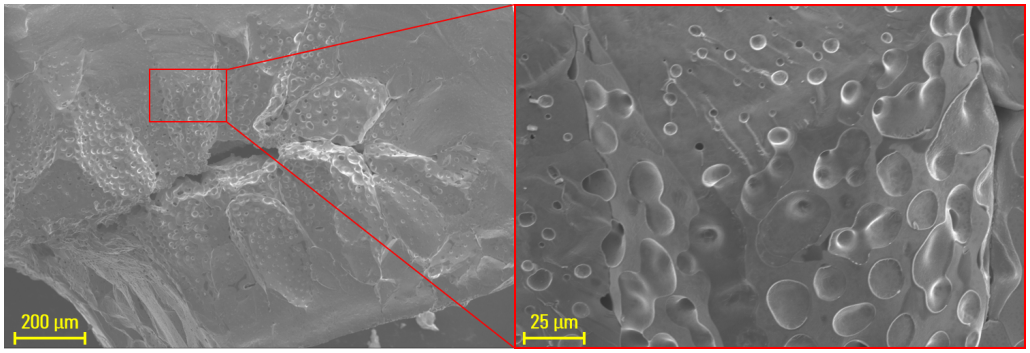

(g) SP-B @ 6h, low mag **(h)** SP-B @ 6h, high mag

Figure 4.8. Secondary electron micrographs of the pristine fracture surfaces of 30-LLZO pellets sintered with SP-B ($T_H = 1150\,°C$, BP-ratio = 2).

4.5 Phase composition of 1150 °C sintered pellets

Fig. 4.9 shows the diffraction patterns of samples sintered with SP-B. After 1/2h, both 24-LLZO and 30-LLZO consist of a mixture of tetragonal and cubic phase LLZO. The relative fraction of the tetragonal phase decreases as holding time increases. The cubic phase is stabilised faster in 24-LLZO than in 30-LLZO. After 6h holding time, both 24-LLZO and 30-LLZO consist only of cubic phase LLZO.

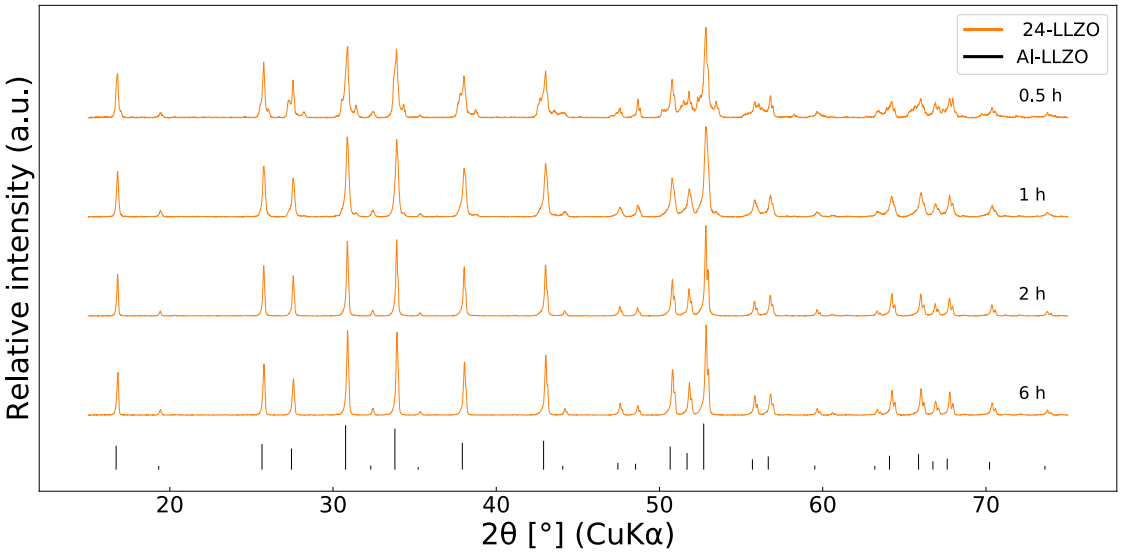

(a) 24-LLZO samples

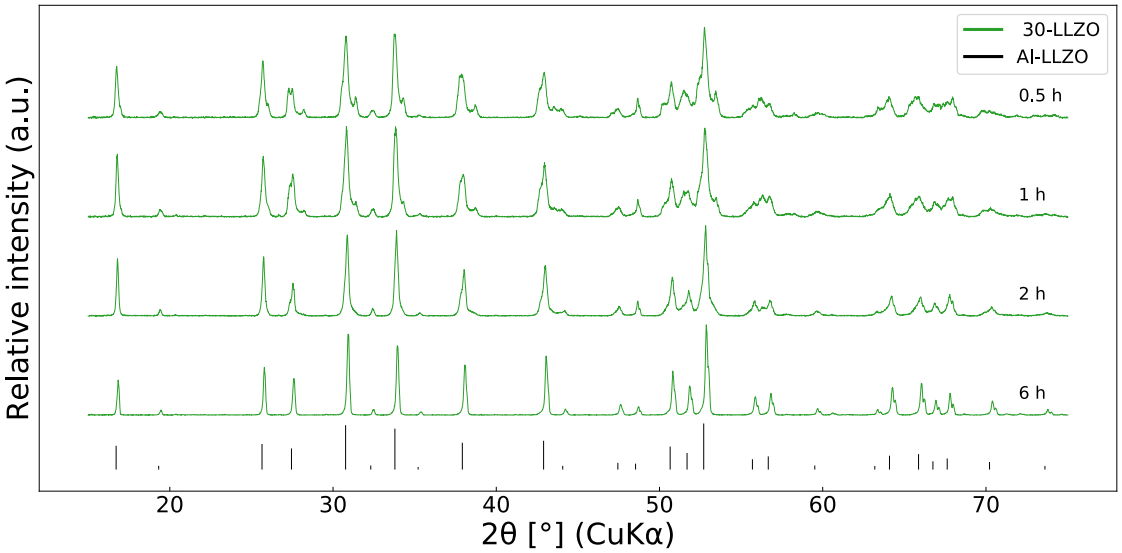

(b) 30-LLZO samples

Figure 4.9. Bulk representative diffraction patterns of samples sintered with SP-B (T_H = 1150 °C, BP-ratio = 2) with holding times $t_H \in$ [1/2h, 6h]. Only peaks belonging to tetragonal and cubic LLZO are present.

The diffraction patterns in Fig. 4.10a are collected from the surface of pellets sintered with SP-D @ 1/2h. The surface of the 30-LLZO pellet is shown in Fig. 4.10b. These patterns show high intensity reflections from the Li_2ZrO_3 secondary phase, in addition to the cubic LLZO phase. Also, there are several unidentified peaks in the diffractogram, the highest intensity ones are clearly marked. There is a secondary phase shaped like irregular grains along the grain boundaries. This secondary phase is commonly observed on the surface of pellets after sintering at 1150 °C.

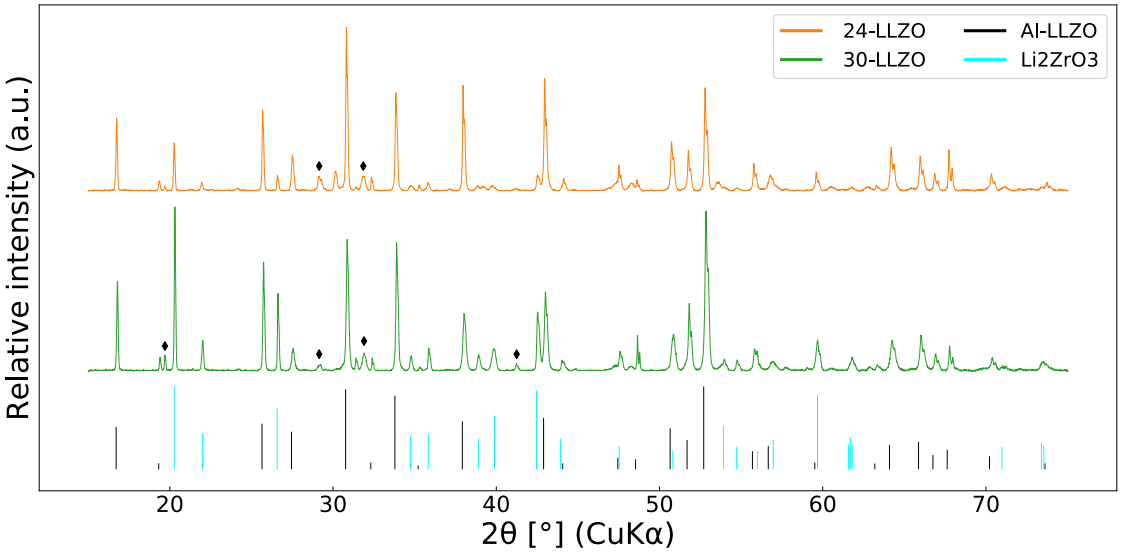

(a) Surface XRD, SP-D @ 1/2h

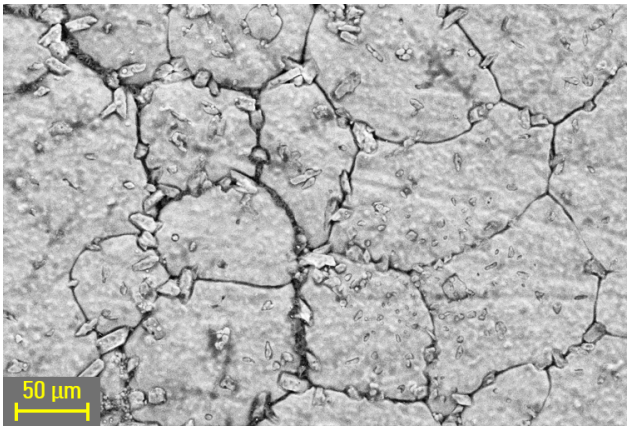

(b) SEM, 30-LLZO, SP-D @ 1/2h surface

Figure 4.10. Diffraction patterns (a) of the pristine pellet surfaces of SP-D (T_H = 1150 °C, BP-ratio = 0) @ 1/2h sintered pellets. Most peaks are indexed to Al-LLZO or Li_2ZrO_3, but there are multiple unidentified peaks. The highest intensity unidentified peaks are marked with ♦. Secondary electron micrograph (b) of the 30-LLZO sintered with SP-D @ 1/2h pristine pellet surface.

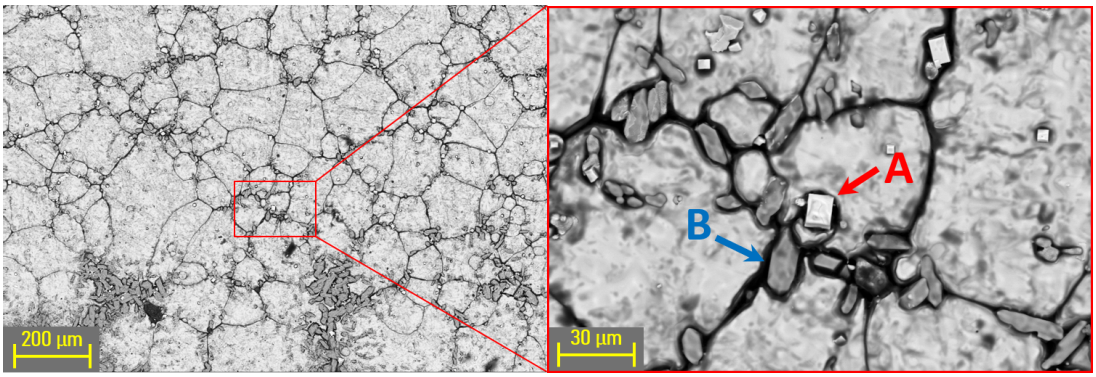

(a) 24-LLZO, SP-C @ 2h **(b)** 24-LLZO, SP-C @ 2h

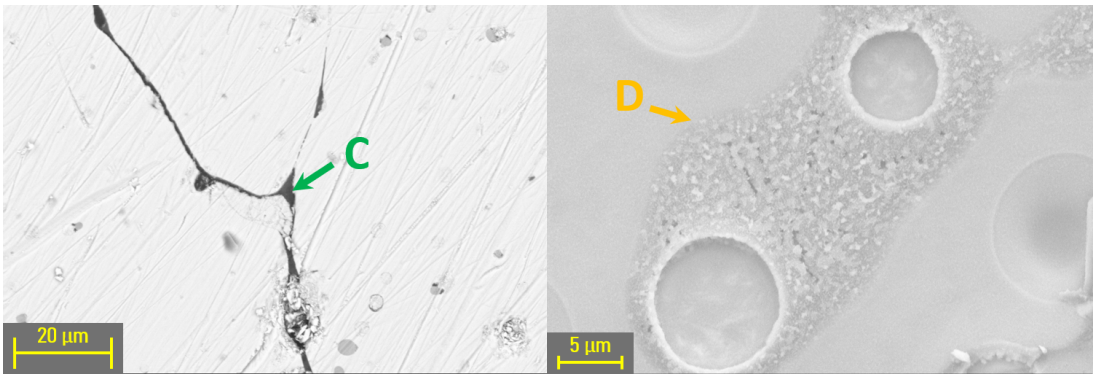

(c) 24-LLZO, SP-B @ 2h **(d)** 30-LLZO, SP-C @ 6h

Figure 4.11. Micrographs highlighting secondary phases in pellets sintered at 1150 °C with BP-ratios of 2 (SP-B) and 1/3 (SP-C). The backscatter electron micrographs (a-b) show cubes (red) and irregular grains (blue) on the pristine pellet surface. The backscatter electron micrograph of the polished fracture surface (c) shows a secondary phase (green) along the grain boundaries. The secondary electron micrograph of the pristine fracture surface (d) shows a secondary phase around the pores (orange). The composition of phases A-D was measured with EDS/WDS and are listed Table 4.1.

Table 4.1: The chemical composition of secondary phases shown in Fig. 4.11, the secondary phases are labeled A-D.

Phase	Measurement	Al [*mol*%]	Li [*mol*%]	La [*mol*%]	O [*mol*%]	Zr [*mol*%]
A (Red)	WDS	0	80 ± 2 [a]	0.1 ± 0.08	16 ± 2	4 ± 0.5
B (Blue)	EDS	0	0	0	78 ± 10	23 ± 4
C (Green)	EDS	31 ± 5	0	0	69 ± 4	0
D (Orange)	EDS	3 ± 5	0	0	97 ± 3	0

[a] Li is undetectable, the Li content was calculated.

Several secondary phases were observed in sintered LLZO samples using SEM, these secondary phases are shown in Fig. 4.11. While the micrographed sample is denoted in the figure, these micrographs are representative of all the samples sintered at 1150 °C. The composition of these phases were measured by EDS/WDS and are summarised in Table 4.1. Li is not detectable with EDS/WDS. For the WDS measurement Li content is reported, however this is only a calculated value, as described in Section 3.2.6. Secondary phases A and B were mostly located along grain boundaries at the surface of the pellets, as shown in Fig. 4.11a. An EDS map of the surface showing the elemental distribution is included in Appendix C, which confirms the results presented in Table 4.1. Secondary phase C is found along the grain boundaries of large grains, and secondary phase D forms around isolated pores which are trapped inside the large grains.

4.6 Ionic conductivity measurements

EIS measurements were conducted on sintered pellets in order to determine their ionic conductivity. The resulting Nyquist diagrams from these experiments are shown in Fig. 4.12. These are normalised Nyquist plots, meaning that the physical dimensions of the pellets have been factored in to make the results directly comparable between samples. The width of the semicircles corresponds to the resistivity of the pellets, hence smaller semicircles are associated with higher ionic conductivity. The width of these semicircles were determined by fitting the patterns with equivalent circuits (shown in Appendix D), the resulting ionic conductivity of the samples are summarised in Table 4.2. In general, 24-LLZO has higher total ionic conductivity than 30-LLZO. For both 24-LLZO and 30-LLZO, the highest ionic conductivity is obtained by sintering with SP-C @ 2h. This sintering program was therefore applied twice in order to investigate the reproducibility. The highest measured ionic conductivity value was $2.99 \cdot 10^{-4}$ Scm^{-1}, which was measured in a 24-LLZO sample sintered with SP-C @ 2h.

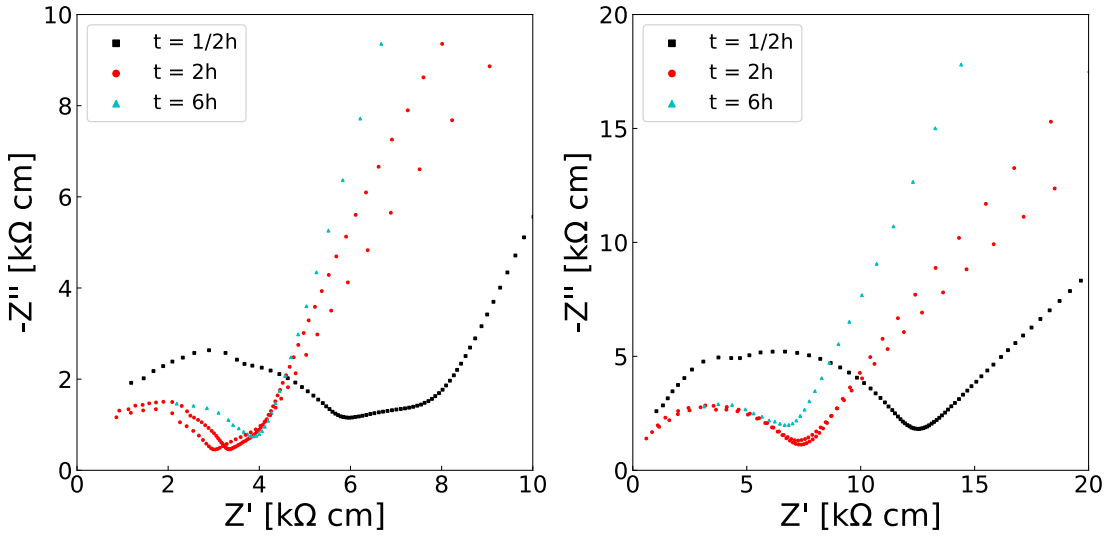

(a) 24-LLZO, SP-C

(b) 30-LLZO, SP-C

Figure 4.12. Normalised Nyquist diagrams for (a) 24-LLZO samples, and (b) 30-LLZO samples sintered with SP-C (T_H = 1150 °C, BP-ratio = 1/3). The SP-C @ 2h was employed twice. Z' is the real part and Z'' is the imaginary part of the impedance.

Table 4.2: The ionic conductivity of pellets sintered with SP-C (T_H = 1150 °C, BP-ratio = 1/3). The values are calculated from Nyquist diagram curve fits. t_H=Holding time, σ_{tot}=Total ionic conductivity.

t_H [h]	σ_{tot} [$\times 10^{-4}$ Scm^{-1}]	
	24-LLZO	30-LLZO
1/2	1.32 ± 0.04	0.88 ± 0.02
2	2.38 ± 0.07	1.44 ± 0.04
2	2.99 ± 0.09	1.54 ± 0.04
6[a]	2.5 ± 0.2	1.5 ± 0.1

[a] The pellet was polished rigorously before measurement.

The phase composition of the pellets used in EIS experiments are shown in the diffractograms in Fig. 4.13. 30-LLZO sintered for 1/2h has a clearly visible tetragonal LLZO phase, while all other samples only have peaks belonging to cubic phase LLZO.

As previously shown, samples sintered for 6h at 1150 °C have a large pore volume in the centre, which is expected to add to the resistance. Therefore, these samples were polished rigorously prior to the EIS measurements in order to remove the void. Fig. 4.14 shows how the SP-C @ 6h pellets were polished prior to EIS measurement.

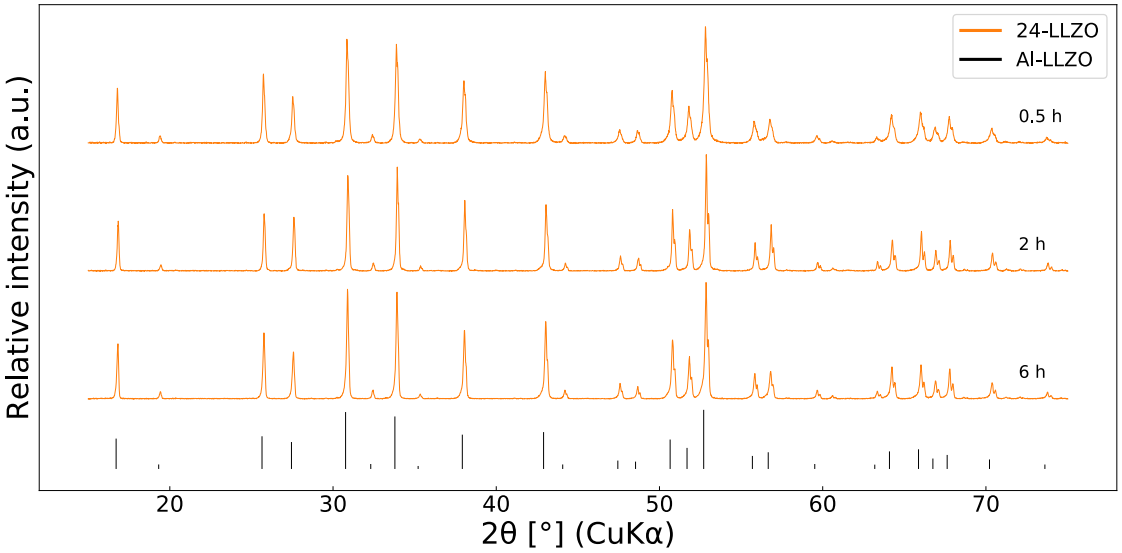

(a) 24-LLZO, SP-C

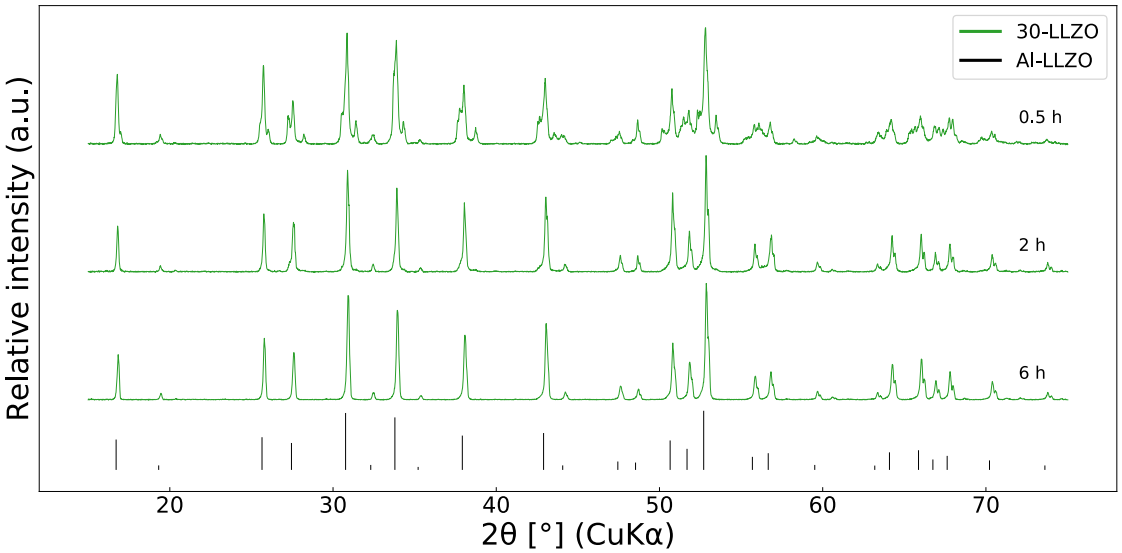

(b) 30-LLZO, SP-C

Figure 4.13. Bulk representative diffractograms showing the phase composition of samples sintered with SP-C (T_H = 1150 °C, BP-ratio = 1/3). These are the diffractograms of the samples which where used in EIS measurements. All peaks are indexed to tetragonal or cubic LLZO.

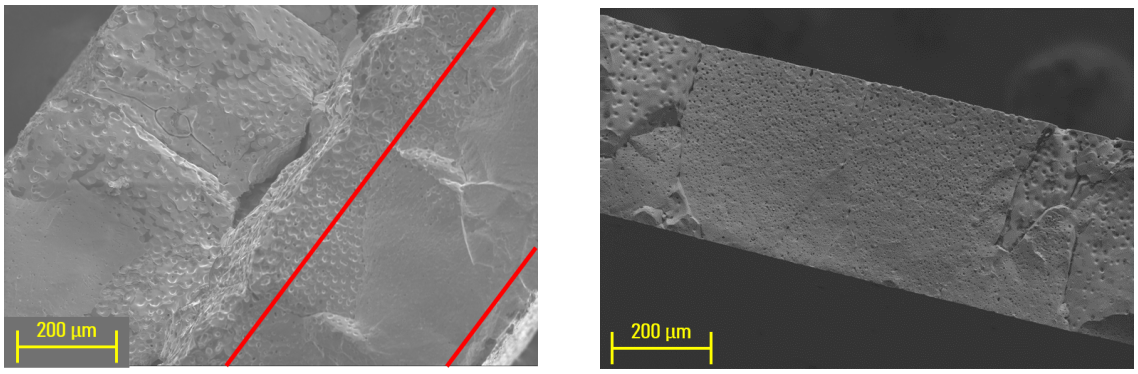

(a) 24-LLZO, SP-B @ 6h

(b) 24-LLZO, SP-C @ 6h

Figure 4.14. Micrographs showing the pristine fracture surface of pellets sintered at 1150 °C for 6h. After sintering there is a large void (a) in the middle of the pellet, similar to the void shown in the micrograph taken of the pristine fracture surface of the pellet sintered with SP-B ($T_H = 1150\,°C$, BP-ratio = 2) @ 6h. The red lines indicate how the as-sintered pellet was polished in order to remove this void. The micrograph (b) shows the cross section of the SP-C ($T_H = 1150\,°C$, BP-ratio = 1/3) sintered pellet used for EIS measurements, where the void was removed by polishing.

5 Discussion

5.1 Garnet phase composition

Powders with different stoichiometries were investigated in this work, where the Li excess was either 8 mol%, 24 mol%, or 30 mol%. The main motivation for varying the Li excess was to increase the likelihood of producing pure cubic phase LLZO. From literature it is evident that (i) controlling the phase composition and obtaining cubic phase LLZO is absolutely essential to obtain a material with good ionic conductivity, and that (ii) the Li content has a huge influence on the phase composition. While Li excess values reported in literature are seldom higher than 10 mol%, higher excess was applied in this work to compensate for losses during spray pyrolysis.

The fact that higher Li excess values are necessary with spray pyrolysis compared to other syntheses was previously verified by Eriksen [10]. As shown in Fig. 4.1, there are clearly visible pyrochlore peaks in the diffractogram collected from the calcined 8-LLZO powder. These peaks indicate that 8-LLZO is Li-deficient after calcination, because pyrochlore forms as a secondary phase when there is insufficient Li for LLZO formation. It is likely that the 8-LLZO powder was Li-deficient already after the spray pyrolysis, which implies that the Li-loss during spraying is > 7.4 mol%. Ascribing the entire Li-loss to the spray pyrolysis rather than the subsequent calcination step is probably a good approximation. Little Li-loss has been observed in this work at the calcination temperature of 750°C, and no mentions of substantial Li-loss at such low temperatures are found in the literature on LLZO. Assessing the Li content after spray pyrolysis was attempted by Rietveld refinement of the XRD pattern (Fig. B.1), but this was proven difficult due to the coexistence of many Li-containing phases with varying crystallinity. The results were unreliable, which is why using the diffractogram of the calcined powder (Fig. 4.1) is therefore a better estimate of the Li-loss during spray pyrolysis.

Due to the Li-deficiency of 8-LLZO after spray pyrolysis, the focus of this study has been on the powders with higher Li excess values. Both 24-LLZO and 30-LLZO

showed initial promise, and sintering experiments have focused on these two stoichiometries. After calcination, there is a surplus of Li in the garnet structure for both 24-LLZO and 30-LLZO. This surplus is evident from the peak splitting in Fig. 4.1, which is caused by the presence of the tetragonal LLZO phase. There are three reflections from each family of planes, therefore the LLZO garnet consists of a mixture of cubic and tetragonal phase. The cubic phase is stabilised through Li vacancies, and too high Li content will fill these vacancies and form tetragonal phase LLZO. However, high Li content after calcination is not a problem, and might actually be beneficial. Li-loss is commonly observed during sintering at high temperatures, and the Li surplus can act as a hedge towards this loss.

From the diffraction patterns shown in Fig. 4.6 it is obvious that sintering at 1000 °C for 6h was insufficient to produce pure cubic phase LLZO. The peak splitting in these patterns is caused by the tetragonal phase. This was the longest applied sintering time at 1000 °C, and still the Li-loss was insufficient to produce pure cubic phase LLZO. Judging from the other diffraction patterns collected of SP-A samples sintered with shorter holding times (Fig. B.2), the tetragonality seems to decrease slightly with holding time. This suggests that some Li-loss occurs, and that it is possible to stabilise the cubic phase at holding times longer than 6h. However, as shown in Fig. 4.3a the density obtained at 1000 °C is unsatisfactory, which makes the sintering temperature of 1000 °C suboptimal. Hence, the appropriate Li excess amount should not be determined by the phase composition obtained at this temperature.

Unlike for sintering at 1000 °C, the Li-loss which occurs in the 1/2h to 6h time frame when sintering at 1150 °C is easily observable in the XRD patterns, shown in Fig. 4.9. There is a transition from a mixture of tetragonal and cubic phase LLZO to pure cubic LLZO in both 24-LLZO and 30-LLZO. In order for this transition to take place, Li must leave the garnet phase and Li vacancies must form. Out of the three mechanisms of Li-loss in the garnet (outlined in Section 2.2.4), it is likely that formation of VLCs is the main contribution to loss at such a high temperature. This is because the samples were not in direct contact with the crucibles, and there was no obvious increase in Li-rich secondary phases at higher sintering times. The Li-loss

increases predictably with sintering time, and after 2h the 24-LLZO consists purely of cubic phase LLZO. 30-LLZO has more Li in the structure, which is why stabilising the cubic phase takes more time. After 6h however, 30-LLZO also consists entirely of cubic phase LLZO.

5.2 Secondary phases

Judging from the XRD diffractograms of samples sintered with SP-B shown in Fig. 4.9, no observable impurity phases appear after sintering at 1150 °C, even at the maximum holding time of 6h. This is especially significant in 24-LLZO, where cubic phase LLZO was already stabilised after 2h, and no secondary phases are observed after 6h. If the Li-loss in 24-LLZO was as severe after the 2h mark as before the 2h mark, this would have resulted in pyrochlore formation. The absence of pyrochlore peaks in 24-LLZO after 6h indicate that either (i) the total Li-loss of the sample is significantly lower after tetragonal LLZO has converted into cubic LLZO, or (ii) that Li-loss from the garnet phase is significantly lower after tetragonal phase has been converted to cubic and that Li is supplied to the atmosphere by secondary phases instead. One could easily dismiss option (ii) as a possibility due to there being no visible secondary phases in the XRD patterns which could supply the atmosphere with Li, but from the SEM micrographs shown in Fig. 4.11 it is obvious that there are secondary phases present. Also, the concentration of secondary phases is substantially higher at the surface, as shown in the surface diffractograms in Fig. 4.10, where high intensity Li_2ZrO_3 peaks are present. With such a high concentration of Li_2ZrO_3 on the surface, it is possible that this secondary phase assists in saturating the atmosphere with VLCs. Regardless of why the rate of Li-loss decreases after the disappearance of the the tetragonal LLZO phase, the fact that no pyrochlore peaks are observed is encouraging. These results show that there are a range of different sintering times which can produce pure cubic phase LLZO.

Several secondary phases have been observed by SEM in sintered samples, despite XRD patterns generally indicating that only tetragonal and cubic LLZO phases are present. The one exception to this is the XRD patterns in Fig. 4.10a, which

were collected from the surface of pellets sintered with SP-D @ 1/2h. In these diffractograms, Li_2ZrO_3 and an unidentified phase were visible in both 24-LLZO and 30-LLZO. All other XRD patterns included in Section 4 and Appendix B are bulk representative. The absence of visible secondary phases in bulk representative samples implies that the mass fraction of secondary phases is low, beyond the detection limit of XRD. Undoubtedly, the fraction of secondary phases are much higher at the pellet surfaces. Both the X-ray diffractograms and SEM micrographs collected throughout this work corroborates this. The fact that the vast majority of secondary phases are at the surface is beneficial: secondary phases reduce the ionic conductivity of the solid-state electrolyte, and by being located at the surface they can be removed by polishing.

The elemental composition of secondary phases A-D is shown in Table 4.1. While the quantitative results obtained with EDS/WDS are presented, this is mostly to illustrate that they are unreliable. Trusting the quantitative results would cause phase A and B to have formula units close to $Li_{20}ZrO_4$ and ZrO_3, which are obviously wrong as neither of these compounds are stable. In the case of the EPMA's ZAF correction it can be concluded that while its precision is high (the standard deviation in measurements is low), its accuracy is likely not; for EDS measurements the presence of undetectable Li can affect the ZAF correction which does not take Li into account when estimating the quantities. Li is a light element, which has little influence on ZAF corrections for La and Zr, but the presence of Li has a larger effect on lighter elements like O and Al. Therefore, it is more reasonable to consider these results as qualitative, and interpret any measured value significantly larger than zero as proof that the element is present rather than trusting the quantitative values. Keeping in mind that Li could always be present, the proposed formula units of phases A-D are listed in Table 5.1.

Both **phase A and B** (Fig. 4.11b) were observed primarily on the external surface of pellets sintered at 1150 °C, and are presumed to be Li_2ZrO_3: both because Li_2ZrO_3 is a stable compound and because Li_2ZrO_3 was observed at the surface with XRD (Fig. 4.10a). The possibility of either of these phases being ZrO_2 is rejected for two reasons: first, in the hypothetical absence of Li the quantitative element

Table 5.1: Proposed formula units of the secondary phases observed in samples sintered at 1150 °C. The phases are shown in Fig. 4.11. The formula units are based on EDS/WDS measurements provided in Table 4.1.

Phase	Observed	Proposed formula unit
A (red)	Surface, along grain boundaries	Li_2ZrO_3
B (blue)	Surface, along grain boundaries	Li_2ZrO_3
C (green)	Grain boundaries of large grains	$0.798\,Li_5AlO_4 + 0.202\,LiAlO_2$
D (orange)	Surrounding isolated pores	Li_2O

measurements should be more reliable and resemble a O:Zr ratio of 2, second, ZrO_2 was not observed in XRD. It is possible that only phase A or B is Li_2ZrO_3, but none of the other stable lithium zirconates (shown in Fig. 2.3) were observed with XRD. However, it is possible that the unidentified peaks in the surface diffractogram (Fig. 4.10a) belong to one of these two phases.

Phase C (Fig. 4.11c) is a Li-Al-O phase which is formed along the grain boundaries of large grains of samples sintered at 1150 °C. The melting point of the eutectic composition in the Li-rich part of the lithia-alumina system is 1064 °C (see Fig. 2.4), which is well below the sintering temperature of 1150 °C. This phase resemble a solidified liquid phase, hence this being Al_2O_3 is not a possibility, because the melting point of alumina is much higher than the sintering temperature. This phase has potentially huge implications on the sintering of Al-LLZO, which will be discussed later in more detail. While the best guess at the formula unit of this phase is the eutectic composition of $0.798\,Li_5AlO_4 + 0.202\,LiAlO_2$, any composition close to the eutectic where the melting point is below the sintering temperature is possible.

Lastly, **phase D** (Fig. 4.11d) which formed around isolated pores in large grains seems to consist only of oxygen in the EDS measurements, which obviously cannot be true. Most likely this phase was Li_2O, but because Li_2O is hygroscopic it is probable that LiOH formed due to exposure to the atmosphere prior to the time of measurement. Reaction with humidity could explain the fine porous structure of this phase. This phase was occasionally observed surrounding isolated pores, and is

therefore expected to have minimal impact on the transport properties of LLZO.

5.3 Densification

A major focus of this work has been to study the sintering behaviour of Al-LLZO in order to maximise the phase purity and RD of sintered pellets.

An initial impression of the densification in LLZO during sintering is provided by the dilatometry curves in Fig. 4.2. First, densification occurs at considerably higher temperatures in 8-LLZO than in the stoichiometries with higher Li excess. As the only difference between these materials is the Li excess, it is clear that higher Li content promotes sintering. Focusing only at 24-LLZO and 30-LLZO, there are three temperatures which the slope of densification increases: at approximately 700 °C, 900 °C, and 1000 °C.

Two sintering temperatures were applied in this work, 1000 °C and 1150 °C. These sintering temperatures correspond to just before and just after the last densification step observed in the dilatometry curves of 24-LLZO and 30-LLZO. The microstructure changes drastically during this final densification step. Micrographs of the surfaces of pellets sintered at 1000 °C (Fig. 4.4) show that limited grain growth has occurred, while micrographs taken of samples sintered at 1150 °C (Fig. 4.7b and Fig. C.3) show that samples have experienced AGG. Hence, AGG occurs simultaneously with the last densification step. However, that does not necessarily mean that the AGG is the cause of the densification. The 8-LLZO dilatometry curve (Fig. 4.2) shows that rapid densification occurs in 8-LLZO at 1150 °C, and 8-LLZO did not experience AGG at this temperature (Fig. 4.7a). Hence, substantial densification is possible without AGG.

Upon closer inspection of the grain boundaries along the large grains shown in Fig. 4.8, the secondary phase C (shown in Fig. 4.11c) was discovered. As discussed in Section 5.2, this is a Li-Al-O phase. The eutectic composition in the Li-rich part of the phase diagram (Fig. 2.4) has melting point of 1064 °C, which is right in the middle of the region where the last densification step occurs in 24-LLZO and 30-LLZO (Fig. 4.2), and below the applied sintering temperature of 1150 °C.

The existence of this phase enables liquid phase sintering, which greatly improves diffusion rates through viscous flow. The Li-Al-O phase located at the interphase between the large grains and the smaller grains is observable in Fig. 4.8f. The small pores isolated within the large grains also indicate that liquid phase sintering occurred, because the grain growth rate was high enough to trap these pores which presumably originated at the grain boundaries [37]. It is therefore proposed that the high growth rate of the large grains is due to dissolution of small grains into the liquid Li-Al-O phase and subsequent reprecipitation onto the surface of the large grains. Based on this sintering mechanism, avoiding AGG at these temperatures is analogous with avoiding the formation of the Li-Al-O phase. Considering that AGG did not occur in 8-LLZO samples, it seems like lowering the Li content also suppresses the formation of the Li-Al-O phase.

While AGG is not uncommon in Al-doped LLZO, it is more prevalent at higher temperature (T_H) and time (t_H). The formation of the Li-Al-O liquid phase explains why AGG is so severe. In this work, substantial AGG is present even after sintering at 1150 °C for 1/2h with a BP-ratio of 0 (shown in Fig. C.6). For reference, a summary of sintering conditions which did not cause AGG at higher T_H and t_H is provided in Table 5.2. Keep in mind though, that the Li excess values applied in other studies are not directly comparable to this work, due to the additional Li-loss occurring during the spray pyrolysis step discussed in Section 5.1. This discrepancy where AGG occurs at lower temperature in this work is explained by the high Li excess. High Li content promotes formation of the Li-Al-O phase, as evidenced by the absence of AGG in 8-LLZO. It is reasonable to assume that Al content, in addition to the Li content, affects the formation rate of Li-Al-O liquid phase. A study by Tian et al. [42] showed that increasing Al doping concentration in LLZO caused AGG to occur at lower temperatures. With 0.15-0.25 Al per formula unit, they observed AGG at 1180 °C, which is comparable to this work. It was not commented on by the authors, but this could be linked to the formation of Li-Al-O liquid phase. However, lowering the Al content to avoid AGG is not viable, because that would destabilise the cubic LLZO phase.

Table 5.2: Sintering conditions successfully applied in literature without AGG. pfu=Per formula unit, RD=Relative density.

T_H	t_H	Li excess	Al content	RD	Grain size	Ref.
1200 °C	6h	10 $mol\%$	0.37 pfu	86%	$5-20\ \mu m$	[40]
1200 °C	12h	10 $mol\%$	0.28 pfu	79%	N/A	[35]
1230 °C	6h	10 $mol\%$	0.25 pfu	90%	$5-20\ \mu m$	[39]
1300 °C	1h	5 $mol\%$	0.25 pfu	N/A	N/A	[18]

It is remarkable that AGG always starts at the surface and that the front of the large grains move towards the centre. While there are many instances of AGG in literature, no mentions of similar directional grain growth have been encountered by the author. This sintering behaviour is unfortunate, as it leaves behind a void in the middle of the pellet which in practice reduces the cross sectional area of the electrolyte available to Li^+ transport. It is possible that the solidified liquid phase which is observed on the surface of pellets sintered at 1000 °C (Fig. 4.4a) represents the early stages of this process. The pellets are very thin, hence there should be no temperature gradients which could have explained this. Instead, it was hypothesised that AGG starting at the surface might be due to contact with the Li-containing atmosphere. The main motivation for varying the BP-ratio, and thereby presumably the VLC concentration in the atmosphere, in this work was to verify whether the amount of bed powder affected the AGG. Results by Huang et al. [31] indicated that liquid condensation of VLCs on the surface is part of the sintering mechanism in LLZO, making the sintering mechanism a gas-liquid-solid process. Therefore, a reasonable explanation for the directional AGG is that the liquid Li-Al-O phase observed in this work forms when Al reacts with condensed VLCs on the pellet surface. However, lowering the BP-ratio had no noticeable impact on the rate of AGG, which was surprising considering that Huang et al. [31] and Yang et al. [36] observed enhanced AGG with increasing BP-ratio. The most obvious explanation for the low correlation between BP-ratio and AGG is that the high Li-excess of 24-LLZO and 30-LLZO easily saturates the atmosphere regardless of BP-ratio, and that BP-ratio therefore has limited impact on the actual VLC vapour pressure.

The difference in RD between samples sintered at 1000 °C and 1150 °C is significant, as expected form the dilatometry experiment. As shown in Fig. 4.3, increasing the sintering temperature increases the RD from below 80% to above 90%. No other sintering parameters have produced a similarly noticeable difference in RD. No correlation was found between varying BP-ratio and RD. Also, varying the sintering holding time in the range $t_H \in [1/2\text{h},\ 6\text{h}]$ did not produce any convincing correlations. It is tempting to conclude that the density of 24-LLZO sintered with SP-B (Fig. 4.3b) increases after $t_H = 1/2$h, but with only one data point this is difficult to justify; especially considering the large variation in RD between samples of the same parallel. Three similar samples were sintered with SP-C @ 2h (shown in Fig. 4.3d), and the RD varies between 88% and 93%. Therefore, it is more reasonable to assume that the RD is affected more by factors like variations in sample preparation, differences in sintering conditions, and measurement errors, rather than the sintering holding time.

High RD is achievable even at short holding times, and AGG is limited by reducing the holding time. Applying short holding times might therefore be a valid strategy to combat AGG without compromising the bulk density. A similar approach to the same challenge is to apply a two-step sintering process, where after applying a high temperature for a short time, further densification can take place at a lower temperature where AGG is inactive. In this case, that might be below the melting point of the eutectic in the lithia-alumina system (1064°C). Strategies which limit the holding time at high temperatures have been successfully implemented to avoid AGG previously, and are covered in the literature review (Section 2.4). Another approach to limiting AGG while still employing high sintering temperatures, is to limit the growth of grains by addition of grain growth inhibitors; while this is not common practice in Al-LLZO, it is a strategy which has been used to limit grain growth in other LLZO-dopant systems. The inhibitor must be inert, and ideally distribute at the triple junctions along the grain boundaries to ensure good grain contact and minimise the effect on ionic conductivity. A common inhibitor in niobium and tantalum doped systems is MgO [37, 49, 50], a similar strategy could be adopted in Al-LLZO if MgO remains inert in the presence of Al.

Liquid phase sintering being part of the Al-LLZO sintering mechanism was also hypothesised by Jin and McGinn [40], although no composition was provided for this liquid phase in their work. The liquid phase they observed was reported to promote sintering and allow for shorter sintering times, and it did not result in AGG. Hence, it is possible that Al-LLZO with lower Li excess is less prone to AGG resulting from the formation of the Li-Al-O liquid phase.

5.4 Ionic conductivity

The ionic conductivity of LLZO samples depends on the phase composition, microstructure, and density of the sintered pellets. Hence, the measured ionic conductivity values must be interpreted in light of the results which have been discussed previously in Section 5.

Before discussing the ionic conductivity results, an interpretation of the Nyquist diagrams is of relevance. Two qualitatively different spectra were observed in different LLZO samples, where either one or two quasi-semicircles form followed by a tail. In the case of two quasi-semicircles, the first one (in the high frequency region to the left) is attributed to bulk ionic resistivity within the grains and the second is attributed the grain boundary resistivity. This is because in LLZO, the bulk ionic resistivity is expected to be lower than the grain boundary resistivity, because cubic phase LLZO is an excellent Li^+ conductor [48]. In the other case with just one quasi-semicircle, the contributions from bulk and grain boundaries are not separable. Non-separable contributions implies that there is negligible grain boundary resistivity [35]. In either case, the quasi-semicircle(s) is (are) followed by a tail in the low frequency region. This tail stems from the polarisation of the Li^+ blocking electrodes.

In all the EIS experiments, 24-LLZO exhibits higher ionic conductivity than 30-LLZO under equal sintering conditions, as shown in Fig. 4.12 and Table 4.2. The reason for this is obvious for samples sintered for 1/2h: while 24-LLZO consists of pure cubic phase LLZO, 30-LLZO consists of a mixture of cubic and tetragonal LLZO (shown in Fig. 4.13). The presence of the tetragonal garnet phase in 30-LLZO

reduces the ionic conductivity. However, for samples sintered with $t_H \in$ [2h, 6h], both 24-LLZO and 30-LLZO have similar compositions according to XRD (Fig. 4.13). Still, the ionic conductivity of 30-LLZO is significantly lower than 24-LLZO, which is surprising. This can not be explained by density variations and grain boundary contact, as only one quasi-semicircle appears in 30-LLZO, which indicates that the grain boundary contribution is negligible compared to the bulk. For some reason not visible in XRD, the bulk ionic conductivity of 30-LLZO is considerably lower than 24-LLZO. The fraction of secondary phases is low in both 24-LLZO and 30-LLZO, hence the impact of these phases on the ionic conductivity is expected to be low. Despite the lack of a convincing explanation as to why, this essentially means that 24-LLZO is a superior electrolyte to 30-LLZO.

The Nyquist diagrams in Fig. 4.12 also reveal that $t_H = 2$h is the optimal sintering holding time at 1150 °C for both 24-LLZO and 30-LLZO. There is a significant improvement in ionic conductivity when increasing holding time from 1/2h to 2h, and a small decrease in ionic conductivity when increasing the holding time further to 6h. Increasing sintering time from $t_H = 1/2$h to $t_H = 2$h reduces both the bulk and grain boundary resistivity in 24-LLZO. The reduction in bulk ionic resistivity is likely a result of a higher fraction of cubic phase LLZO. Although it is not observable in the diffractogram (Fig. 4.13a), there might be some remaining tetragonal phase LLZO after sintering for 1/2h. Small fractions of tetragonal phase LLZO are not observable in XRD, because the low intensity diffraction peaks from tetragonal LLZO phase would be indistinguishable from the high intensity peaks from the cubic LLZO phase. The lower grain boundary resistivity is due to a significant reduction in the density of grain boundaries caused by AGG (the quantitative reduction in the number of grain boundaries is visible by comparing Figs. C.5a and C.5c). The complete absence of grain boundary resistivity in 24-LLZO sintered for 6h is as expected from the microstructure: due to the AGG there are no grain boundaries remaining, as shown in Fig. 4.14b.

The highest ionic conductivity of $2.99 \cdot 10^{-4}$ Scm^{-1} was measured in 24-LLZO sintered with SP-C @ 2h. This is a high ionic conductivity, comparable to the best achieved by ambient air sintering of Al-LLZO in literature (see Table 2.2). To

further increase the ionic conductivity, the RD should be increased as discussed in Section 5.3. The high ionic conductivity obtained in this work is partly due to the AGG, which removes grain boundary resistance. However, AGG is not the ideal method of increasing the ionic conductivity, because it lowers mechanical strength. Small and tightly bound grains and high density is the preferred microstructure, as it offers good ionic conductivity and high mechanical strength.

Regarding the reproducibility of these results, it is difficult to tell from the few experiments conducted in this work. Ideally, more parallels should be employed, but due to limited time and resources only the experiment with the best performing sintering program was repeated. SP-C @ 2h was applied twice with different samples to test the reproducibility (see Table 4.2). The two 30-LLZO samples showed similar ionic conductivity, while the two 24-LLZO samples showed a somewhat higher variance. Based on the limited amount of data available, quantitatively estimating the sample variance is unreliable. However, the similar trend between 24-LLZO and 30-LLZO samples, and relatively small variance between the SP-C @ 2h samples, indicate an acceptable reproducibility.

5.5 Optimal Li excess

As a final remark, the Li excess values used in this work are likely higher than optimal. From the ionic conductivity results it is obvious that 30 mol% Li excess it too much, but there are multiple indications that 24 mol% might also be too much. First, there is little correlation between sintering holding time and RD. Hence, densification is not a reason to apply longer sintering holding times. Second, higher t_H has two obvious effects: (i) the large grains grow larger and eventually forms a void, and (ii) the cubic LLZO phase is stabilised as the Li-loss increases. Considering (i) that the growth of large grains is undesirable, and (ii) that prolonged holding times at high temperature is only necessary in order to evaporate the Li that was added in the first place, applying lower Li excess seems reasonable. Lower Li excess should reduce AGG and allow for shorter sintering duration. Of course, the Li excess should not be too low, because that would cause pyrochlore formation. Based

on these insights, the optimal Li excess for producing Al-LLZO by spray pyrolysis is between 8 mol% and 24 mol%.

6 Conclusion

This work studied the effect of Li excess and sintering conditions on Al-LLZO powder produced by spray pyrolysis. The goal was to obtain a material which exhibits high density, high phase purity, and high ionic conductivity. Based on the findings in this work, it can be concluded that:

- High ionic conductivity of $\sim 3.0 \cdot 10^{-4}\ Scm^{-1}$ is obtainable by ambient air sintering of 24-LLZO produced by spray pyrolysis.
- Optimal Li excess for spray pyrolysis is between 8 mol% and 24 mol%. 30 mol% Li excess is clearly too much judging by the reduced ionic conductivity, and 24 mol% is likely too much because prolonged sintering is necessary to obtain pure cubic phase LLZO. 8 mol% Li excess is not enough, as evidenced by the formation of a pyrochlore secondary phase.
- 24-LLZO and 30-LLZO experience abnormal grain growth during sintering at 1150 °C, even with a short sintering duration of 1/2h. This growth is directional, and is due to the formation of a liquid Li-Al-O phase, which accelerates grain growth by enabling viscous flow.
- Relative density $> 90\%$ was obtained in 24-LLZO and 30-LLZO by ambient air sintering at 1150 °C. Densification occurs quickly, and a short sintering time of 1/2h can be employed.
- Cubic phase LLZO is stabilised at 1150°C even for samples with high Li excess, due to Li-loss. Multiple sintering times result in pure cubic LLZO, and the rate of Li-loss in the garnet phase is slower after the tetragonal-cubic transition is complete.

7 Further Work

Future endeavours should address the AGG observed in 24-LLZO and 30-LLZO samples, and aim to further increase the RD of sintered pellets. A reliable process which produces small grains with tight grain boundaries and high density should be developed. Lowering the Li excess seems to be the key to limit the AGG. With lower Li excess however, incorporating strategies which improve Li retention might be necessary. Increased density can be achieved by applying different sintering programs, including two-step sintering programs and advanced sintering techniques like hot isostatic pressing and SPS. Also, studying the effects of crucible materials is of interest, good alternatives to alumina include MgO and Pt which are inert to LLZO.

To further explore the LLZO system, other dopant elements can be applied. The choice of dopant has implications for both the sintering behaviour and Li^+ transport properties of LLZO. Commonly applied dopant elements include gallium, niobium and tantalum. Tantalum doping is particularly interesting due to frequent reports of high ionic conductivity $\geq 1.0 \cdot 10^{-3}\ Scm^{-1}$ in Ta-doped LLZO.

Bibliography

[1] V. Thangadurai and W. Weppner, "Recent progress in solid oxide and lithium ion conducting electrolytes research," *Ionics*, vol. 12, no. 1, pp. 81–92, May 2006. [Online]. Available: https://doi.org/10.1007/s11581-006-0013-7

[2] M. Kotobuki, H. Munakata, K. Kanamura, Y. Sato, and T. Yoshida, "Compatibility of Li7La3Zr2O12 Solid Electrolyte to All-Solid-State Battery Using Li Metal Anode," *Journal of The Electrochemical Society*, vol. 157, no. 10, p. A1076, Aug. 2010, publisher: IOP Publishing. [Online]. Available: https://iopscience.iop.org/article/10.1149/1.3474232/meta

[3] X. Feng, M. Ouyang, X. Liu, L. Lu, Y. Xia, and X. He, "Thermal runaway mechanism of lithium ion battery for electric vehicles: A review," *Energy Storage Materials*, vol. 10, pp. 246–267, Jan. 2018. [Online]. Available: http://www.sciencedirect.com/science/article/pii/S2405829716303464

[4] W. Xu, J. Wang, F. Ding, X. Chen, E. Nasybulin, Y. Zhang, and J.-G. Zhang, "Lithium metal anodes for rechargeable batteries," *Energy & Environmental Science*, vol. 7, no. 2, pp. 513–537, Jan. 2014, publisher: The Royal Society of Chemistry. [Online]. Available: https://pubs.rsc.org/en/content/articlelanding/2014/ee/c3ee40795k

[5] E. C. Evarts, "Lithium batteries: To the limits of lithium," *Nature*, vol. 526, no. 7575, pp. S93–S95, Oct. 2015, number: 7575 Publisher: Nature Publishing Group. [Online]. Available: https://www.nature.com/articles/526S93a

[6] M. Motoyama, M. Ejiri, and Y. Iriyama, "Modeling the Nucleation and Growth of Li at Metal Current Collector/LiPON Interfaces," *Journal of The Electrochemical Society*, vol. 162, pp. A7067–A7071, Jan. 2015.

[7] X.-B. Cheng, R. Zhang, C.-Z. Zhao, and Q. Zhang, "Toward Safe Lithium Metal Anode in Rechargeable Batteries: A Review," *Chemical Reviews*, vol. 117, no. 15, pp. 10 403–10 473, Aug. 2017, publisher: American Chemical Society. [Online]. Available: https://doi.org/10.1021/acs.chemrev.7b00115

[8] G. T. Hitz, D. W. McOwen, L. Zhang, Z. Ma, Z. Fu, Y. Wen, Y. Gong, J. Dai, T. R. Hamann, L. Hu, and E. D. Wachsman, "High-rate lithium cycling in a scalable trilayer Li-garnet-electrolyte architecture," *Materials Today*, vol. 22, pp. 50–57, Jan. 2019. [Online]. Available: http://www.sciencedirect.com/science/article/pii/S1369702118301871

[9] J. Leng, Z. Wang, J. Wang, H.-H. Wu, G. Yan, X. Li, H. Guo, Y. Liu, Q. Zhang, and Z. Guo, "Advances in nanostructures fabricated via spray pyrolysis and their applications in energy storage and conversion," *Chemical Society Reviews*, vol. 48, no. 11, pp. 3015–3072, Jun. 2019, publisher: The Royal Society of Chemistry. [Online]. Available: https://pubs.rsc.org/en/content/articlelanding/2019/cs/c8cs00904j

[10] U. Eriksen, "Phase stability of LLZO produced by spray pyrolysis for use in solid-state battery technology," NTNU, Trondheim, Tech. Rep., Dec. 2020.

[11] C. A. Geiger, E. Alekseev, B. Lazic, M. Fisch, T. Armbruster, R. Langner, M. Fechtelkord, N. Kim, T. Pettke, and W. Weppner, "Crystal Chemistry and Stability of "Li7La3Zr2O12" Garnet: A Fast Lithium-Ion Conductor," *Inorganic Chemistry*, vol. 50, no. 3, pp. 1089–1097, Feb. 2011, publisher: American Chemical Society. [Online]. Available: https://doi.org/10.1021/ic101914e

[12] M. Matsui, K. Takahashi, K. Sakamoto, A. Hirano, Y. Takeda, O. Yamamoto, and N. Imanishi, "Phase stability of a garnet-type lithium ion conductor Li7La3Zr2O12," *Dalton Transactions*, vol. 43, no. 3, pp. 1019–1024, Dec. 2013, publisher: The Royal Society of Chemistry. [Online]. Available: https://pubs.rsc.org/en/content/articlelanding/2014/dt/c3dt52024b

[13] N. Bernstein, M. D. Johannes, and K. Hoang, "Origin of the Structural Phase Transition in "Li7La3Zr2O12"," *Physical Review Letters*, vol. 109, no. 20, p. 205702, Nov. 2012, publisher: American Physical Society. [Online]. Available: https://link.aps.org/doi/10.1103/PhysRevLett.109.205702

[14] J. Awaka, N. Kijima, H. Hayakawa, and J. Akimoto, "Synthesis and structure analysis of tetragonal Li7La3Zr2O12 with the garnet-related type structure," *Journal of Solid State Chemistry*, vol. 182, no. 8, pp. 2046–2052, Aug. 2009. [Online]. Available: http://www.sciencedirect.com/science/article/pii/S002245960900228X

[15] Y. Wang and W. Lai, "Phase transition in lithium garnet oxide ionic conductors Li7La3Zr2O12: The role of Ta substitution and H2O/CO2 exposure," *Journal of Power Sources*, vol. 275, pp. 612–620, Feb. 2015. [Online]. Available: http://www.sciencedirect.com/science/article/pii/S0378775314018898

[16] A. Paolella, W. Zhu, G. Bertoni, S. Savoie, Z. Feng, H. Demers, V. Gariepy, G. Girard, E. Rivard, N. Delaporte, A. Guerfi, H. Lorrmann, C. George, and K. Zaghib, "Discovering the Influence of Lithium Loss on Garnet Li7La3Zr2O12 Electrolyte Phase Stability," *ACS Applied Energy Materials*, vol. 3, no. 4, pp. 3415–3424, Apr. 2020, publisher: American Chemical Society. [Online]. Available: https://doi.org/10.1021/acsaem.9b02401

[17] H. Xie, Y. Li, and J. B. Goodenough, "Low-temperature synthesis of Li7La3Zr2O12 with cubic garnet-type structure," *Materials Research Bulletin*, vol. 47, no. 5, pp. 1229–1232, May 2012. [Online]. Available: http://www.sciencedirect.com/science/article/pii/S0025540812000384

[18] Y. Matsuda, K. Sakamoto, M. Matsui, O. Yamamoto, Y. Takeda, and N. Imanishi, "Phase formation of a garnet-type lithium-ion conductor Li7-3xAlxLa3Zr2O12," *Solid State Ionics*, vol. 277, pp. 23–29, Sep. 2015. [Online]. Available: http://www.sciencedirect.com/science/article/pii/S0167273815001587

[19] Y. Chen, E. Rangasamy, C. R. d. Cruz, C. Liang, and K. An, "A study of suppressed formation of low-conductivity phases in doped Li7La3Zr2O12 garnets by in situ neutron diffraction," *Journal of Materials Chemistry A*, vol. 3, no. 45, pp. 22 868–22 876, 2015, publisher: Royal Society of Chemistry. [Online]. Available: https://pubs.rsc.org/en/content/articlelanding/2015/ta/c5ta04902d

[20] R. Murugan, V. Thangadurai, and W. Weppner, "Fast Lithium Ion Conduction in Garnet-Type Li7La3Zr2O12," *Angewandte Chemie International Edition*, vol. 46, no. 41, pp. 7778–7781, 2007, _eprint: https://onlinelibrary.wiley.com/doi/pdf/10.1002/anie.200701144. [Online]. Available: https://onlinelibrary.wiley.com/doi/abs/10.1002/anie.200701144

[21] T. Thompson, J. Wolfenstine, J. L. Allen, M. Johannes, A. Huq, I. N. David, and J. Sakamoto, "Tetragonal vs. cubic phase stability in Al – free Ta doped Li7La3Zr2O12 (LLZO)," *Journal of Materials Chemistry A*, vol. 2, no. 33, pp. 13 431–13 436, Jul. 2014, publisher: The Royal Society of Chemistry. [Online]. Available: https://pubs.rsc.org/en/content/articlelanding/2014/ta/c4ta02099e

[22] C. Shao, H. Liu, Z. Yu, Z. Zheng, N. Sun, and C. Diao, "Structure and ionic conductivity of cubic Li7La3Zr2O12 solid electrolyte prepared by chemical co-precipitation method," *Solid State Ionics*, vol. 287, pp. 13–16, Apr. 2016. [Online]. Available: http://www.sciencedirect.com/science/article/pii/S0167273815301892

[23] S. R. Yeandel, B. J. Chapman, P. R. Slater, and P. Goddard, "Structure and Lithium-Ion Dynamics in Fluoride-Doped Cubic Li7La3Zr2O12 (LLZO) Garnet for Li Solid-State Battery Applications," *The Journal of Physical Chemistry C*, vol. 122, no. 49, pp. 27 811–27 819, Dec. 2018, publisher: American Chemical Society. [Online]. Available: https://doi.org/10.1021/acs.jpcc.8b07704

[24] S. Kim, M. Hirayama, S. Taminato, and R. Kanno, "Epitaxial growth and lithium ion conductivity of lithium-oxide garnet for an all solid-state battery electrolyte," *Dalton Transactions*, vol. 42, no. 36, pp. 13 112–13 117, Aug. 2013, publisher: The Royal Society of Chemistry. [Online]. Available: https://pubs.rsc.org/en/content/articlelanding/2013/dt/c3dt51795k

[25] M. Kotobuki, K. Kanamura, Y. Sato, and T. Yoshida, "Fabrication of all-solid-state lithium battery with lithium metal anode using Al2O3-added Li7La3Zr2O12 solid electrolyte," *Journal of Power Sources*, vol. 196, no. 18, pp. 7750–7754, Sep. 2011. [Online]. Available: https://www.sciencedirect.com/science/article/pii/S0378775311008871

[26] Q. Liu, Z. Geng, C. Han, Y. Fu, S. Li, Y.-b. He, F. Kang, and B. Li, "Challenges and perspectives of garnet solid electrolytes for all solid-state lithium batteries," *Journal of Power Sources*, vol. 389, pp. 120–134, Jun. 2018. [Online]. Available: http://www.sciencedirect.com/science/article/pii/S0378775318303628

[27] E. Rangasamy, J. Wolfenstine, and J. Sakamoto, "The role of Al and Li concentration on the formation of cubic garnet solid electrolyte of nominal composition Li7La3Zr2O12," *Solid State Ionics*, vol. 206, pp. 28–32, Jan. 2012. [Online]. Available: http://www.sciencedirect.com/science/article/pii/S0167273811005297

[28] G. P. Wyers and E. H. P. Cordfunke, "Phase relations in the system Li2O-ZrO2," *Journal of Nuclear Materials*, vol. 168, no. 1, pp. 24–30, Oct. 1989. [Online]. Available: https://www.sciencedirect.com/science/article/pii/0022311589905606

[29] A. G. Blackman, L. R. Gahan, and G. H. Aylward, *Aylward and Findlays's SI Chemical Data/Allan Blackman; Lawrence Gahan*, 7th ed. Milton: John Wiley & Sons Australia, Ltd., 2014.

[30] N. S. Kulkarni, T. M. Besmann, and K. E. Spear, "Thermodynamic Optimization of Lithia–Alumina," *Journal of the American Ceramic Society*, vol. 91, no. 12, pp. 4074–4083, 2008, _eprint: https://ceramics.onlinelibrary.wiley.com/doi/pdf/10.1111/j.1551-2916.2008.02753.x. [Online]. Available: https://ceramics.onlinelibrary.wiley.com/doi/abs/10.1111/j.1551-2916.2008.02753.x

[31] X. Huang, Y. Lu, Z. Song, K. Rui, Q. Wang, T. Xiu, M. E. Badding, and Z. Wen, "Manipulating Li2O atmosphere for sintering dense Li7La3Zr2O12 solid electrolyte," *Energy Storage Materials*, vol. 22, pp. 207–217, Nov. 2019. [Online]. Available: http://www.sciencedirect.com/science/article/pii/S2405829718313552

[32] X. Huang, Y. Lu, H. Guo, Z. Song, T. Xiu, M. E. Badding, and Z. Wen, "None-Mother-Powder Method to Prepare Dense Li-Garnet Solid Electrolytes with High Critical Current Density," *ACS Applied Energy Materials*, vol. 1, no. 10, pp. 5355–5365, Oct. 2018, publisher: American Chemical Society. [Online]. Available: https://doi.org/10.1021/acsaem.8b00976

[33] W. Xia, B. Xu, H. Duan, Y. Guo, H. Kang, H. Li, and H. Liu, "Ionic Conductivity and Air Stability of Al-Doped Li7La3Zr2O12 Sintered in Alumina and Pt Crucibles," *ACS Applied Materials & Interfaces*, vol. 8, no. 8, pp. 5335–5342, Mar. 2016, publisher: American Chemical Society. [Online]. Available: https://doi.org/10.1021/acsami.5b12186

[34] Y. Chen, E. Rangasamy, C. Liang, and K. An, "Origin of High Li+ Conduction in Doped Li7La3Zr2O12 Garnets," *Chemistry of Materials*, vol. 27, no. 16, pp. 5491–5494, Aug. 2015, publisher: American Chemical Society. [Online]. Available: https://doi.org/10.1021/acs.chemmater.5b02521

[35] N. Janani, C. Deviannapoorani, L. Dhivya, and R. Murugan, "Influence of sintering additives on densification and Li+ conductivity of Al doped Li7La3Zr2O12 lithium garnet," *RSC Advances*, vol. 4, no. 93, pp. 51 228–51 238, Oct. 2014, publisher: The Royal Society of Chemistry. [Online]. Available: https://pubs.rsc.org/en/content/articlelanding/2014/ra/c4ra08674k

[36] L. Yang, Q. Dai, L. Liu, D. Shao, K. Luo, S. Jamil, H. Liu, Z. Luo, B. Chang, and X. Wang, "Rapid sintering method for highly conductive Li7La3Zr2O12 ceramic electrolyte," *Ceramics International*, vol. 46, no. 8, Part A, pp. 10 917–10 924, Jun. 2020. [Online]. Available: https://www.sciencedirect.com/science/article/pii/S0272884220301073

[37] X. Huang, T. Xiu, M. E. Badding, and Z. Wen, "Two-step sintering strategy to prepare dense Li-Garnet electrolyte ceramics with high Li+ conductivity," *Ceramics International*, vol. 44, no. 5, pp. 5660–5667, Apr. 2018. [Online]. Available: https://www.sciencedirect.com/science/article/pii/S0272884217329255

[38] J. L. Allen, J. Wolfenstine, E. Rangasamy, and J. Sakamoto, "Effect of substitution (Ta, Al, Ga) on the conductivity of Li7La3Zr2O12," *Journal of Power Sources*, vol. 206, pp. 315–319, May 2012. [Online]. Available: http://www.sciencedirect.com/science/article/pii/S0378775312002753

[39] C. Chen, Y. Sun, L. He, M. Kotobuki, E. Hanc, Y. Chen, K. Zeng, and L. Lu, "Microstructural and Electrochemical Properties of Al- and Ga-Doped Li7La3Zr2O12 Garnet Solid Electrolytes," *ACS Applied Energy Materials*, vol. 3, no. 5, pp. 4708–4719, May 2020, publisher: American Chemical Society. [Online]. Available: https://doi.org/10.1021/acsaem.0c00347

[40] Y. Jin and P. J. McGinn, "Al-doped Li7La3Zr2O12 synthesized by a polymerized complex method," *Journal of Power Sources*, vol. 196, no. 20, pp. 8683–8687, Oct. 2011. [Online]. Available: http://www.sciencedirect.com/science/article/pii/S0378775311010913

[41] Z. Hu, H. Liu, H. Ruan, R. Hu, Y. Su, and L. Zhang, "High Li-ion conductivity of Al-doped Li7La3Zr2O12 synthesized by solid-state reaction," *Ceramics International*, vol. 42, no. 10, pp. 12 156–12 160, Aug. 2016. [Online]. Available: https://www.sciencedirect.com/science/article/pii/S0272884216305569

[42] Y. Tian, Y. Zhou, Y. Liu, C. Zhao, W. Wang, and Y. Zhou, "Formation mechanism of sol-gel synthesized Li7-3xAlxLa3Zr2O12 and the influence of abnormal grain growth on ionic conductivity," *Solid State Ionics*, vol. 354, p. 115407, Oct. 2020. [Online]. Available: https://www.sciencedirect.com/science/article/pii/S0167273820304616

[43] Y. Kim, H. Jo, J. L. Allen, H. Choe, J. Wolfenstine, and J. Sakamoto, "The Effect of Relative Density on the Mechanical Properties of Hot-Pressed Cubic Li7La3Zr2O12," *Journal of the American Ceramic Society*, vol. 99, no. 4, pp. 1367–1374, 2016, _eprint: https://ceramics.onlinelibrary.wiley.com/doi/pdf/10.1111/jace.14084. [Online]. Available: https://ceramics.onlinelibrary.wiley.com/doi/abs/10.1111/jace.14084

[44] Y. Zhang, F. Chen, R. Tu, Q. Shen, and L. Zhang, "Field assisted sintering of dense Al-substituted cubic phase Li7La3Zr2O12 solid electrolytes," *Journal of Power Sources*, vol. 268, pp. 960–964, Dec. 2014. [Online]. Available: https://www.sciencedirect.com/science/article/pii/S0378775314005473

[45] S. I. A. Halim, C. H. Chan, and J. Apotheker, "Basics of teaching electrochemical impedance spectroscopy of electrolytes for ion-rechargeable batteries – part 1: a good practice on estimation of bulk resistance of solid polymer electrolytes," *Chemistry Teacher International*, Mar. 2021, publisher: De Gruyter Section: Chemistry Teacher International. [Online]. Available: https://www.degruyter.com/document/doi/10.1515/cti-2020-0011/html

[46] F. Shen, M. B. Dixit, X. Xiao, and K. B. Hatzell, "Effect of Pore Connectivity on Li Dendrite Propagation within LLZO Electrolytes Observed with Synchrotron X-ray Tomography," *ACS Energy Letters*, vol. 3, no. 4, pp. 1056–1061, Apr. 2018, publisher: American Chemical Society. [Online]. Available: https://doi.org/10.1021/acsenergylett.8b00249

[47] J. Su, X. Huang, Z. Song, T. Xiu, M. E. Badding, J. Jin, and Z. Wen, "Overcoming the abnormal grain growth in Ga-doped Li7La3Zr2O12 to enhance the electrochemical stability against Li metal," *Ceramics International*, vol. 45, no. 12, pp. 14 991–14 996, Aug. 2019. [Online]. Available: https://www.sciencedirect.com/science/article/pii/S0272884219310739

[48] X. Zeng, A. J. Martinolich, K. A. See, and K. T. Faber, "Dense garnet-type electrolyte with coarse grains for improved air stability and ionic conductivity," *Journal of Energy Storage*, vol. 27, p. 101128, Feb. 2020. [Online]. Available: https://www.sciencedirect.com/science/article/pii/S2352152X19306528

[49] X. Huang, Y. Lu, Z. Song, T. Xiu, M. E. Badding, and Z. Wen, "Preparation of dense Ta-LLZO/MgO composite Li-ion solid electrolyte: Sintering, microstructure, performance and the role of MgO," *Journal of Energy Chemistry*, vol. 39, pp. 8–16, Dec. 2019. [Online]. Available: https://www.sciencedirect.com/science/article/pii/S2095495618309161

[50] X. Huang, Z. Song, T. Xiu, M. E. Badding, and Z. Wen, "Sintering, micro-structure and Li+ conductivity of Li7-xLa3Zr2-xNbxO12/MgO (x = 0.2-0.7) Li-Garnet composite ceramics," *Ceramics International*, vol. 45, no. 1, pp. 56–63, Jan. 2019. [Online]. Available: https://www.sciencedirect.com/science/article/pii/S027288421832604X

[51] "Dense shaped refractory products —Determination of bulk density, apparentporosity and true porosity," International Organization for Standardization, International Standard ISO 5017:1998, Jul. 1998.

[52] S. Gates-Rector and T. Blanton, "The Powder Diffraction File: a quality materials characterization database," *Powder Diffraction*, vol. 34, no. 4, pp. 352–360, Dec. 2019, publisher: Cambridge University Press. [Online]. Available: https://www.cambridge.org/core/journals/powder-diffraction/article/powder-diffraction-file-a-quality-materials-characterization-database/3C1FDF449C7A82A8E6FBC8F76342187A

Appendices

A Pellet mass & density

The mass of pellets before and after sintering, and the weight measurements performed during Archimedes' method are listed in Table A.1. The submerged and wet weights were measured in isopropanol, in order to calculate density and porosity.

Table A.1: The weight measurements of pellets before sintering, and after sintering during Archimedes' method. m_0=Pre-sintered mass, m_{dry}=Dry mass after sintering, m_{sub}=Weight while submerged in isopropanol, m_{wet}=Weight with isopropanol in open pores, T=Isopropanol temperature.

Sample		$m_0\,[mg]$	$m_{dry}\,[mg]$	$m_{sub}\,[mg]$	$m_{wet}\,[mg]$	$T\,[°C]$
8-LLZO	SP-B @ 1h	339.0	288.5	242.6	295.6	21.5
24-LLZO	SP-A @ 1/2h	343.0	280.2	235.2	289.3	20.2
	SP-A @ 1h	337.5	277.6	233.3	289.3	20.6
	SP-A @ 2h	342.6	276.8	228.0	282.8	20.6
	SP-A @ 6h	346.9	274.9	231.5	289.2	21.0
	SP-B @ 1/2h	344.7	276.4	230.6	278.4	11.2
	SP-B @ 1h	296.8	233.2	195.2	233.9	11.8
	SP-B @ 2h	342.5	267.4	223.9	268.6	12.6
	SP-B @ 6h	292.8	227.5	190.5	228.0	13.2
	SP-C @ 1/2h	311.2	248.0	205.3	248.6	9.5
	SP-C @ 2h	328.2	258.9	215.6	259.7	10.5
	SP-C @ 2h	341.6	270.9	225.4	271.8	22.0
	SP-C @ 2h	343.8	272.3	225.8	273.1	22.5

(To be continued)

Sample		$m_0\,[mg]$	$m_{dry}\,[mg]$	$m_{sub}\,[mg]$	$m_{wet}\,[mg]$	$T\,[°C]$
	SP-C @ 6h	339.8	85.5[a]	71.4[a]	85.8[a]	22.0
	SP-D @ 1/2h	345.3	275.9	228.7	276.1	10.0
	SP-D @ 1/2h[b]	330.3	264.6	-	-	-
30-LLZO	SP-A @ 1/2h	349.0	275.9	222.0	277.5	11.6
	SP-A @ 1h	349.2	277.1	232.1	289.9	12.0
	SP-A @ 2h	355.6	281.6	235.9	293.3	12.6
	SP-A @ 6h	352.2	278.0	230.1	286.3	13.2
	SP-B @ 1/2h	351.5	274.7	228.4	275.5	12.2
	SP-B @ 1h	349.2	267.2	22.5	268.6	12.4
	SP-B @ 2h	347.9	261.8	219.1	264.1	13.0
	SP-B @ 6h	349.6	263.4	220.3	265.6	13.4
	SP-C @ 1/2h	333.9	263.3	219.1	264.0	10.0
	SP-C @ 2h	339.5	261.0	218.1	262.5	11.0
	SP-C @ 2h	347.7	270.4	225.0	271.4	22.0
	SP-C @ 2h	337.2	263.2	220.1	263.8	22.5
	SP-C @ 6h	338.7	72.3[a]	60.7[a]	72.8[a]	22.0
	SP-D @ 1/2h	347.0	273.1	228.3	273.9	11.0
	SP-D @ 1/2h[b]	343.8	271.6	-	-	-

[a] The low mass is due to rigorous polishing before measurement.

[b] Archimedes' method was not performed on this sample.

The RD of pellets sintered with SP-C and SP-D are shown in Fig. A.1.

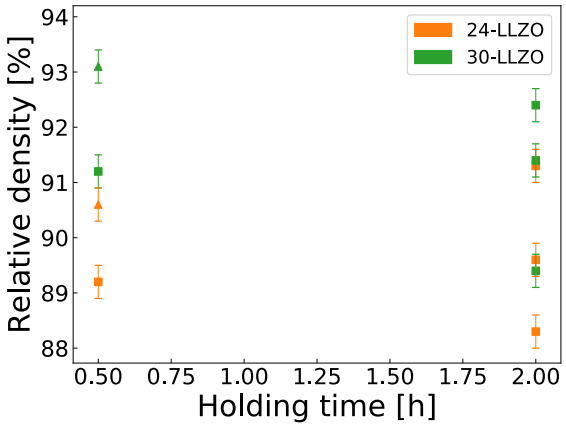

Figure A.1. The RD of pellets sintered with SP-C (T_H = 1150 °C, BP-ratio = 1/3, denoted ■) and SP-D (T_H = 1150 °C, BP-ratio = 0, denoted ▲) as a function of sintering holding time. The densities were measured by Archimedes' method.

The RD was calculated using a theoretical density, ρ_t, of 5.095 gcm^{-3}. This was determined by estimating the unit cell volume by Rietveld refinement of a XRD pattern of pure cubic LLZO. The calculation is shown in eq. A.1, where M_i is the molar mass of specie i, a is the lattice constant, and N_A is Avogadro's number.

$$\rho_{theoretical} = \frac{8M_{LLZO}}{N_A a^3} = 8\frac{6.25M_{Li} + 0.25M_{Al} + 3M_{La} + 2M_{Zr} + 12M_O}{N_A(12.9927655 \cdot 10^{-8})^3} \tag{A.1}$$

The bulk densities, ρ_b, presented in Fig. 4.3 and Fig. A.1 are calculated from the measurements provided in Table A.1 according to eq. A.2.

$$\rho_b = \frac{m_0}{m_{wet} - m_{sub}} \cdot (-0.0009T + 0.8018) \Rightarrow RD = \frac{rho_b}{rho_t} \tag{A.2}$$

The error in the RD was calculated by applying Gauss' law of error propagation, as described in Section E. Measurement uncertainties of 0.1 mg in all weight measurements and 0.5 °C in the temperature measurements were assumed, which are the instrument uncertainties.

B X-ray diffractograms

The composition of the as-sprayed powder precursors have previously been measured with XRD by Eriksen [10] and is shown in Fig. B.1. The powder precursor contains the stable Li_2CO_3 compound. The calcination temperature of 750 °C was employed for all powders in order for Li_2CO_3 to rapidly decompose.

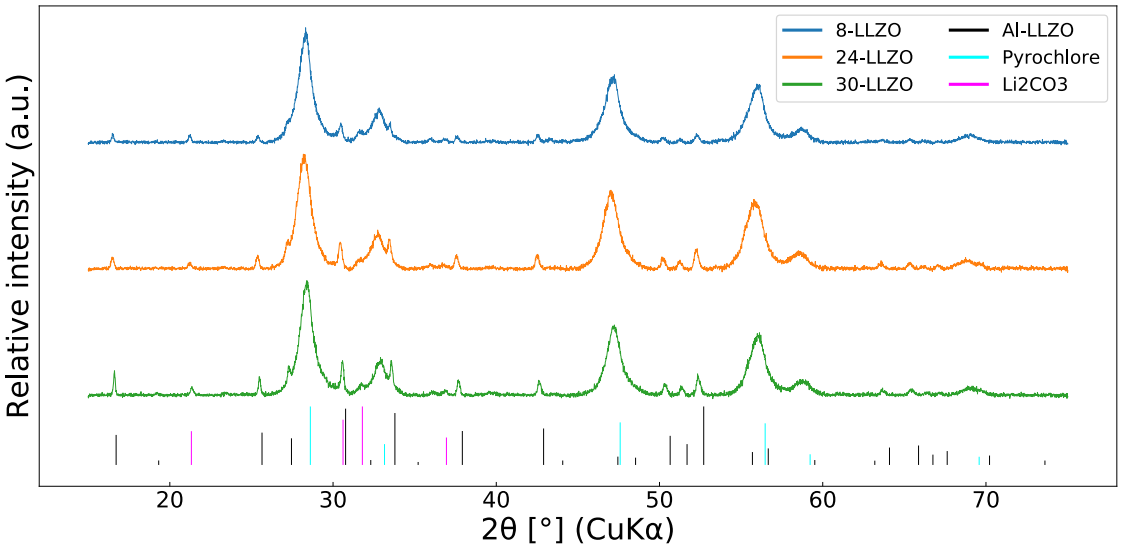

Figure B.1. Diffractogram of the powder precursors (as-sprayed from the spray pyrolysis). All peaks are indexed to cubic LLZO, pyrochlore or Li_2CO_3. Previously measured by Eriksen [10].

The X-ray diffractograms of all samples sintered with SP-A are shown in Fig. B.2. The cubic phase LLZO is not fully stabilised for holding in the range where $t_H \in [1/2\text{h},\ 6\text{h}]$.

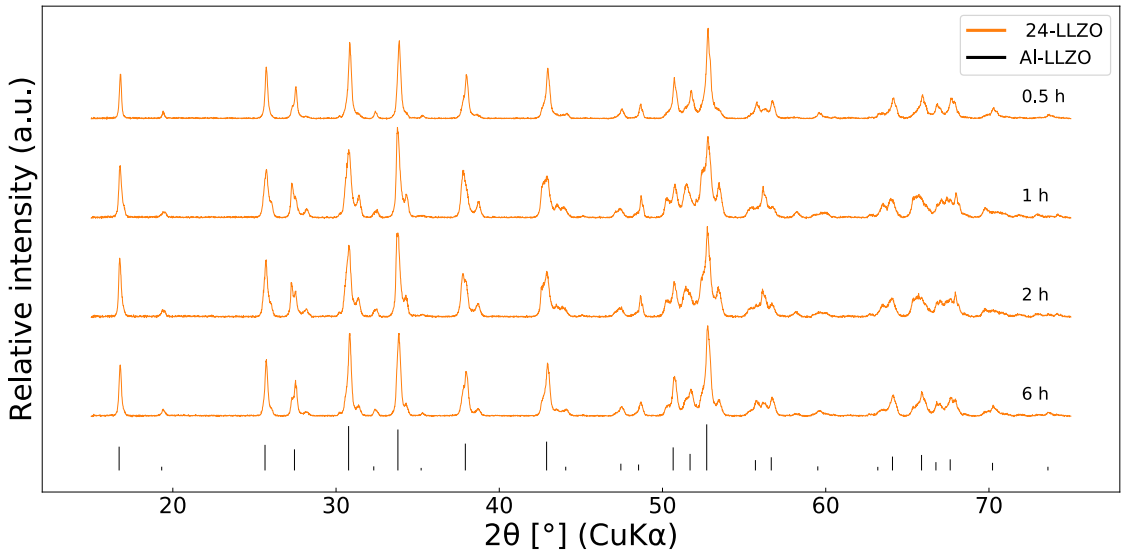

(a) 24-LLZO, SP-A

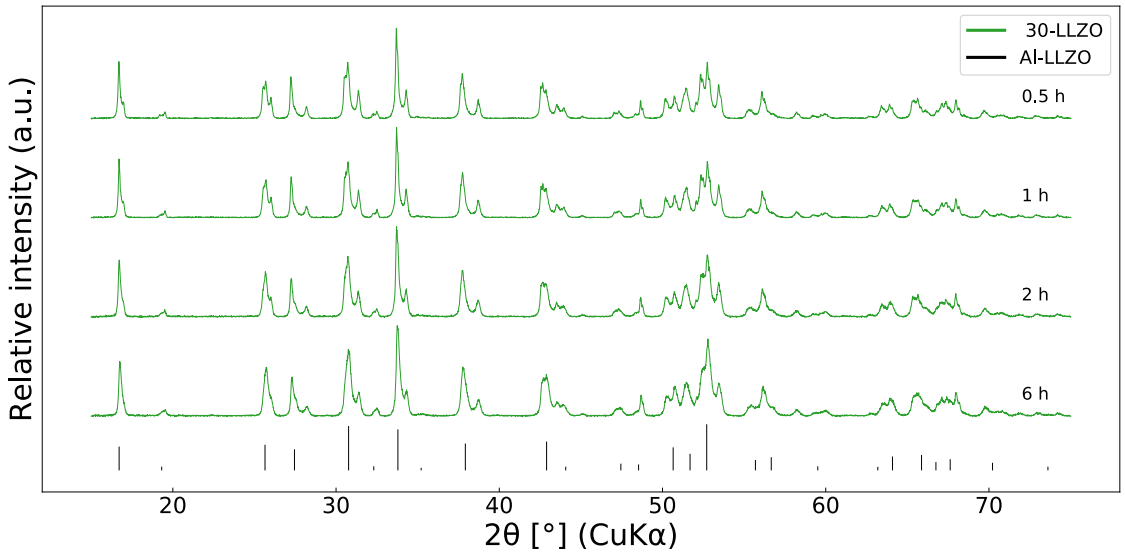

(b) XRD, 30-LLZO, SP-A

Figure B.2. Bulk representative diffraction patterns of samples sintered with SP-A ($T_H = 1000\,°\text{C}$, BP-ratio = 2). Only peaks belonging to tetragonal and cubic LLZO are present.

Fig. B.3 shows the collected diffractogram of the only sintered 8-LLZO sample. Just like the calcined 8-LLZO powder (Fig. 4.1), the sintered 8-LLZO is Li-deficient and has a residual pyrochlore phase.

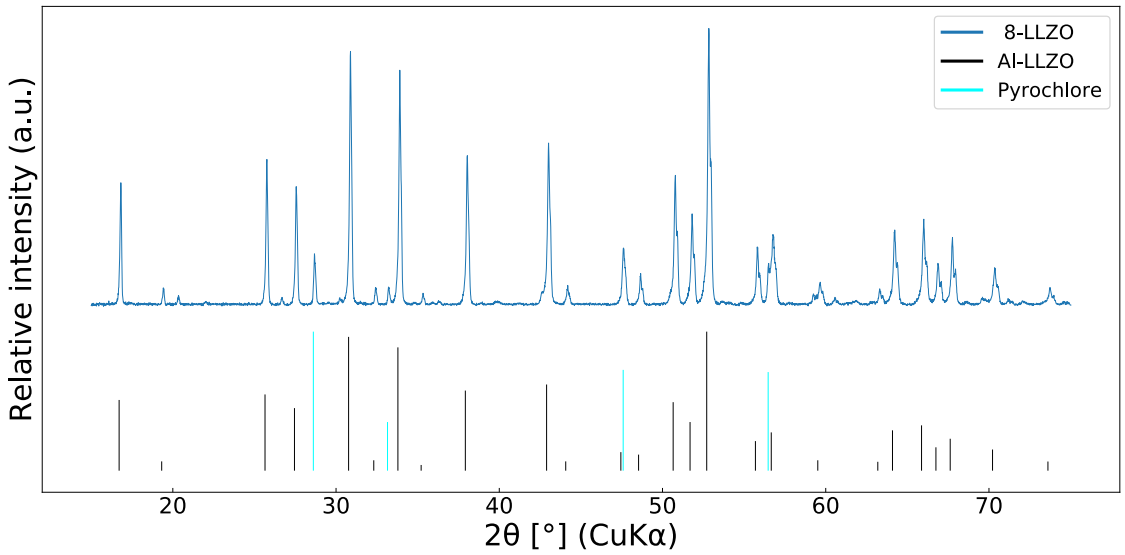

Figure B.3. Bulk representative diffractogram of of the 8-LLZO sample sintered with SP-B ($T_H = 1150\,°C$, BP-ratio = 2) @ 1h. All peaks belong to cubic LLZO or pyrochlore.

Fig. B.4 shows the effect of BP-ratio on the phase composition. In general, higher BP-ratio improves Li retention slightly, as evidenced by the higher tetragonality of samples sintered with high BP-ratios. However, no clear trend is observed in 30-LLZO sintered at 1/2h.

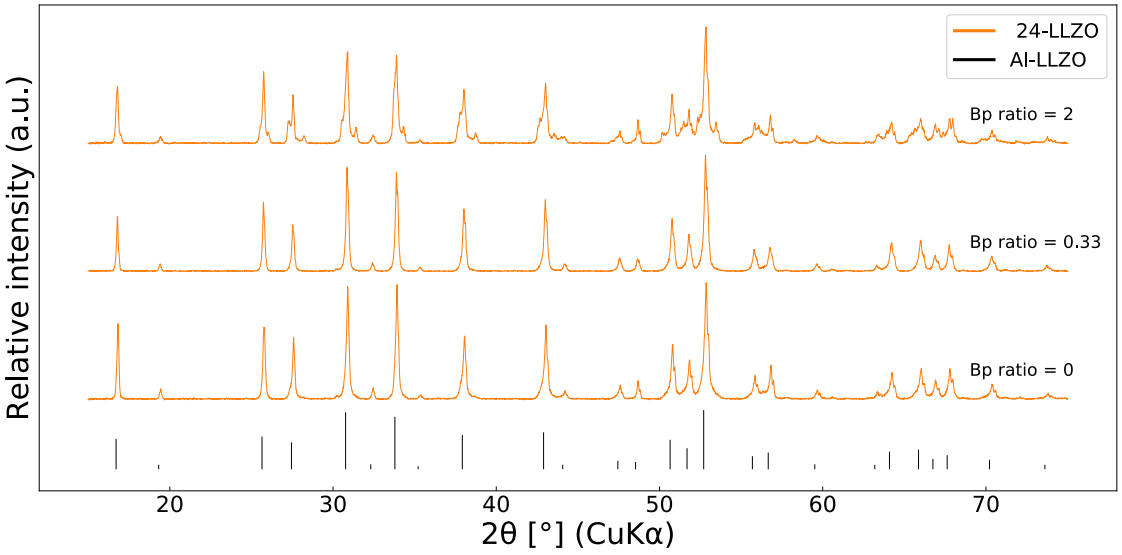

(a) 24-LLZO, $T_H = 1150\,°\mathrm{C}$, $t_H = 1/2\mathrm{h}$

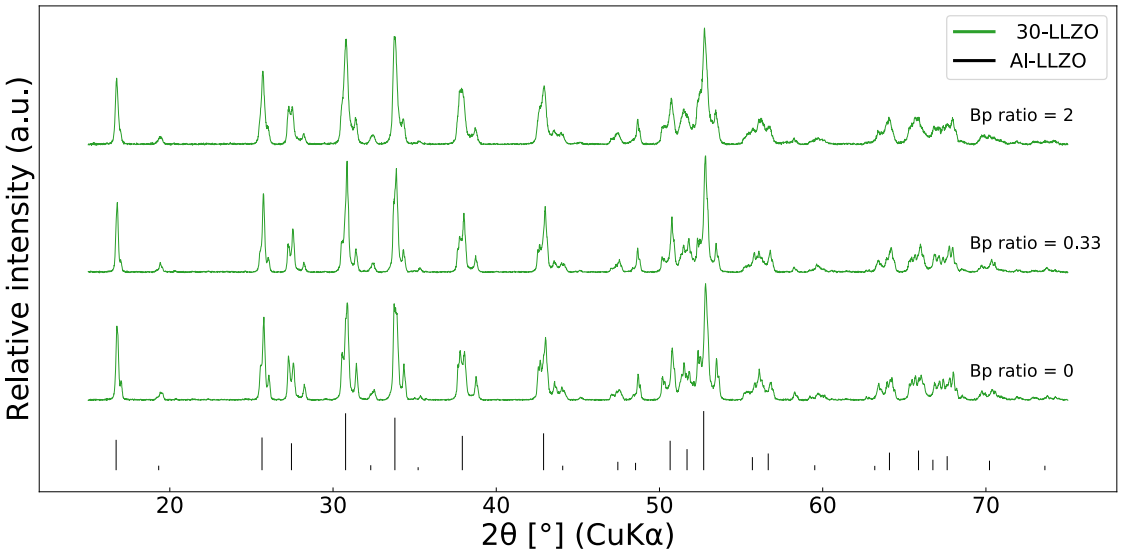

(b) 30-LLZO, $T_H = 1150\,°\mathrm{C}$, $t_H = 1/2\mathrm{h}$

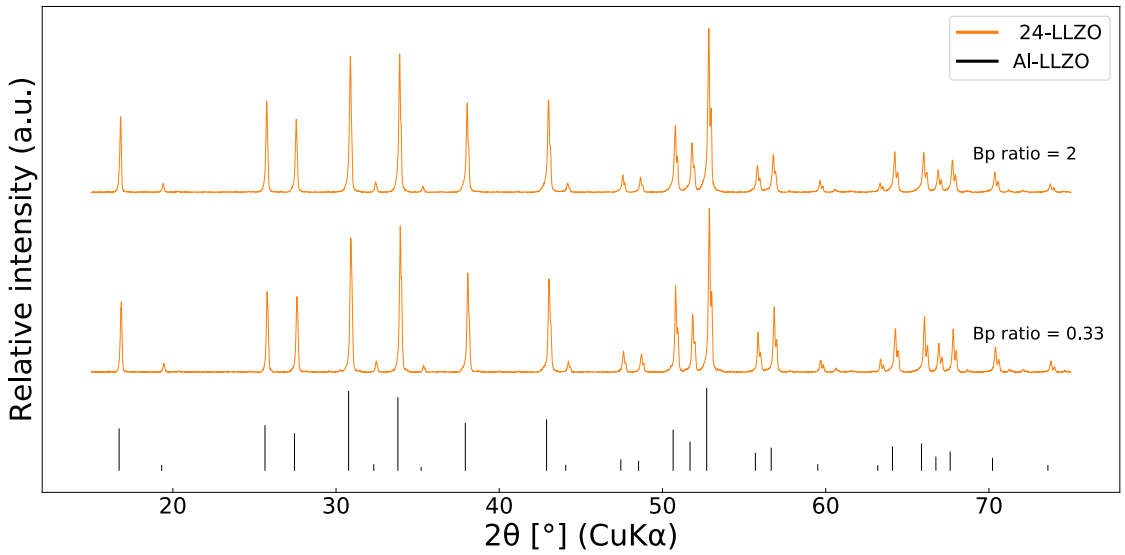

(c) 24-LLZO, $T_H = 1150\,^{\circ}\mathrm{C}$, $t_H = 2\mathrm{h}$

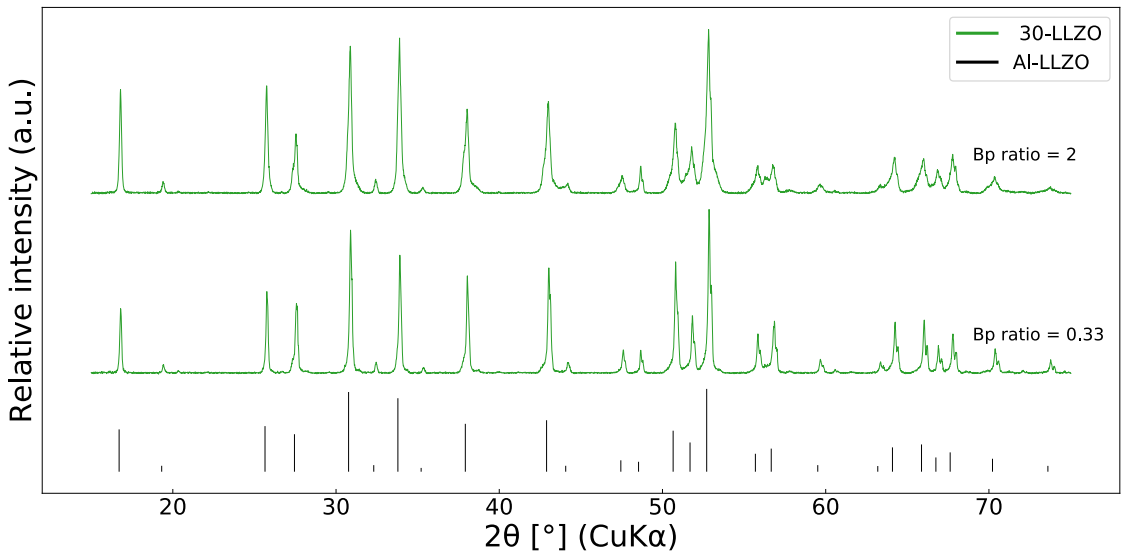

(d) 30-LLZO, $T_H = 1150\,^{\circ}\mathrm{C}$, $t_H = 2\mathrm{h}$

Figure B.4. Bulk representative diffractograms of samples with varying BP-ratio. All peaks are indexed to cubic or tetragonal LLZO.

C SEM micrographs

Micrographs of the pristine surfaces of 24-LLZO pellets sintered with SP-A are shown in Fig. C.1. The pristine fracture surfaces of the pellets sintered with SP-A are shown in Fig. C.2. Micrographs already included in Section 4 are omitted.

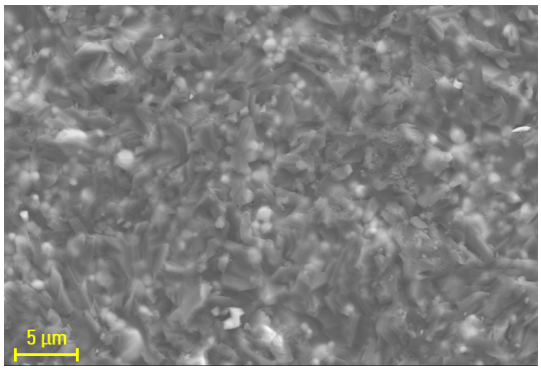

(a) 24-LLZO, SP-A @ 1/2h

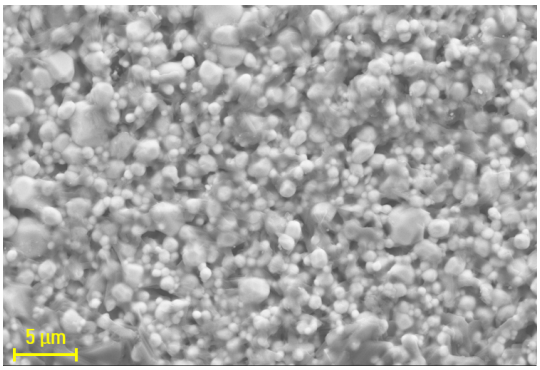

(b) 24-LLZO, SP-A @ 1h

Figure C.1. Secondary electron micrographs of the pristine surface of 24-LLZO pellets sintered with SP-A ($T_H = 1000\,°\mathrm{C}$, BP-ratio = 2).

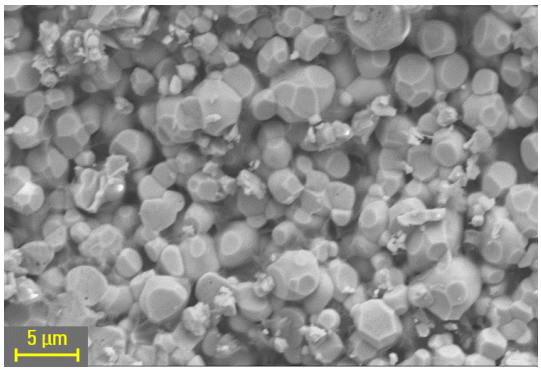

(a) 24-LLZO, SP-A @ 1/2h

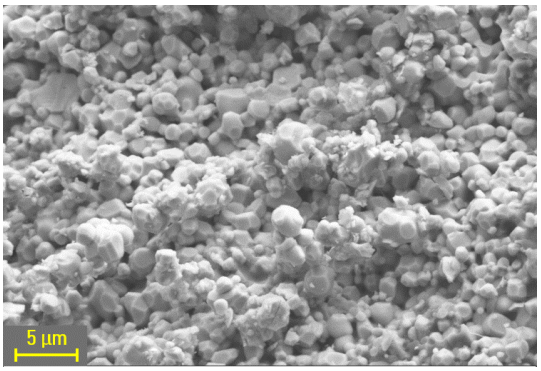

(b) 24-LLZO, SP-A @ 1h

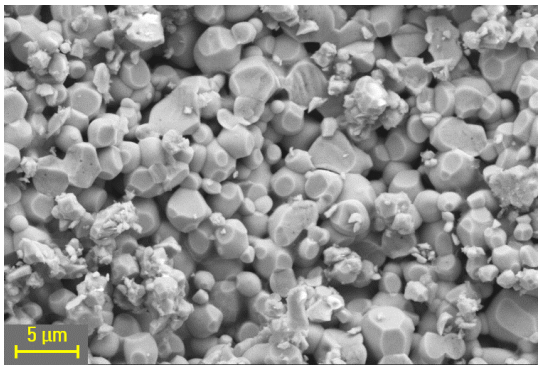

(c) 24-LLZO, SP-A @ 2h

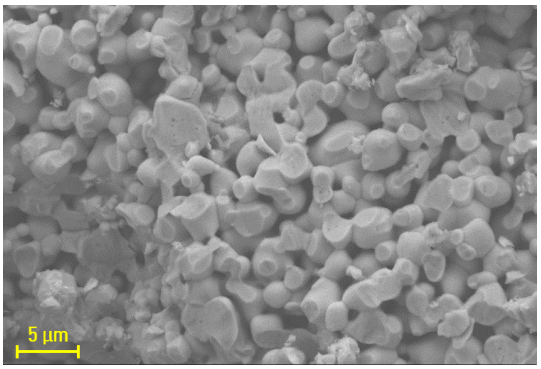

(d) 24-LLZO, SP-A @ 6h

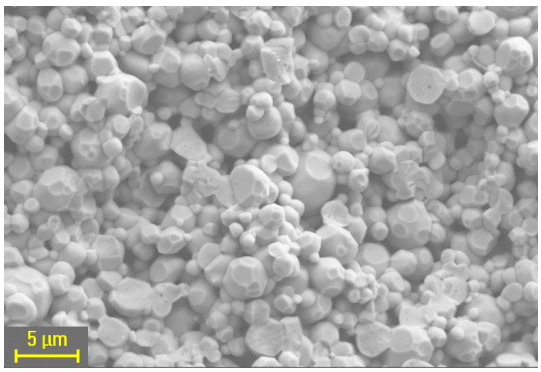

(e) 30-LLZO, SP-A @ 1h

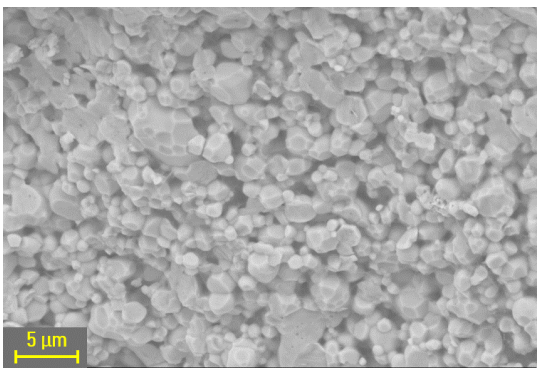

(f) 30-LLZO, SP-A @ 2h

Figure C.2. Secondary electron micrographs of pristine fracture surfaces of 24-LLZO and 30-LLZO pellets sintered with SP-A ($T_H = 1000\,°C$, BP-ratio = 2).

Micrographs of the pristine surfaces of 24-LLZO pellets sintered with SP-B are shown in Fig. C.3.

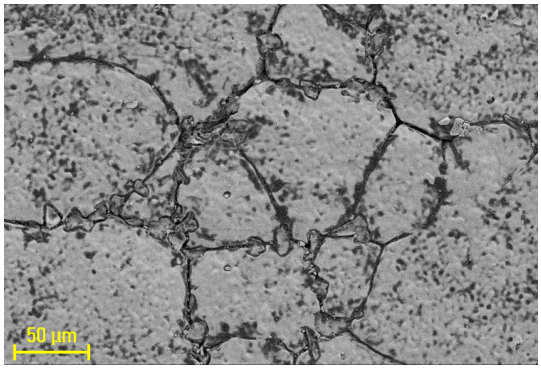

(a) 24-LLZO, SP-B @ 1/2h

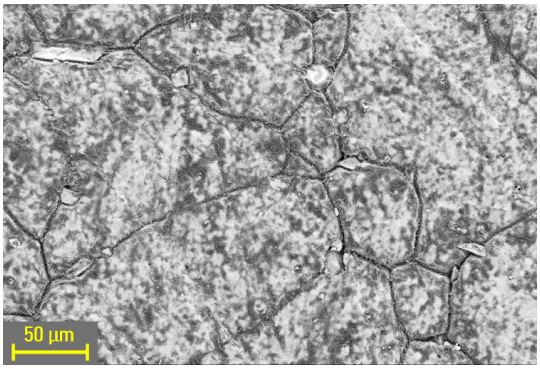

(b) 24-LLZO, SP-B @ 1h

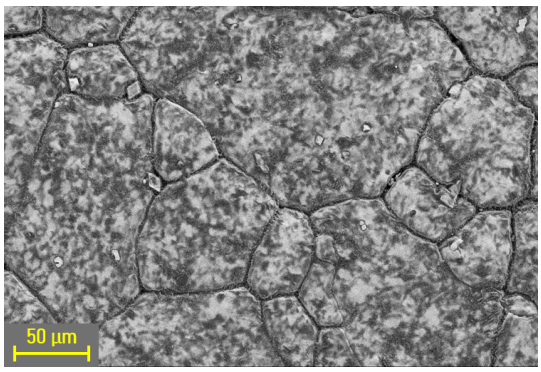

(c) 24-LLZO, SP-B @ 2h

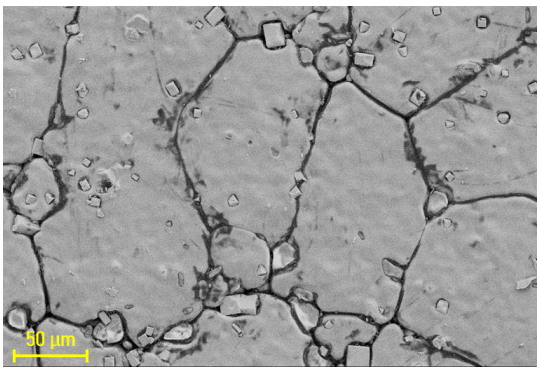

(d) 24-LLZO, SP-B @ 6h

Figure C.3. Secondary electron micrographs of the pristine surface of 24-LLZO pellets sintered with SP-B ($T_H = 1150\,°C$, BP-ratio = 2).

The pristine fracture surface of 24-LLZO pellets sintered with SP-B are shown in Fig. C.4. The sintering behaviour is similar to the 30-LLZO pellets, which is shown in Fig. 4.8.

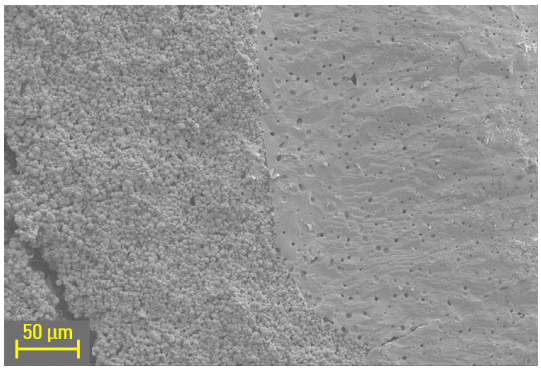

(a) 24-LLZO, SP-B @ 1/2h

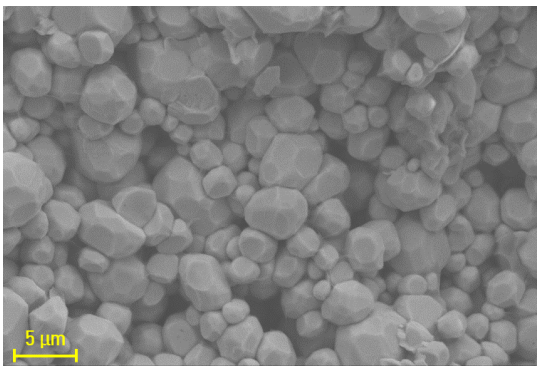

(b) 24-LLZO, SP-B @ 1/2h

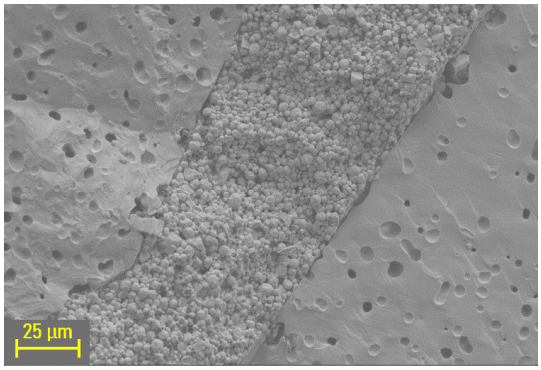

(c) 24-LLZO, SP-B @ 1h

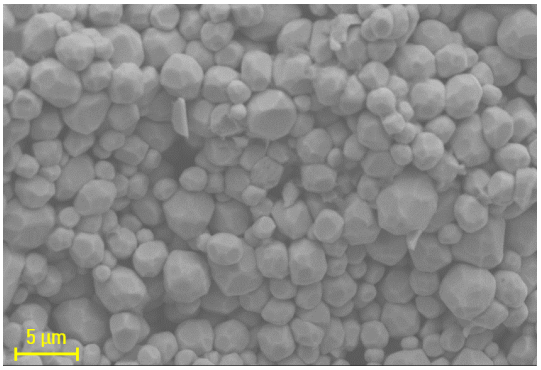

(d) 24-LLZO, SP-B @ 1h

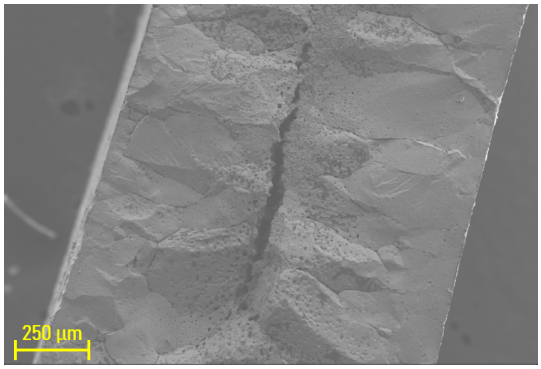

(e) 24-LLZO, SP-B @ 2h

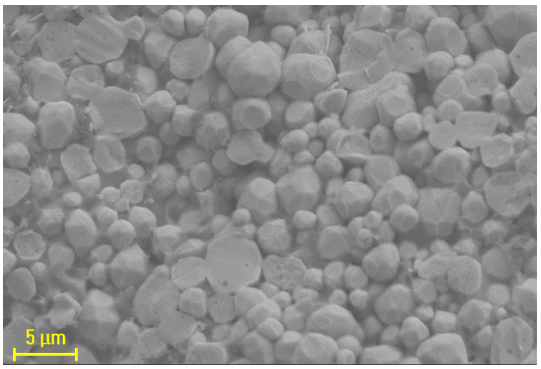

(f) 24-LLZO, SP-B @ 2h

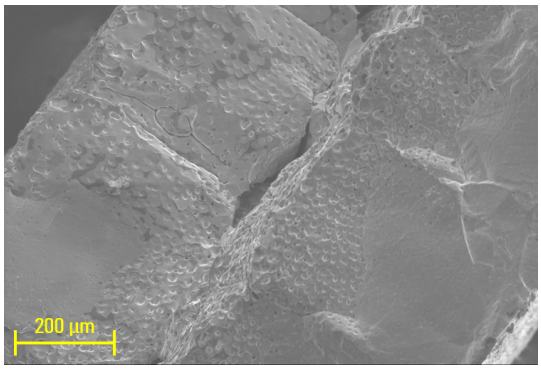

(g) 24-LLZO, SP-B @ 6h

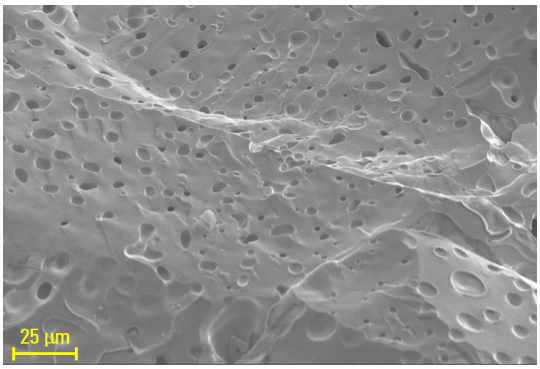

(h) 24-LLZO, SP-B @ 6h

Figure C.4. Secondary electron micrographs of pristine fracture surfaces of 24-LLZO pellets sintered with SP-B ($T_H = 1150\,°C$, BP-ratio = 2).

The pristine fracture surfaces of pellets sintered with SP-C and SP-D are shown in Figs. C.5 and C.6 respectively. BP-ratio has little influence on the microstructure, which is similar to those of pellets sintered with SP-B.

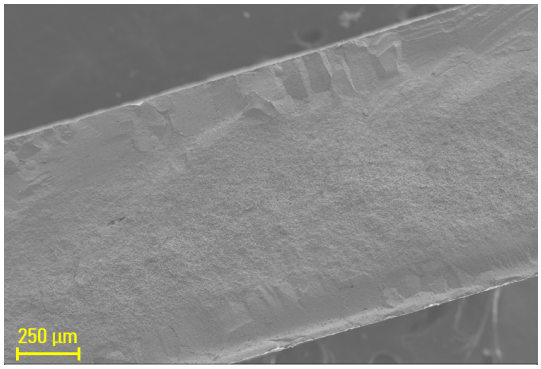

(a) 24-LLZO, SP-C @ 1/2h

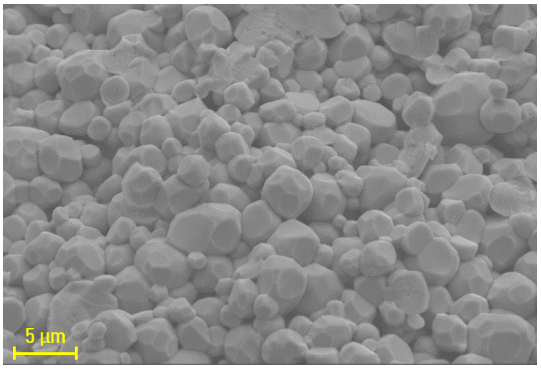

(b) 24-LLZO, SP-C @ 1/2h

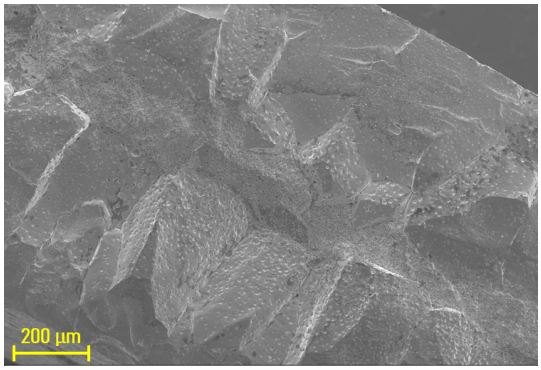

(c) 24-LLZO, SP-C @ 2h

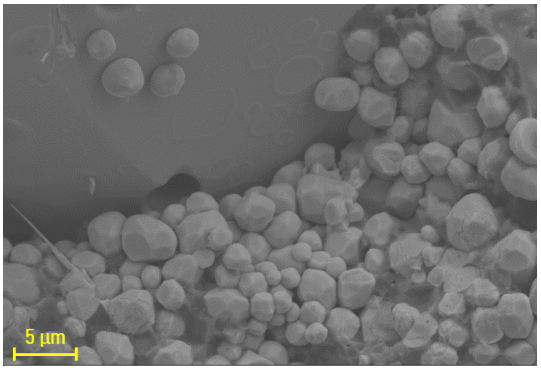

(d) 24-LLZO, SP-C @ 2h

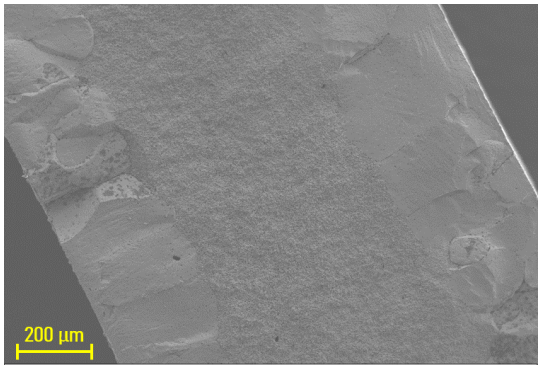

(e) 30-LLZO, SP-C @ 1/2h

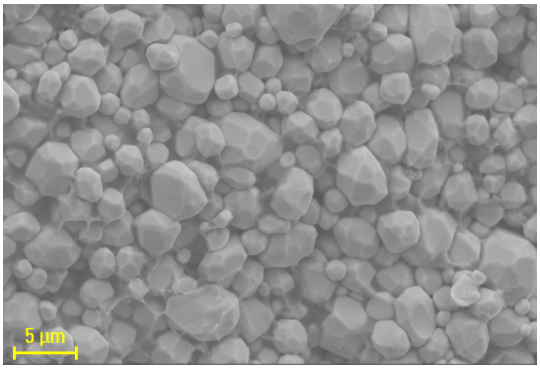

(f) 30-LLZO, SP-C @ 1/2h

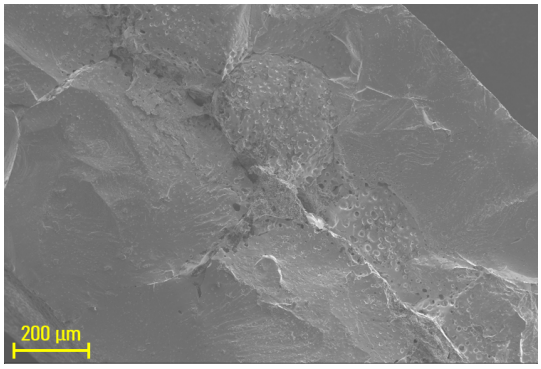

(g) 30-LLZO, SP-C @ 2h

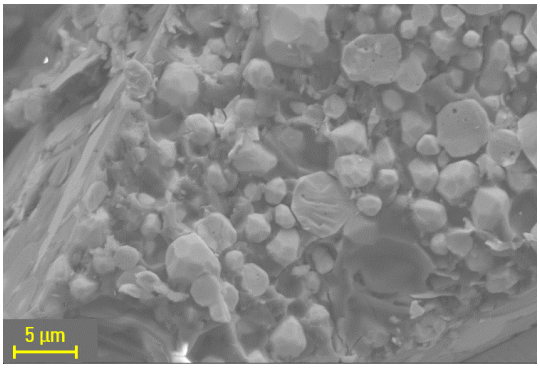

(h) 30-LLZO, SP-C @ 2h

Figure C.5. Secondary electron micrographs of pristine fracture surfaces of 24-LLZO and 30-LLZO pellets sintered with SP-C ($T_H = 1150\,°C$, BP-ratio = 1/3).

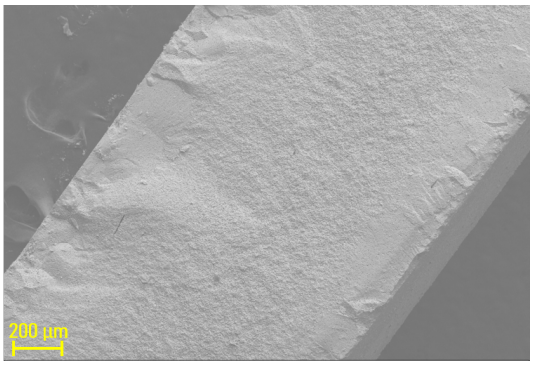

(a) 24-LLZO, SP-D @ 1/2h

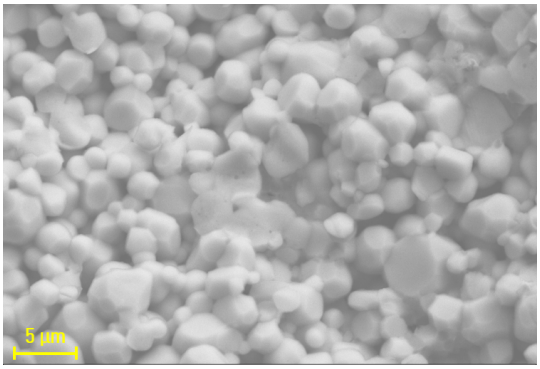

(b) 24-LLZO, SP-D @ 1/2h

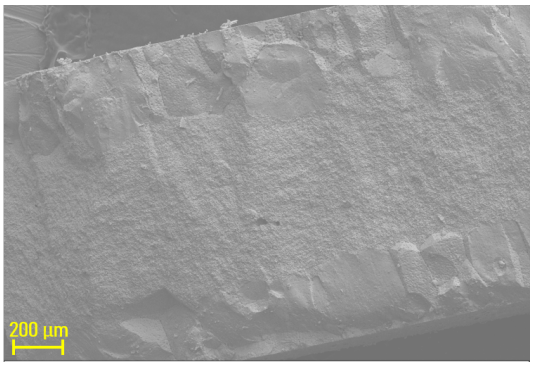

(c) 30-LLZO, SP-D @ 1/2h

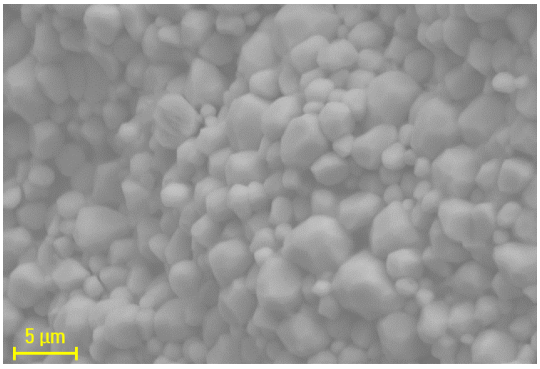

(d) 30-LLZO, SP-D @ 1/2h

Figure C.6. Secondary electron micrographs of pristine fracture surfaces of 24-LLZO and 30-LLZO pellets sintered with SP-D ($T_H = 1150\,°C$, BP-ratio = 0).

Micrographs of the polished fracture surface of 30-LLZO sintered with SP-B @ 2h are shown in Fig. C.7. The pore volume and secondary phases are clearly visible with backscattered electrons on the smooth polished surface.

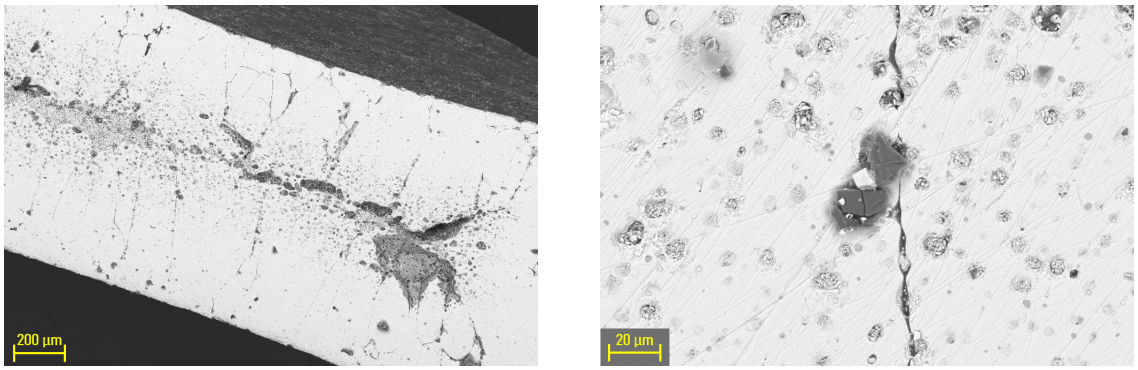

(a) 30-LLZO, SP-B @ 2h **(b)** 30-LLZO, SP-B @ 2h

Figure C.7. Backscatter electron micrographs of the polished fracture surface of 30-LLZO sintered with SP-B ($T_H = 1150\,°C$, BP-ratio = 2) @ 2h.

The EDS map in Fig. C.8 shows the concentration of elements on the surface of a 24-LLZO pellet sintered with SP-C @ 2h. The impurity phases A and B shown in Fig. 4.11b are also present on this pellet surface. The elemental composition of the secondary phases in this EDS map are similar to the results shown in Table 4.1. These secondary phases has a high concentration of Zr, and negligible concentration of La.

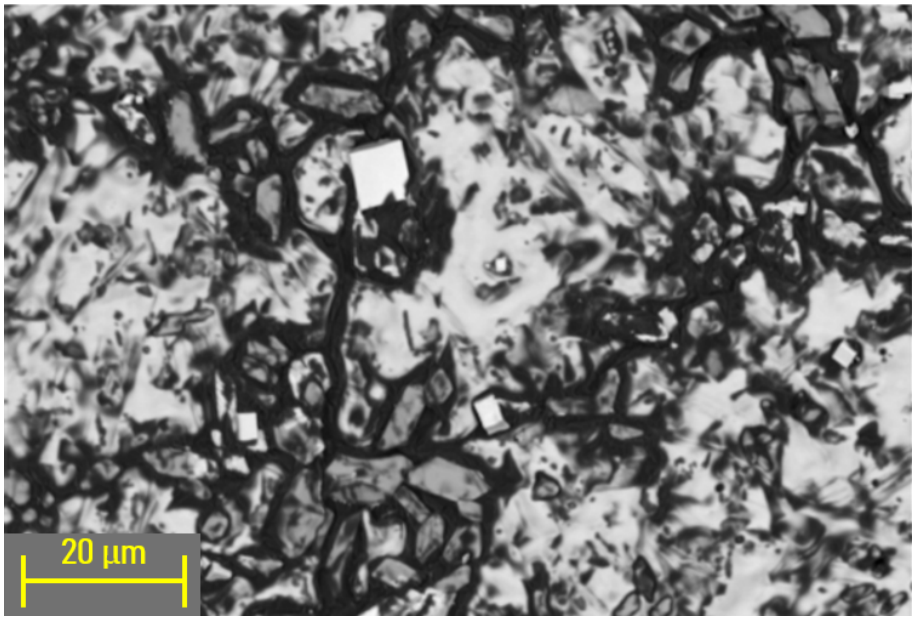

(a) SEM, 24-LLZO, SP-C @ 2h

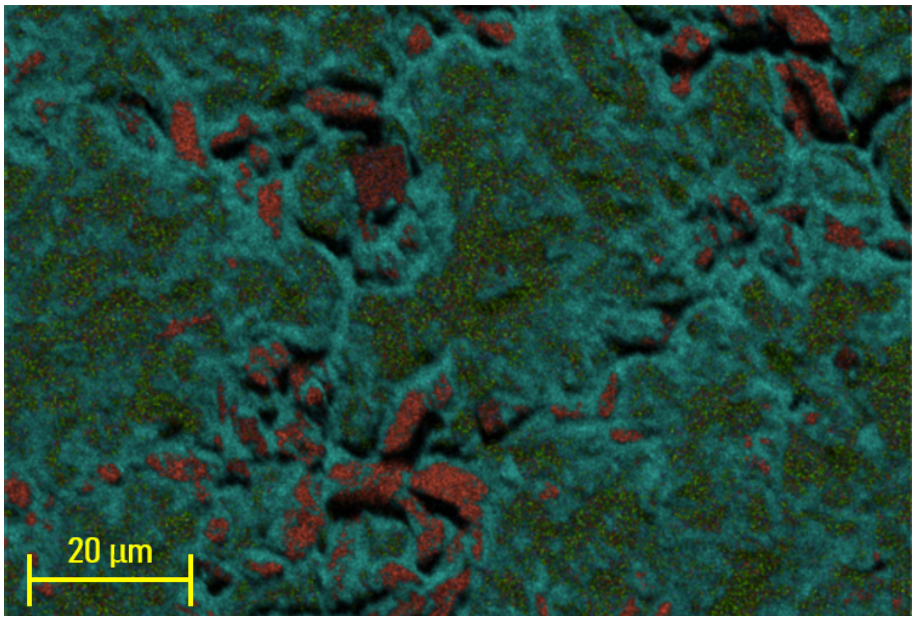

(b) EDS, 24-LLZO, SP-C @ 2h

Figure C.8. Backscatter electron micrograph (a) of the pristine fracture surface of 24-LLZO sintered with SP-C ($T_H = 1150\,°C$, BP-ratio = 1/3) @ 2h. The EDS map (b) shows the concentration of elements in the micrograph, where O is light blue, Al is dark blue, La is green and Zr is red. Li is not observable with EDS.

D Nyquist diagrams

EIS results are presented in the Nyquist diagrams in Fig. D.1. The best model fits are included in the diagrams. The data was fitted with the EC-lab V11.31 (BioLogic) software using one of the two equivalent circuits shown in Fig. 3.6. Eq. D.1 and eq. D.2 show the impedance and total ionic conductivity of the equivalent circuits in Fig. 3.6a and Fig. 3.6b respectively. The total ionic conductivity is calculated from the resistance of the equivalent circuit, and the thickness, t, and cross sectional area, A, of the samples. Table D.1 shows the best fit parameters for all the impedance measurements, as calculated by the EC-Lab.

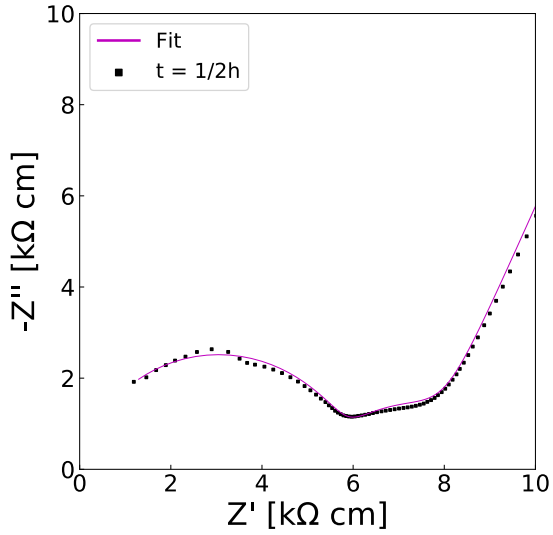

(a) 24-LLZO, $t_H = 1/2h$

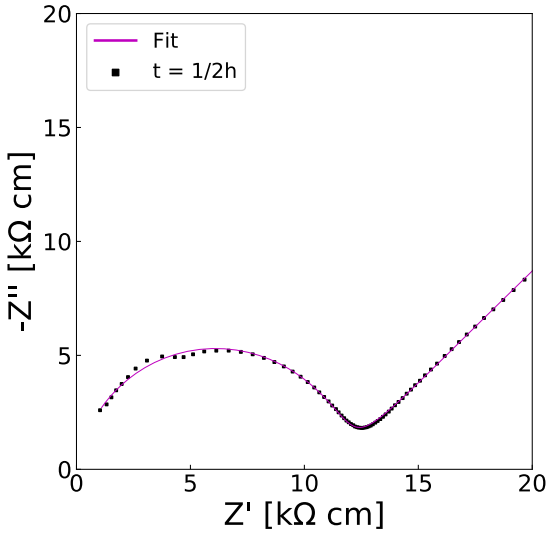

(b) 30-LLZO, $t_H = 1/2h$

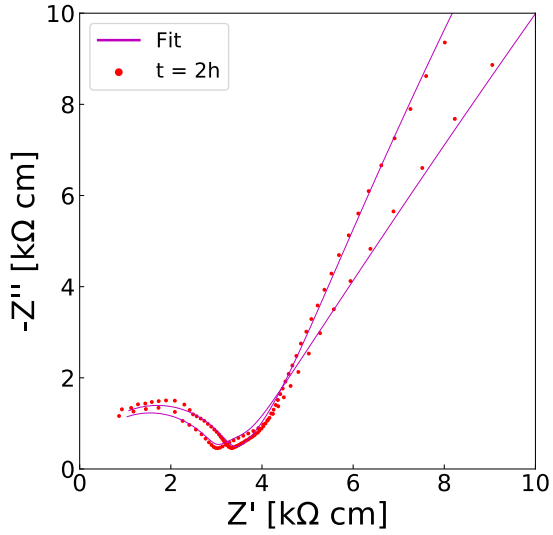

(c) 24-LLZO, $t_H = 2h$

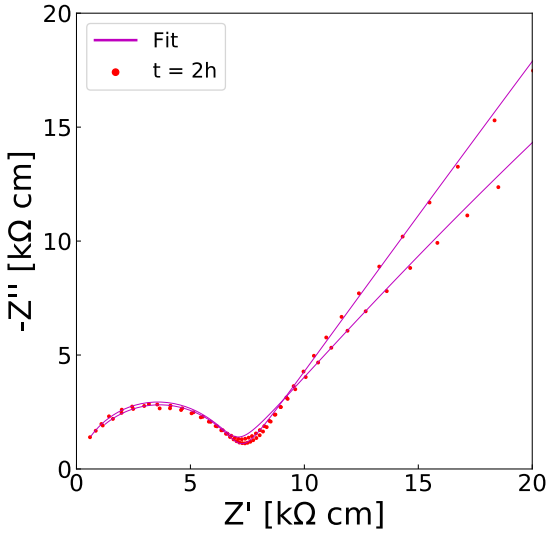

(d) 30-LLZO, $t_H = 2h$

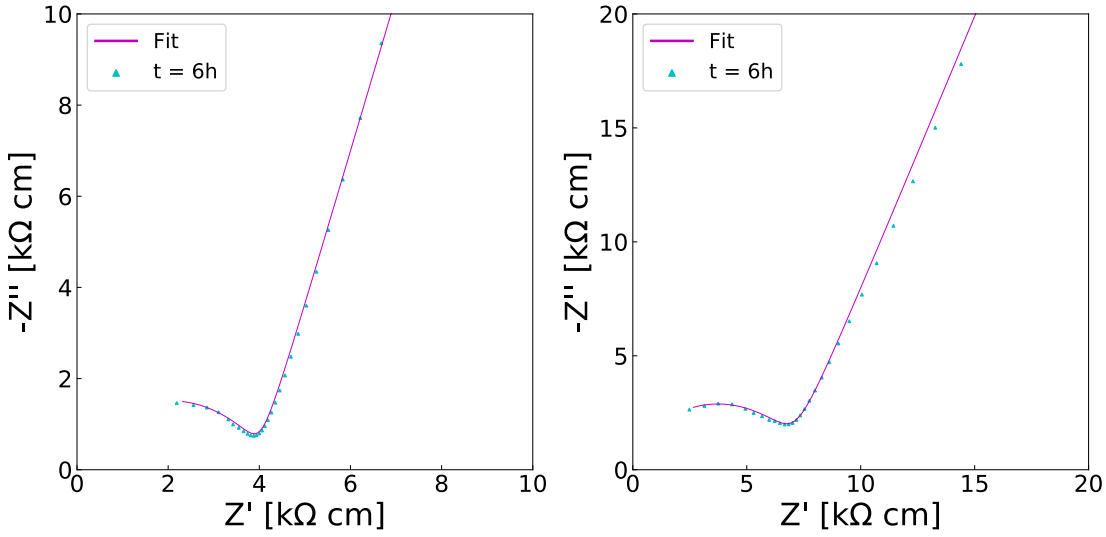

(e) 24-LLZO, $t_H = 6h$ **(f)** 30-LLZO, $t_H = 6h$

Figure D.1. The EIS data presented in normalised Nyquist plots, where Z' is the real part and Z" is the imaginary part of the impedance. The best fit of the data to the respective equivalent circuit is included in all the diagrams.

$$Z(\omega) = \frac{R_1}{R_1 Q_1 (i\omega)^{\alpha_1} + 1} + \frac{R_2}{R_2 Q_2 (i\omega)^{\alpha_2} + 1} \Rightarrow \sigma_{tot} = \frac{t}{R_1 A} \tag{D.1}$$

$$Z(\omega) = \frac{R_1}{R_1 Q_1 (i\omega)^{\alpha_1} + 1} + \frac{R_2}{R_2 Q_2 (i\omega)^{\alpha_2} + 1} + \frac{R_3}{R_3 Q_3 (i\omega)^{\alpha_3} + 1} \Rightarrow \sigma_{tot} = \frac{t}{(R_1 + R_2) A} \tag{D.2}$$

Table D.1: The best fit parameters for the impedance data as calculated by EC-lab. α=Phase argument of the CPE (unitless), Q=Magnitude of the CPE $[S \cdot s^{\alpha}]$, R=Resistance $[\Omega]$.

Figure	Q_1	α_1	R_1	Q_2	α_2	R_2	Q_3	α_3	R_3
D.1a	$2.72 \cdot 10^{-10}$	0.88	1440	$1.64 \cdot 10^{-8}$	0.93	410	$5.6 \cdot 10^{-7}$	0.75	$1.49 \cdot 10^{5}$
D.1b	$1.12 \cdot 10^{-10}$	0.92	2862	$2.89 \cdot 10^{-6}$	0.52	$1.20 \cdot 10^{5}$	-	-	-
D.1c	$4.12 \cdot 10^{-10}$	0.88	728	$4.65 \cdot 10^{-6}$	0.59	206	$4.98 \cdot 10^{-7}$	0.79	$4.15 \cdot 10^{4}$
	$5.18 \cdot 10^{-10}$	0.86	775	$2.03 \cdot 10^{-8}$	1.0	93.9	$1.77 \cdot 10^{-6}$	0.64	$1.06 \cdot 10^{5}$
D.1d	$5.10 \cdot 10^{-10}$	0.84	1860	$1.49 \cdot 10^{-6}$	0.61	$4.64 \cdot 10^{5}$	-	-	-
	$3.88 \cdot 10^{-10}$	0.89	1617	$2.36 \cdot 10^{-6}$	0.55	$7.53 \cdot 10^{4}$	-	-	-
D.1e [a]	$1.46 \cdot 10^{-9}$	0.81	337	$1.16 \cdot 10^{-7}$	0.82	$1.60 \cdot 10^{36}$	-	-	-
D.1f [a]	$7.60 \cdot 10^{-10}$	0.85	558	$1.28 \cdot 10^{-7}$	0.75	$2.17 \cdot 10^{19}$	-	-	-

[a] The pellet was polished rigorously before measurement.

In Table D.1, the fits with Q_3, α_3, and R_3 values were fitted using the equivalent circuit depicted in Fig. 3.6b, and the other fits were fitted using the equivalent circuit depicted in Fig. 3.6a. The total resistance (R_{tot} equal to $(R_1 + R_2)$ or R_1 depending on equivalent circuit), thickness, and diameter are tabulated in Table D.2. The standard deviation of the ionic conductivity is estimated using Gauss' law of error propagation as outlined in Section E. The uncertainty of diameter measurements is set to 0.02 mm, and the uncertainty of the thickness measurements is set to 0.03 mm. This is based on the typical variance in diameter and thickness of measured samples. The error of thickness measurements is higher than diameter measurements due to thickness variations introduced during polishing.

Table D.2: The resistance and dimensions of pellets. R_{tot}=Total resistance, t=Polished thickness, d=Diameter.

Figure	R_{tot} [Ω]	t [mm]	d [mm]
D.1a	1851 ± 0.7	1.13 ± 0.03	7.68 ± 0.02
D.1b	2862 ± 0.8	1.14 ± 0.03	7.61 ± 0.02
D.1c	934 ± 0.8	1.05 ± 0.03	7.75 ± 0.02
	869 ± 1	1.18 ± 0.03	7.60 ± 0.02
D.1d	1860 ± 0.8	1.18 ± 0.03	7.50 ± 0.02
	1617 ± 0.9	1.10 ± 0.03	7.51 ± 0.02
D.1e	337 ± 2	0.40 ± 0.03	7.69 ± 0.02
D.1f	558 ± 1	0.36 ± 0.03	7.42 ± 0.02

E Gauss' law of error propagation

The standard deviation, σ, of derived quantities is estimated using Gauss' law of error propagation. Eq. E.1 is the general expression for error propagation with uncorrelated variables.

$$\sigma_f = \sqrt{\left(\frac{\partial f}{\partial x}\right)^2 \sigma_x^2 + \left(\frac{\partial f}{\partial y}\right)^2 \sigma_y^2 + \left(\frac{\partial f}{\partial z}\right)^2 \sigma_z^2 + \ldots} \tag{E.1}$$

Gauss' law of error propagation was applied to calculate the standard deviation of RD and σ_{tot} values presented in Section 4.

F LLZO crystal structure

The complete crystal structure of cubic Al-doped and tetragonal LLZO are shown in Fig. F.1. These models were generated using the Vesta V3.4.6 software. The main difference between cubic and tetragonal LLZO is the Li arrangement.

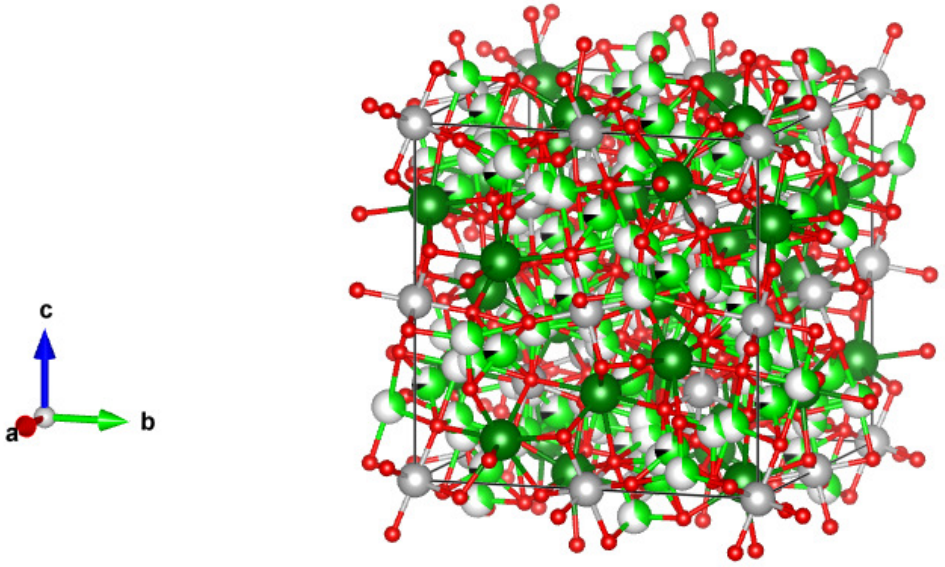

(a) Cubic Al-LLZO

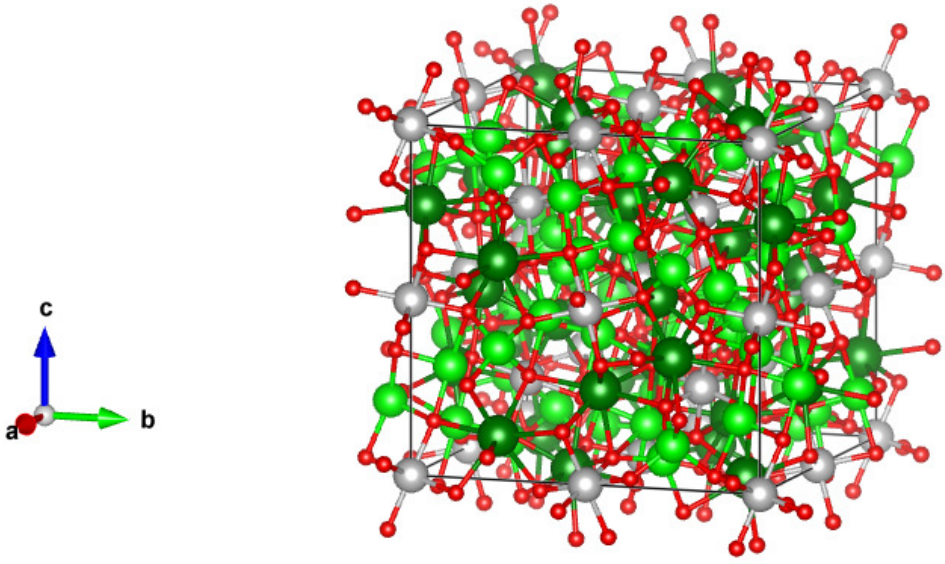

(b) Tetragonal LLZO

Figure F.1. The Vesta-generated unit cell of (a) Al-doped cubic LLZO and (b) tetragonal LLZO. Li is light green, La is dark green, Zr is grey, O is red, Al is black, and vacancies are white. Partially occupied sites are marked by partially coloured spheres, where the occupancy is denoted by the fraction of the corresponding colour.

Ulrik Aalborg Eriksen

Sintering and transport properties of Al-LLZO ceramic electrolytes for use in solid-state Li-ion batteries

NTNU
Norwegian University of
Science and Technology